Heat production in Alkaline Capillary-Fed Water Electrolysis

Krishna Manna

Delft University of Technology

TU Delft

Heat production in Alkaline Capillary-Fed Water Electrolysis

by

Krishna Manna

to obtain the degree of Master of Science
at the Delft University of Technology,
to be defended publicly on Friday July 14, 2023 at 09:30 AM.

Student number:	4392035	
Project duration:	September 12, 2022 – July 14, 2023	
Thesis committee:	Dr. ir. J.W. Haverkort,	TU Delft, supervisor
	Prof. dr. K. Hooman,	TU Delft
	Dr. H. Bazyar,	TU Delft

This thesis is confidential and cannot be made public until July 6, 2025.

TU Delft

Preface

Dear reader,

A preface would not begin to scratch the surface of the gratitude that I hold among all those involved in this process. But I will try.

My supervisor, Willem, has been a role model during this whole process. The enthusiasm you bring and the warm welcome that you provide has given me a safe space to learn and develop myself as an individual. My co-supervisor, Araz, has been so much of an inspiration for me throughout the process. No week has passed where I did not learn from you. I can not forget Nico, you have shown me what it means to convey a story. Your lessons will stay with me for all my future endeavors.

Lastly, my parents and Ashni who always wish the best for me. Words can not express how lucky I am. You all have been a continuous support throughout the whole process for which I am eternally grateful. This is for you.

Enjoy!

Krishna Manna
Delft, July 2023

Abstract

Hydrogen will play an important role in decarbonising sectors that produce carbon-dioxide in their activities. In doing so, hydrogen will be important in the fight against ongoing climate change. Alkaline water electrolyzers running on renewable resources are a promising way to generate green hydrogen. However, traditional alkaline water electrolyzers have moderate efficiency and are commonly costly to build and costly to scale up. This master thesis introduces a recently surfaced method to produce hydrogen and oxygen using alkaline water electrolysis. A hydrophilic porous diaphragm is used that can feed electrolyte laterally to two porous electrodes that are placed against it. Consequently, hydrogen and oxygen are produced directly at the electrodes without any bubble formation. More specifically, this master thesis aims to investigate the thermal behaviour of such a capillary-fed electrolyzer and the limits to which capillary-fed electrolysis can be sustained.

A small scale capillary-fed cell and a larger segmented cell are manufactured during the project. Both cells are used to perform experiments at constant current. Capillary rise in diaphragms with and without compression deviate from the Lucas-Washburn model for capillary rise. Particularly the polyethersulfone material outperforms the diaphragms that were studied. It follows the Lucas-Washburn equation relatively well and exhibits two times deeper penetration under compression. Furthermore, experiments have been performed studying the relation between electrolytic concentration and capillary wicking. Although more highly concentrated KOH solutions for electrolytes increase conductivity over time, it has shown that for the utilised diaphragm a KOH solution surpassing 3 moles per litre shows problematic capillarity. Contact angle experiments with 6M KOH have shown a hydrophobic contact angle of $\bar{\theta}_{\text{6M}} \approx 78.0^\circ$ compared to complete imbibition, i.e $\theta = 0^\circ$, for 1,2 and 3M KOH solutions. The origin of these extremely large contact angles on the polyethersulfone substrate is not fully understood. The study has culminated in performing experiments at constant current and low concentration KOH utilising flushing and dilution techniques to prevent precipitation at the electrodes. The small cell reached an overall heat transfer coefficient of $h = 121$ W/m^{2}K, showing very large heat production for a relatively small surface area. For the segmented cell, electrolyte supply with a bottom-up feed resulted in $h = 19.13$ W/m^{2}K in which precipitation occurred. The top-down feed showed that the top segment has the largest areal heat dissipation. The heat transfer coefficient equates to $h = 25.73$ W/m^{2}K. A final enhancement has been made by introducing Nickel Felt Fiber conducting layers into the cell to improve electronic conductivity. This resulted in an increased range of current densities that could be reached at lower overpotentials compared to absence of these conductive layers. This resulted in the bottom most segment to exhibit the largest areal heat dissipation. The heat transfer coefficient here equates to $h = 43.86$ W/m^{2}K.

This study takes another important step into the regime of capillary-fed electrolysis and alternative electrolysis methods in general. Introducing an alternative design, assessing this design from experimentation and reporting on subsequent steps that can be taken.

Contents

List of Figures

List of Tables

Nomenclature

Abbreviations

Abbreviation	Definition
Bi	Biot Number
ePTFE	Expanded Polytetrafluoroethylene
Gr	Grashof Number
HER	Hydrogen Evolution Reaction
KOH	Potassium Hydroxide
LTC	Lumped Thermal Capacity
MEA	Membrane Electrode Assembly
Nu	Nusselt Number
OC	Open Circuit
OER	Oxygen Evolution Reaction
PES	Polyethersulfone
Pr	Prandtl Number
PMMA	Polymethylmethacrylate
PTFE	Polytetrafluoroethylene
Ra	Rayleigh Number
TN	Thermoneutral

Symbols

Symbol	Definition	Unit
$C_{\text{O,eq}}$	Concentration of oxidized species in bulk electrolyte	[molm^{-3}]
C_{O}	Concentration of oxidized species close to electrode	[molm^{-3}]
$C_{\text{R,eq}}$	Concentration of reductive species in bulk electrolyte	[molm^{-3}]
C_{R}	Concentration of reductive species close to electrode	[molm^{-3}]
E^0_{cell}	Equilibrium cell potential	[V]
E^0_{TN}	Thermoneutral potential	[V]
ΔG	Change in Gibbs free energy	[Jmol^{-1}]
ΔH	Change in enthalpy	[Jmol^{-1}]
ΔS	Change in entropy	[Jmol^{-1}K^{-1}]
k	Mass transfer coefficient / Reaction rate constant	[mol^{1-r}s^{-1}m^{3r-2}][1]
n	Number of electrons	[-]
F	Faraday's constant ($F = 96485$)	[Cmol^{-1}]
I	Current	[A]
j	Current density	[Am^{-2}]
$\mathbb{D}$	Diffusion coefficient	[m^{2}s^{-1}]
Q_{gas}	Volumetric gas flow	[m^{3}s^{-1}]
$\dot{Q}_v$	Heat production	[W]
$\dot{Q}_{\text{loss}}$	Heat loss	[W]
h_c	(Convective) Heat transfer coefficient	[Wm^{-2}K^{-1}]
α	Charge transfer coefficient	[-]

[1] For first order reactions, $r = 1$.

Symbol	Definition	Unit
γ	Surface tension	[kgs^{-2}]
ϵ	Porosity / Void fraction	[-]
η	Overpotential	[V]
κ	Ionic conductivity	[Ω^{-1}m^{-1}]
τ	Tortuosity	[-]
Φ	Volumetric flux	[m^{3}s^{-1}]

1

Introduction

Hydrogen accounts for approximately 75% of the mass in the universe [12]. However, the Earth is an exception in this statement. Molecular hydrogen is rather scarce in the Earth's atmosphere. Yet, on Earth, molecular hydrogen is abundantly available within a variety of liquids, solids and gases where it combines with different elements. Water, for example, is the simplest form of the chemical bond between hydrogen and oxygen molecules. Ongoing environmental pollution and climate change call for innovative technology that can enhance a greener future. Hydrogen will play an important role in this aspect as it can decarbonise various sectors such as the industrial sector, automotive transport, marine sector and the built environment. All of which still have a large contribution to global carbon-dioxide emission into the atmosphere. Figure 1.1 shows how hydrogen can play a key role in working towards a greener future. Added to the scope of the aforementioned sectors, hydrogen can sustainably be generated through electrolysis using renewable resources and it can be stored and utilised together with fuel cells to act as a buffer for the electrical power grid [19].

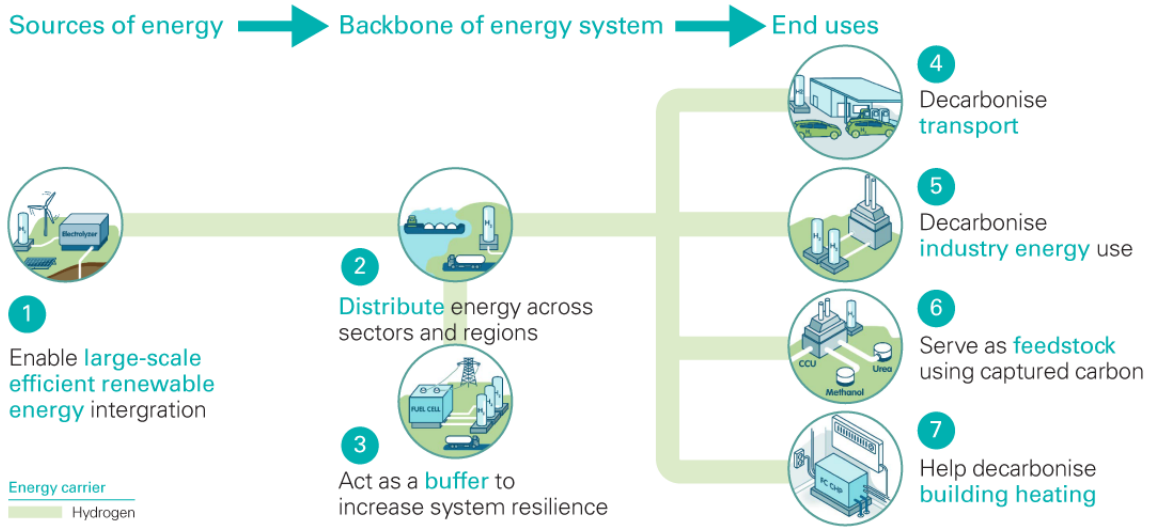

Figure 1.1: Overview of the (future) use of hydrogen in a greener economy. Generated by the 'Hydrogen Council' which consists of members of various disciplines and sectors. Retrieved from [19].

A lot of research is being done in the field of water electrolysis to generate hydrogen and oxygen. This master thesis will introduce a recently surfaced type of electrolyzer which will be briefly introduced next and deeper later in the report.

1.1. Research question

This master thesis focuses on the research and experimental work regarding the capillary-fed electrolyzer. More specifically, recent work by Hodges et al. [1] showed that the capillary-fed electrolyzer can reach efficiencies up to 100%. In short, the capillary-fed electrolyzer employs a means of directly producing bulk hydrogen and oxygen gas by taking in electrolyte from a reservoir using capillary motion. Conventional alkaline water electrolyzers have to deal with ohmic losses due to bubble nucleation which increases the potential that has to be applied to the cell. The capillary-fed cell is inherently bubble free. However, less work has been conducted regarding the thermal behaviour of the capillary-fed electrolyzer. The heat production over time and the temperature distribution within the cell are still topics under consideration. Furthermore, the impact of different diaphragm materials with different material properties are still questions to be answered. The main question that we aim to answer in this master thesis is the following:

- **How hot does a capillary-fed electrolyzer become as a function of the areal heat dissipation during alkaline water electrolysis?**

Logically, within the scope of the project, the aim is not so much to build and study an electrochemical cell that outperforms similar cells in literature. The focus lies more on investigating what the thermal behaviour of such a cell is, what affects its performance and the impact of using e.g. different materials in the cell. These can be summarized more clearly with the following subquestions that will help to answer the main research question:

- How hot does a capillary-fed electrolyzer become as a function of current density, cell potential and height?
- How does diaphragm porosity and material impact the electrolyte flow, current density and cell potential?
- How does electrolyte supply from the bottom versus the top impact heat production within the cell?

1.2. Structure of the thesis

The thesis report consists of six chapters including this introduction. Chapter 2 introduces the theoretical basis regarding water electrolysis in general. Next to a brief history on water electrolysis we discuss the fundamentals of water electrolysis, the thermodynamics related to water electrolysis and we discuss the kinetics in an electrochemical cell. Chapter 3 focuses on cell design. Fundamental elements in cell design are presented and two capillary-fed elecrolyzer designs are presented. Chapter 4 focuses on presenting the various experiments that have been performed together with experimental setups and descriptions thereof. Chapter 5 presents the results and discusses these in light of the posed research (sub)questions. The report is finalized with concluding remarks and prospects for future work.

2

Theory

2.1. Brief history on water electrolysis

The first experimental observations related to water electrolysis go back to the sixteenth century. Garche et al. [46] describes one of the prime observations of hydrogen as a product gas after dissolution of metals within a sulfuric acid. They also describe how Adriaan Paets van Troostwijk (1752–1837) and Johan Rudolph Deiman (1743–1808) were the first to succesfully generate hydrogen and oxygen in a electrostatic generator with gold electrodes in water using a Leyden jar. A Leyden jar filled with water, seen in Figure 2.1, consists of an insulating glass wall. The inner and outer surfaces are foiled. The electrode in the middle touching the inside is commonly connected to a source of charge. This can be attributed the first account of water electrolysis still very much in its infancy.

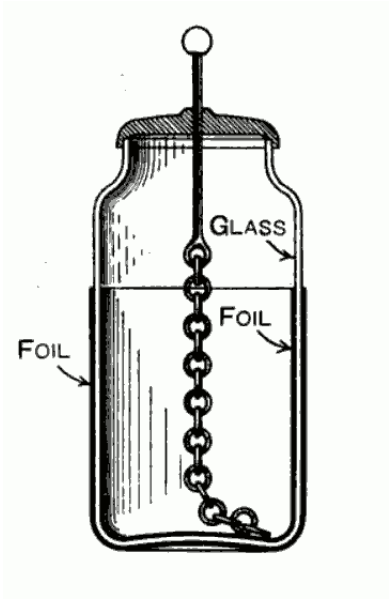

Figure 2.1: Schematic of a Leyden jar. [57]

Figure 2.2: Hydropowered water electrolysis plant for production of hydrogen for ammonia synthesis. [17]

The early 1900s presented the first industrial electrolyzer plant with subsequent technological improvements in this field satisfying consumer demand for e.g. ammonia synthesis [5][17]. Figure 2.2 shows the first large scale water electrolysis plant used for ammonia synthesis in Norway. Installed in 1927 in Rjukan, Norway, the 135 MW plant could produce approximately 30.000 $m^3H_2hr^{-1}$. The supply of high purity hydrogen is closely intertwined with fluctuating electricity costs. Hence, the development and interest in water electrolysis was largely dependent on economical considerations. Guerrini and Trasatti [26] describe the decrease in cost for fossil fuels in the early 1980s that lead to a sharp decrease in

interest for water electrolysis. Present day, the renewed interest in water electrolysis and research thereof have sparked. Environmental pollution, global climate change and a steep rise in oil prices are some of the reasons for this renewed enthusiasm [26]. However, at the time of writing this report, gas and electricity prices have reached record heights as a consequence of ongoing global conflicts which has forced a number of countries to reignite fossil fuel based chemical plants for electricity and heat [14].

2.2. Fundamentals of water electrolysis

The fundamental principle of water electrolysis consists of splitting water molecules into hydrogen and oxygen molecules. This is done by driving a direct current through a water-electrolyte solution. Consequently, electrodes placed in the solution are responsible for the production of the product gases. Figure 2.3 depicts the schematic of the working principle of alkaline water electrolyzers.

2.2.1. Hydrogen evolution reaction

At the cathode, shown on the right hand side of Figure 2.3, the hydrogen evolution reaction (HER) takes place as [3]:

$$2H_2O_{(l)} + 2e^- \rightleftharpoons H_{2(g)} + 2OH^-_{(aq.)} \tag{2.1}$$

In which for every two molecules of water and moles of electrons, two hydrogen atoms and hydroxide ions are produced. As this reaction requires negatively charged electrons, the cathode is also negatively charged.

2.2.2. Oxygen evolution reaction

At the anode, depicted on the left side in Figure 2.3, the oxygen evolution reaction (OER) takes place.

$$2OH^-_{(aq.)} \rightleftharpoons H_2O_{(l)} + \frac{1}{2}O_{2(g)} + 2e^- \tag{2.2}$$

During this chemical reaction, the hydroxide ions are transported through the electrolyte to undergo the oxidation reaction at the anode. Consequently, this results in oxygen gas being generated together with electrons that close the electrical circuit in this way. Hence, the overall reaction can be described as follows:

$$2H_2O_{(l)} \rightleftharpoons O_{2(g)} + 2H_{2(g)} \tag{2.3}$$

Which describes that two molecules of liquid water can be split into one oxygen and two hydrogen molecules. Furthermore, water electrolyzers have to be operating at a potential for which water electrolysis can actually occur. For the reaction described in Equation 2.3 this is approximately $E^0_{\text{cell}} = 1.23$ V at standard conditions (1 atm, 25°C) [39]. E^0_{cell} is the equilibrium voltage between the anode and the cathode and can be expressed as [58]:

$$E^0_{\text{cell}} = E^0_{\text{anode}} - E^0_{\text{cathode}} \tag{2.4}$$

This is commonly mentioned as the reversible cell voltage or the open circuit potential E^0_{oc} or E^0_{eq} just when the current is turned off [39][58]. Any potential that is measured in excess of the equilibrium potential is called the cell overpotential. Figure 2.4 relates the electrolyzer potential to the temperature and shows when water electrolysis can occur and at what potential. The equilibrium voltage $E^0_{\text{cell}} = 1.23$ V can be seen here. Furthermore, note that below the equilibrium voltage electrolysis can not occur. It can be seen that increasing the temperature lowers the equilibrium voltage. For water electrolysis to take place and gaseous products to form, the thermoneutral voltage E_{TN} is used. Below this threshold, the reaction is endothermic and extracts heat from the surroundings. Above this threshold, water electrolysis generates heat.

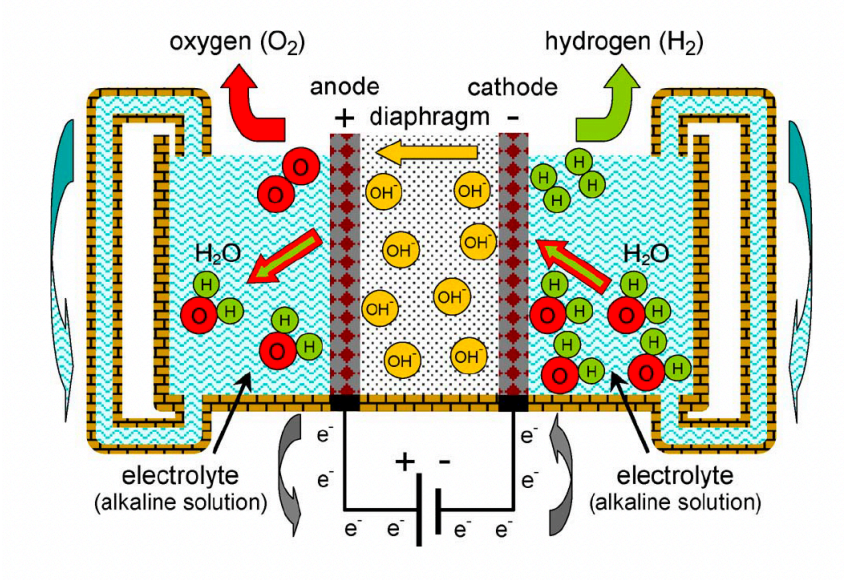

Figure 2.3: Schematic of the working principle of an alkaline water electrolyzer with circulating electrolyte. Retrieved from [3].

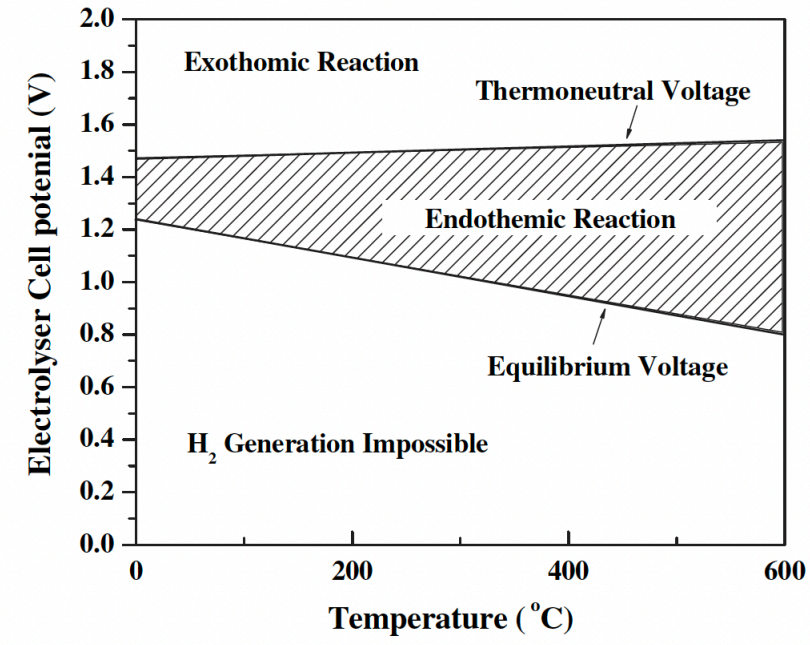

Figure 2.4: electrolyzer cell potential as a function of temperature. Retrieved from [58].

2.3. Thermodynamics

During water electrolysis, we convert electrical energy into chemical energy. The thermodynamic potential that relates the entropy S and enthalpy H is called the Gibbs free energy G. The change in the Gibbs free energy can be described mathematically as [28]:

$$\Delta G = \Delta H - T\Delta S \tag{2.5}$$

With ΔH the change in enthalpy, T the temperature and ΔS the entropy change. At constant pressure and temperature, this quantity describes the direction of the chemical reaction:

$$\Delta G > 0 : \text{The chemical reaction is non-spontaneous.} \tag{2.6}$$
$$\Delta G = 0 : \text{Process is in equilibrium.} \tag{2.7}$$
$$\Delta G < 0 : \text{The chemical reaction is spontaneous.} \tag{2.8}$$

In which spontaneity indicates whether or not external energy has to be supplied for the reaction to occur, i.e. a spontaneous reaction will not have the need of external energy. For the reaction described in Equation 2.3, we have for standard conditions of 1 atm and 25°C:

$$\Delta H^0_{\mathrm{H_2O(l)}} = -285.8 \text{ kJ/mol} \tag{2.9}$$
$$\Delta S^0_{\mathrm{H_2O(l)}} = -163.39 \text{ kJ/mol·K} \tag{2.10}$$
$$\Delta G^0_{\mathrm{H_2O(l)}} = -285.83 - (298)(-163.39) \approx -237.14 \text{ kJ/mol} \tag{2.11}$$

Note that the equilibrium condition $\Delta G = 0$ describes that the system is unable to perform work. Following [26], we note that the equilibrium condition regarding a chemical system can be expressed as a function of the potential difference ΔE as:

$$\Delta G = -nF\Delta E \tag{2.12}$$

Where n describes the number of moles of electrons needed per mole of product. $F = 96485$ [C/mol] is Faraday's constant and ΔE is the potential difference measured between two electrodes. From here the open circuit potential E^0_{cell} can be derived as:

$$E^0_{\mathrm{cell}} = \frac{-\Delta G}{nF} = \frac{-(-237.14 \cdot 10^3)}{2 \cdot 96485} \approx 1.23 \text{ V} \tag{2.13}$$

Equation 2.13 shows that a potential of 1.23 V has to be applied to arrange water electrolysis. Around this voltage and standard conditions, this process will be endothermic and cool the surroundings. The potential required to have no net absorption or expulsion of heat is described by the thermoneutral voltage E_{TN} which has been introduced in Section 1. Mathematically, this threshold can be quantified by utilising the enthalpy change which describes the energy requirement to bring reactants from their standard reference states to products in their standard reference states [26]:

$$E_{\mathrm{TN}} = \frac{-\Delta H}{nF} = \frac{-(-285.8 \cdot 10^3)}{2 \cdot 96485} \approx 1.48 \text{ V} \tag{2.14}$$

2.4. Kinetics in an electrochemical cell

Water electrolysis within an electrochemical cell does not proceed without energetic losses. These are losses - or resistances - that the cell elements pose to the flow of ionic current. These can be summarised as shown in Table 2.1 [58].
Furthermore, the resistances as noted in Table 2.1 can be expressed as a series connection of resistances by utilizing the illustrations in Figures 2.3 and 2.5.

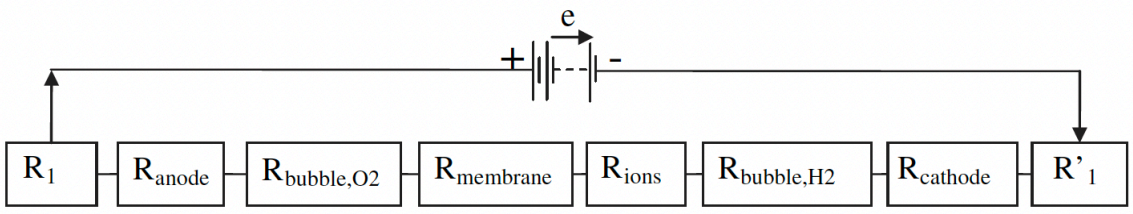

Figure 2.5: Electrical circuit analogy of resistances within an electrochemical cell.

Within this circuit, the resistances are connected in series and totals:

$$R_{\mathrm{tot}} = \sum R_i \tag{2.15}$$

With i, the elements as noted in Table 2.1.

Item	Symbol	Barrier
Electrical circuit	R_1	External circuit resistance to ionic current due to wiring and additional connections on the anode side.
Anode	R_{anode}	Overpotential associated with OER.
Electrode surface	R_{bubble,O_2}	Overpotential associated with bubble coverage on the positive electrode surface.
Diaphragm	R_{membrane}	Overpotential associated with the resistance that the separator poses.
Electrolyte	R_{ions}	Overpotential associated with the resistance that the electrolyte solution poses to ionic transfer.
Electrode surface	R_{bubble,H_2}	Overpotential associated with bubble coverage on the negative electrode surface.
Cathode	R_{cathode}	Overpotential associated with HER.
Electrical circuit	$R_1^{'}$	External circuit resistance to ion flow due to wiring and additional connections on the cathode side.

Table 2.1: Electrical analogy of resistances within an electrochemical cell [58].

2.4.1. Ohmic overpotential

The overpotential caused by the resistances that the electrical circuit (cables/wires etc.), electrolyte and electrodes pose to ionic flow can be approximated by considering Ohm's law for resistances within an electrical circuit:

$$R = UI = \frac{L}{\kappa A} \tag{2.16}$$

With R the resistance which can be regarded as R_1 and R_1' in Figure 2.5, U the potential and I the current. Furthermore, with regard to the transfer of ions, L is the length or distance between the electrodes [m], κ the ionic conductivity [Ω^{-1}·m^{-1}] and A the surface area in [m^2].

2.4.2. Activation overpotential

When considering additional losses that contribute to an increasing overpotential we can look into activation overpotentials. The activation energy is the energy that has to be supplied to overcome any repelling forces acting between reactant molecules in order for attractive forces to take over at the electrodes. Hence, the overpotential that accompanies this is commonly adopted as the overpotential caused by electrode kinetics. R_{anode} and R_{cathode} describe this part of the resistance scheme in Figure 2.5 at the anode and cathode electrode respectively.

Concentration-independent Butler-Volmer Equation

The Butler-Volmer equation for water electrolysis kinetics shows how the current density $j\ \left[\text{A/m}^2\right]$ is related to the overpotential $\eta_i,\ i \in \{a, c\}$ at the anode and cathode, respectively [26] [43]. Mathematically, this can be described as:

$$j = j_0 \left\{ \mathrm{e}^{\left(\frac{(1-\alpha)F\eta}{RT}\right)} - \mathrm{e}^{\left(\frac{-\alpha F\eta}{RT}\right)} \right\} \tag{2.17}$$

with j_0 $\left[\text{A}/\text{m}^2\right]$ the exchange current density, F known as Faraday's constant equal to $F = 96485$ [C/mol], R the gas constant equal to $R = 8.314$ [J/mol·K], T the temperature in Kelvin and α, a non-dimensional quantity called the charge transfer coefficient, which is a measure of the symmetry between the oxidative and reductive component of the current. The components of the current can be seen in Equation 2.18:

$$j = j_0 \left\{ \underbrace{\mathrm{e}^{\left(\frac{(1-\alpha)F\eta}{RT}\right)}}_{\text{Oxidation}} - \underbrace{\mathrm{e}^{\left(\frac{-\alpha F\eta}{RT}\right)}}_{\text{Reduction}} \right\} \tag{2.18}$$

Both j_0 and α are properties that depend on the electrode material that is utilised [34]. The exchange current density j_0 can be explained from Equation 2.18 as the magnitude of the cathodic and anodic currents at zero overpotential $\eta = 0$ [V] and a net current density of $j = 0$ [A/m^2]. At the equilibrium potential this reduces simply to $j = j_0 = 0$ [A/m^2]. If we now utilise the general statement that relates the Gibbs free energy from Equation 2.12 with its equilibrium value [28]:

$$\Delta G = \Delta G^0 + RT \ln Q \tag{2.19}$$

$$-nF\Delta E = -nF\Delta E^0 + RT \ln Q \tag{2.20}$$

$$E_{\text{eq}} = E^0 + \frac{RT}{nF} \ln Q \tag{2.21}$$

we find the Nernst Equation in which Q is the reaction quotient. This equation relates the equilibrium voltage of an electrode to its open circuit potential.

The Butler-Volmer equation does not directly specify what j_0 and α are since we have more unknowns than equations to solve. So called Tafel plots can aid in determining the remaining unknowns. The bottom plot in Figure 2.6 illustrates the Tafel plot and shows how the charge transfer coefficient α and the exchange current density j_0 can be determined graphically from the current density and potential. j_0 can be deduced from the intersection of the lines with the $\eta = 0$ V axis. α can be deduced from the gradients of the lines. Furthermore, note that the lower graph in Figure 2.6 follows from taking the log of Equation 2.17:

$$\ln |j| = \ln |j_0| + \left(\frac{(1-\alpha)F\eta}{RT}\right) + \left(\frac{-\alpha F\eta}{RT}\right) \tag{2.22}$$

The lower plot in Figure 2.6 shows the symmetry for $\alpha = 0.5$. However, for decreasing α the oxidative component of the current density gives the dominant contribution.

Tafel equation

At very high overpotentials, i.e. $\eta \geq 0.1$ V the Butler-Volmer equation reduces to the anodic form:

$$\eta_{\text{a}} = -\frac{RT}{(1-\alpha)F} \ln |j_0| + \frac{RT}{(1-\alpha)F} \ln |j| = -a_{\text{a}} + b_{\text{a}} \ln |j| \tag{2.23}$$

Similarly, for $\eta \leq -0.1$ V the Butler-Volmer equation reduces to the cathodic form:

$$\eta_{\text{c}} = \frac{RT}{\alpha F} \ln |j_0| - \frac{RT}{\alpha F} \ln |j| = a_{\text{c}} - b_{\text{c}} \ln |j| \tag{2.24}$$

Hence, Equations 2.23 and 2.24 can be written as:

$$\eta_{\text{act}} = \eta_i = a_i \pm b_i \ln |j|, \qquad i \in \{\text{a}, \text{c}\} \tag{2.25}$$

Which is called the Tafel equation in which b_i is the Tafel slope [58]. It provides an insight into electrochemical reaction kinetics.

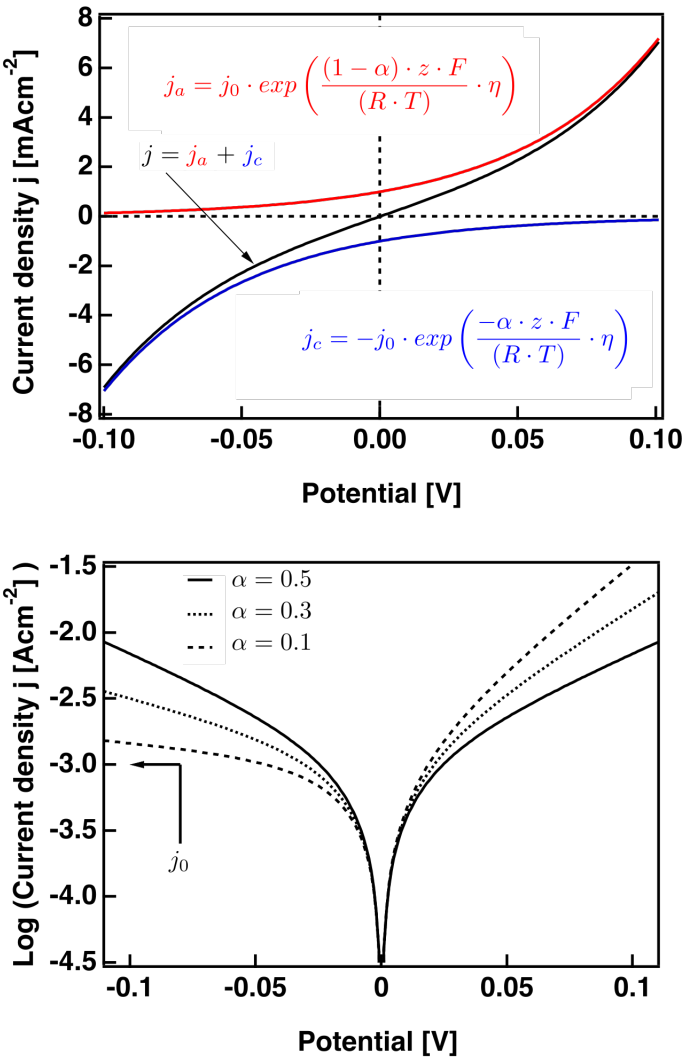

Figure 2.6: Tafel plot of logarithmic current density versus potential. Retrieved from [49]. Note that in the top plot, $z = n = 1$ as we are considering a single electron transfer of the form: O + e^- $\leftrightarrow$ R.

Concentration-dependency

Considering an active electrochemical cell with nonzero current over the electrodes, we can not readily assume constant concentrations of the oxidized and reductive species throughout the KOH solution. Evidently, at the electrode surfaces, the concentration of either oxygen or hydrogen differs from the concentration that would be measured in the bulk electrolyte. Hence, a concentration gradient will be observed. Any measured concentration of either oxidative or reductive species will differ from that measured relative to the equilibrium concentration, i.e. $C_{\mathrm{O}} \neq C_{\mathrm{O,eq}}$ and $C_{\mathrm{R}} \neq C_{\mathrm{R,eq}}$. The Butler-Volmer equation in this case can be written as:

$$j = Fk_0 \left\{ C_{\mathrm{R}} e^{\frac{(1-\alpha)\eta F}{RT}} - C_{\mathrm{O}} e^{\frac{-\alpha\eta F}{RT}} \right\} \tag{2.26}$$

In which k_0 is the standard rate constant that describes the rate for which a chemical reaction progresses. At the equilibrium potential the Nernst equation can be described in terms of concentration:

$$E_{\mathrm{eq}} = E^0 + \frac{RT}{F} \ln\left(\frac{C_{\mathrm{O,eq}}}{C_{\mathrm{R,eq}}}\right) \tag{2.27}$$

Note that $\eta = E_{\text{eq}} - E^0$ and when we substitute this into Equation 2.26, the exchange current density can then be described as [21]:

$$j_0 = Fk_0 C_{\text{O,eq}}^{(1-\alpha)} C_{\text{R,eq}}^{\alpha} \tag{2.28}$$

The dependency of the exchange current density on concentration is evident from this relation. Consequently, combining Equations 2.26 and 2.28, we find the concentration-dependent Butler-Volmer equation which can be rewritten in terms of a ratio of concentration to equilibrium concentration.

$$\frac{j}{j_0} = \left(\frac{C_{\text{R}}}{C_{\text{R,eq}}} \mathrm{e}^{\frac{(1-\alpha)\eta F}{RT}} - \frac{C_{\text{O}}}{C_{\text{O,eq}}} \mathrm{e}^{\frac{-\alpha\eta F}{RT}} \right) \tag{2.29}$$

This expression describes the dependency of the current density on concentration differences within the cell. The concentration difference relative to equilibrium conditions is taken here, i.e. in the case when $j = 0$ Am^{-2}.

The Nernst equation can be expressed in concentration amounts as well. We can rewrite Equation 2.21 to:

$$E_{\text{eq}} = E^0 + \frac{RT}{F} \ln \left(\frac{C_{\text{H}_2}^{1/2} C_{\text{O}_2}^{1/4}}{C_{\text{H}_2\text{O}}} \right) \tag{2.30}$$

2.5. Vertical flat plate approximation

Section A.2 showed that a first-order differential equation can describe the temperature evolution over time. Logically, this was done by making certain assumptions. However, much insight can also be gained from the temperature difference, $\Delta T = T_s - T_e$, see Figure 2.7. When we want to approximate the temperature difference along the vertical length of the cell we can use the vertical flat plate approximation [37]. This approach assumes natural convection due to buoyancy forces only, i.e. density variations along the length of the flat plate. Figure 2.7 shows a schematic overview. The heated flat plate of temperature T_s and length L is placed in a fluid with density ρ_e and temperature T_e. A natural convection boundary layer that emerges over time has been drawn and consist of a fluid with density ρ_s. The requirement here is that the Rayleigh number should be below or approximately 10^9, $\text{Pr} \simeq 1$ and $\text{Gr} \simeq 10^9$ in order to maintain laminar conditions.

$$\overline{\text{Nu}}_L = 0.68 + 0.670 \left(\text{Ra}_L \Psi\right)^{\frac{1}{4}} \qquad \text{Ra}_L \lesssim 10^9 \tag{2.31}$$

$$\Psi = \left[1 + \left[\frac{0.492}{\text{Pr}} \right]^{\frac{9}{16}} \right]^{-\frac{16}{9}} \tag{2.32}$$

$$\text{Ra}_L = \frac{\beta \Delta T g L^3}{\nu^2} = GrPr \tag{2.33}$$

Vliet et al. [51] also presents emperically gained approximations of the Nusselt number which can be utilised to calculate the convective heat transfer coefficient. Vliet et al. derived the approximation from the study done on natural convection on inclined surfaces. For the local Nusselt number they found for the laminar case:

$$\text{Nu}_x = 0.60(\text{Gr}_x \text{Pr})^{0.20} \tag{2.34}$$

And for the turbulent case:

$$\text{Nu}_x = 0.302(\text{Gr}_x \text{Pr})^{0.24} \tag{2.35}$$

With Nu_x and Gr_x the local Nusselt and Grashof numbers.

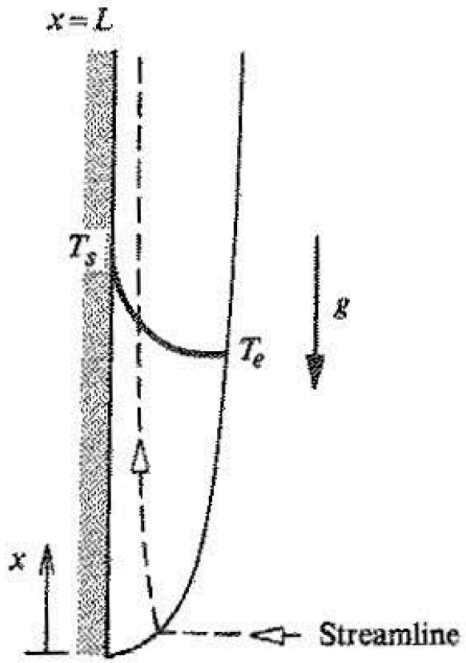

Figure 2.7: Schematic depiction of natural convection boundary layer occurring along a flat vertical plate. Retrieved from [37].

2.6. Capillary flow through porous medium

In building and testing a capillary-fed cell, estimations can be made as to the flow through the membrane. More specifically, the volumetric flow rate through the capillaries can give estimations of the penetration depth and penetration velocity. Additionally, by comparing certain membranes on the aforementioned properties we can give insight into which separator materials should be considered when designing an electrochemical cell utilizing the capillary-fed principle. Particularly for capillary-fed electrolysis, the hydrophilicity of the membrane can be exploited. Edward W. Washburn has been at the front of investigating the dynamics of capillary flow in his 1921 paper [54]. Liquid penetration into capillaries and porous bodies have been approached from a horizontal and a vertical configuration. Washburn performed mercury experiments and manually recorded the measurements to relate the penetration height versus time. Research into capillary rise and capillary action has gained multi-disciplinary interest in fields such as geo-technology [33] and petroleum engineering [36]. Additionally, developments into interfacial science such as the work by Lago and Araujo [32] utilise the Lucas-Washburn equation to research the velocity with which a water front progresses when a capillary tube is filled with beads. Figure 2.8 illustrates a simple schematic of a cylindrical capillary tube including force balances. The hydrostatic pressure force $F_h = \pi r^2 h \rho g$ is in force equilibrium with the capillary force $F_c = 2\pi r \sigma \cos\theta$.

Similarly to Washburn's notations, the pressures working on a capillary of small diameter can be expressed as [54]:

$$\sum P = P_A + P_h + P_s \tag{2.36}$$

Where P_A is the atmospheric pressure, P_h is the hydrostatic pressure and P_s the capillary pressure. These pressure terms can subsequently be expanded as follows:

$$\sum P = P_A + \rho g h + \frac{2\gamma}{r} \cos\theta \tag{2.37}$$

In which h is the height of the liquid, ρ the density, r the radius of a capillary tube, γ the liquid surface tension, g the gravitational acceleration and θ the contact angle made with the capillary wall. Furthermore, we note that the cross sectional area of the capillaries is so small that we can assume a laminar flow regime. Additionally, the Hagen-Poisuille law can be used to relate the flow velocity to the pressure

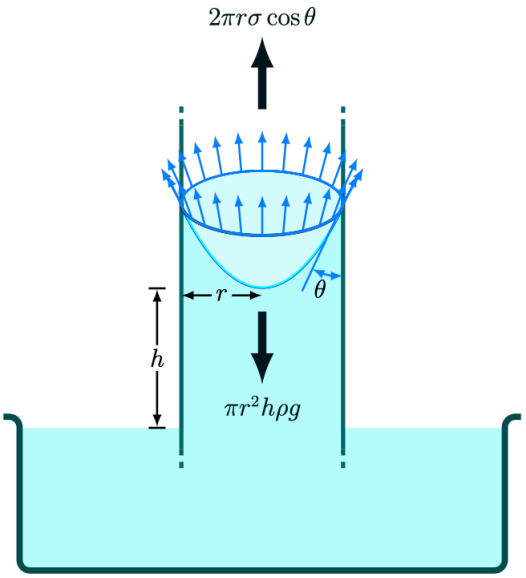

Figure 2.8: Illustration of a force balance in a capillary tube with liquid of density ρ, $\sigma = \gamma$ surface tension, viscosity μ and height h. Retrieved from [45].

drop along the membrane [42]:

$$v = \frac{D^2}{32\mu L}\Delta P \tag{2.38}$$

with D the pore-diameter, μ the dynamic viscosity, L the pore-length and ΔP the pressure drop over the membrane. The pressure drop has commonly been regarded as being dominated by the capillary pressure, i.e. in terms of forces, gravity forces $\ll$ capillary forces. Hence, only the capillary force will be regarded as being the sole driving force when we look at the capillary-fed electrolysis.
Within a membrane or diaphragm we commonly find a multitude of capillaries for which the total cross-sectional area can be expressed with use of the void fraction ϵ that relates the number of capillaries n to the capillary cross sectional area A_c as:

$$\epsilon = nA_c = \frac{n\pi D^2}{4} \tag{2.39}$$

Combining Equations 2.38 and 2.39 we can express the volumetric flux along a membrane of capillary length L as[1]:

$$Q_{\text{vol}} = v\epsilon = \frac{n\pi D^4}{128\mu L}\Delta P \tag{2.40}$$

Which is similar to the approach utilised by Hodges et al. [1], which included a tortuosity[2] term τ to include the actual distance that the liquid travels inside of the capillary:

$$Q_{\text{vol}} = \frac{n\pi D^4}{128\mu\tau L}\Delta P \tag{2.41}$$

Furthermore, if we want an estimate for the time it takes to reach a certain penetration depth, we can derive the Lucas-Washburn equation from a momentum balance inside a capillary tube similar to that illustrated in Figure 2.8. Assuming a 1D flow and ignoring viscous, inertial and gravitational effects of

[1] Note that Washburn [54] expresses the volumetric flux $Q_{\text{vol}} = \frac{dV}{dt}$ as: $\frac{dV}{dt} = \frac{\pi\sum P}{8\mu L}(r^4 + 4\epsilon r^3)$ with ϵ the slip coefficient which is assumed to be equal to zero in Equation 2.40.

[2] The tortuosity term τ can be approximated through Bruggeman's relation: $\tau \approx \epsilon^{-1/2}$. Where ϵ is the porosity.

air at the liquid-gas interface we find the following momentum balance [24]:

$$\frac{2\gamma \cos\theta}{r} = \rho g h + \frac{8\mu h}{r^2}\dot{h} + \rho\frac{d(h\dot{h})}{dt} \tag{2.42}$$

With h the liquid height, $\dot{h}$ the time derivative of the liquid height and ρ the density. The various terms represent capillary pressure, influence of gravity , a viscous term (similar to Equation 2.38) and an inertial term, respectively. To arrive at the Lucas-Washburn approximation, the dominant contributions in the momentum balance are assigned to the capillary pressure and viscous effects. This assumption equates to:

$$\frac{2\gamma \cos\theta}{r} = \frac{8\mu h}{r^2}\dot{h} \tag{2.43}$$

Simplifying equates to [54]:

$$\int \frac{\gamma r \cos\theta}{4\mu} dt = \int h \, dh \tag{2.44}$$

$$\frac{\gamma r \cos\theta}{2\mu} t + C = h^2 \tag{2.45}$$

$$h(t=0) = 0 : \qquad \frac{\gamma r \cos\theta}{2\mu} t = h^2 \tag{2.46}$$

With r the tube-radius and t time. Note that Equation 2.43 shows the rate at which a liquid penetrates the capillary as:

$$\frac{dh}{dt} = \left(\frac{\gamma \cos\theta}{4h\mu}\right) r \tag{2.47}$$

2.7. Capillary length

Section 2.6 noted the dominant driving force when we look at capillary-fed electrolysis. However, to promote and sustain capillary-fed electrolysis, insight into when effects of gravity can be disregarded or not are valuable in choosing the most suitable electrolyte solutions. The capillary length relates the gravity force to surface tension. It can be utilised as a scaling factor and is expressed as

$$r = \sqrt{\frac{\gamma}{\rho g}} \tag{2.48}$$

With r the radius of a droplet, γ the liquid surface tension and g the gravitational acceleration. This scaling derives from the pressures acting on a volume of liquid which can be described by equating the Laplace pressure to the hydrostatic pressure:

$$P_h = P_s \tag{2.49}$$

$$2r\rho g = 2\frac{\gamma}{r} \tag{2.50}$$

$$r = \sqrt{\frac{\gamma}{\rho g}} \tag{2.51}$$

Note that we consider the interface between the gaseous and liquid region. Hence, the contact angle is taken as zero which cancels the cosine term shown in the Young-Laplace expression for capillary pressure.

Equation 2.48 gives an important condition for which gravity effects should be taken into account opposed to when capillary effects are predominantly present. Kranias [30] has determined the capillary length to be equal to 2.7 mm for water. Furthermore, he has experimentally shown that droplet contact angles are reasonably similar for various drop volumes. When the volume is increased from 1 to 10 microliters, the radius of the droplet stays well below the capillary length.

3

Cell Design

Electrolyzer cells come in a variety of configurations. The membranes together with the electrodes are commonly called the membrane electrode assembly (MEA). The demand for a certain species of products, purity, scalability, efficiency and robustness are just a few of the various parameters that are considered when choosing a certain MEA assembly for an electrolyzer. Especially the difference in configuration that the capillary-fed electrolyzer has compared to conventional configurations is shown here. In this section, a brief focus will be on the basic electrochemical cell elements for water electrolysis. Furthermore, some commonly utilised MEA configurations will be presented and discussed. More specifically, the unipolar, bipolar, zero-gap and capillary-fed design will be discussed.

3.1. Fundamentals

In general, the electrochemical cell consists of a number of fundamental components. These can be summarised as being: membrane or diaphragm, anode electrode, cathode electrode, conducting electrolyte solutions and an external power source.

3.1.1. Membrane choice

In an electrochemical cell for water electrolysis the membrane has a multipurpose function. As the hydrogen and oxygen evolution reaction take place at the respective electrodes, the membrane poses as a separating wall between the two produced species. At a temperature of approximately $T = 80°$C, a hydrogen flow containing an oxygen concentration of > 4.6% constitutes an explosive mixture. Similarly, an oxygen flow containing a hydrogen concentration of > 3.8% also constitutes an explosive mixture. In the conventional electrochemical cell, the MEA is submerged in an electrolyte solution which is typically a 30wt% potassium hydroxide solution for increased electrical conductivity. Membranes between the electrodes prevent the passage of electrons but do not block any hydroxide ions (OH^-)) between the anode and the cathode. Consequently, the hydroxide ions are then free to flow to react at the anode to produce oxygen and free electrons. Kamei et al. [11] describe the requirements that water electrolyzer diaphragms need to fulfill. Its functionality as a gas separator and the requirement of good chemical and physical strength are some of the properties that need to be considered. Their invention includes research on the most suitable diaphragm materials and concluded that polyethersulfone is a relatively good option when considering a strong, robust and heat/alkaline resistant material. It is the same membrane material used in the paper about the capillary-fed electrolyzer by Hodges et al.[1].

3.2. Unipolar design

Simple and commonly utilised alkaline water electrolyzer configurations incorporate a so called unipolar or monopolar design, displayed in Figure 3.1. This design consists of a cell in which the cathode and anode electrodes are separated by a diaphragm. The cathode is negatively polarized and the anode is positively polarized. They are responsible for the hydrogen and oxygen production respectively. A cell stack consists of a multitude of individual cells which are placed next to each other. Within a cell stack, each electrode has a single polarity. Hence, the name unipolar design. The cell stack resembles a parallel connection of cells. The current flowing through the stack is a summation of all the individual cells summed while the power supply of each cell is of the same magnitude, i.e.:

$$I_{\text{stack}} = \sum_{n=1}^{N} I_n, \qquad V_{\text{stack}} = V_n \qquad \text{with } n = \{1, \ldots, N\} \tag{3.1}$$

Both Ursua et al. [3] and Zeng et al.[58] highlight the advantages and disadvantages of a unipolar design. Firstly, this type of configuration is well understood and reliable. However, it requires a considerate amount of space to accommodate the stack compared to the bipolar design. For industrial implementations where high production standards are not uncommon, the large footprint may pose as a significant drawback. Another advantage of the unipolar electrolyzer is that its risk of parasitic currents is quite lower than the bipolar electrolyzer (which will be discussed hereafter). This is due to the fact that each cell is connected separately to the power supply. A drawback here is that the wiring poses an extra added penalty - in terms of ohmic losses - to the potential that is applied to the cell stack.

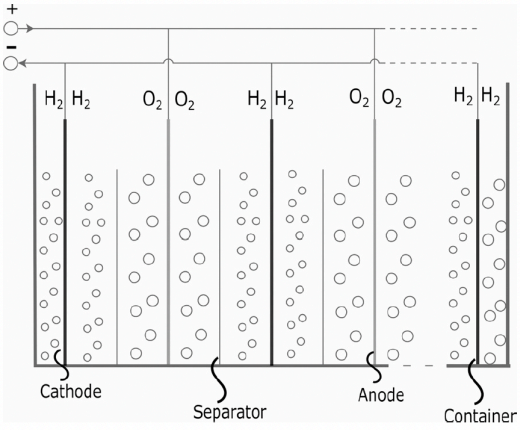

Figure 3.1: Unipolar design. The anode and cathode are separated by diaphragm or separator and are immersed in a liquid electrolyte solution. Each electrode has a single polarity. Retrieved from [5].

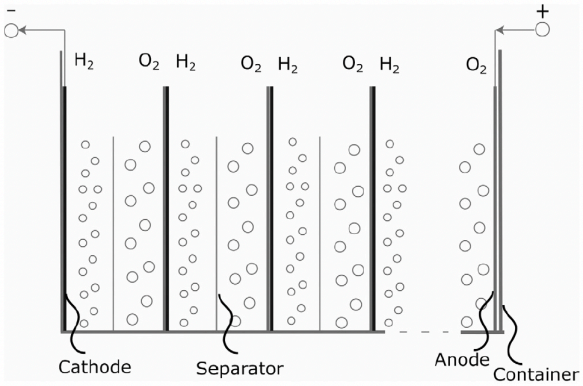

Figure 3.2: Bipolar design. The anode and cathode are separated by diaphragm or separator and are immersed in a liquid electrolyte solution. Each electrode has two polarities. Retrieved from [5].

3.3. Bipolar design

The unipolar configuration can be approximated as a parallel connection of electrochemical cells. When we look at cells that are series connected, we arrive at a configuration as shown in Figure 3.2. The cathode and anode electrodes have similar functionality compared to the unipolar case. However, in this configuration every electrode - apart from the first and last electrode in a stack - has a double purpose. They have two polarities that differ on the front and back side respectively. Hence, the name bipolar design. Each electrode that has two polarities contributes to either a hydrogen or oxygen evolution reaction in a cell. In fact, the functionality of a single electrode now spans over two connected cells. Following Figure 3.2, it is evident that this stack resembles a series connection of cells for which the current which flows through the cells is constant over the length of the stack. Whereas the potential

applied to the stack is a summation of individual cell potentials, i.e.:

$$V_{\text{stack}} = \sum_{n=1}^{N} V_n, \qquad I_{\text{stack}} = I_n \qquad \text{with } n = \{1, \ldots, N\} \tag{3.2}$$

Compared to the unipolar design, the bipolar design Figure 3.2 has an increased complexity as explained by both Ursua et al. [3] and Zeng et al. [58]. Every electrode has to participate in two separate electrochemical reactions. However, apart from its increased complexity, the bipolar design does offer a significant size reduction compared to the unipolar design. In this design, the electrodes are not all individually separated which reduces its footprint considerably. Furthermore, Ansar [5] states that bipolar stacks can operate under increased pressures. Producing compressed hydrogen would reduce costs for equipment such as (hydrogen) compressors. Hodges et al. [1] make use of a bipolar configuration including current collectors. Although rather ambiguous for a single cell, their implementation of a working bipolar design has been carried out with focus on scaling up the design to compare with commercially available electrolyzers. Preliminary estimations for a 150 kW performance results in a stack of 500 cells in a bipolar configuration.

3.4. Zero-gap configuration

The traditional alkaline water electrolyzer configuration utilises a well defined space between the positive and negative electrodes. The distance between the electrodes is commonly filled with electrolyte. The hydroxide ions migrate through the electrolyte to be consumed at the anode. The ion flow feels resistance to the flow due to the electrolyte itself. Consequently, ohmic losses are measured and give way for the overpotential to increase. The zero-gap or near zero-gap configuration is a way to reduce those ohmic losses by placing the electrodes close to or on the diaphragm. Haverkort et al. [29] investigated the effects of the reduced distance between the electrodes and diaphragm. They found that eliminating any space between the diaphragm and electrodes would give very high overpotentials. Partial pore blockage or deposits within the pore openings or electrode openings could explain the decreased performance. However, when introducing a small space of 0.2 mm, losses due to trapped bubbles were mitigated, resulting in a better performance compared to the zero-gap configuration. The paper by Hodges et al. [1] used a zero-gap configuration in their capillary-fed electrolyzer. Tie bolts were used to press the electrodes and separator tightly together and make a leak tight seal. Any space here should be eliminated since the gas production will take place at the sides facing the separator. Furthermore, as there is no electrolyte solution present in which the electrodes are immersed, the tight pressing against the separator is required for any electrochemical reaction to take place. Lavorante et al. [35] experimented with nine different distances between the separator and the diaphragm. These ranged from 3.40 mm up to 10.65 mm. Interestingly, they used a convention where the distance between the cathode and separator is twice that of the distance between the anode and separator. The main justification for this is reaction stoichiometry. Water has a 1:1 stoichiometric relation with hydrogen. In other words, for every two moles of water we generate 2 moles of hydrogen versus one mole of oxygen.

3.5. Capillary-fed configuration

The main protagonist in this master project is the capillary-fed electrolyzer. Figure 3.4 shows how subsequent developments in reducing the cell resistance resulted in the current cell technology. The capillary-fed cell consists of a MEA similar to the zero-gap configuration. The cathode and anode are unchanged from the conventional electrolysis cell. However, as opposed to the (near)zero-gap cell, the electrodes are now tightly pressed to the diaphragm. The MEA is not immersed in an electrolyte solution but instead only a small portion is placed in contact with the electrolyte solution, see Figure 3.4. The capillary-fed configuration employs a means to exploit the hydrophilicity of the separator to draw in fresh electrolyte using capillary forces. By wetting the diaphragm this way, a means of directly producing bulk hydrogen and oxygen gases is made possible. Furthermore, as the MEA is not completely immersed anymore, an inherently bubble free electrolyzer is realized. Resistances due to bubble nucleation and bubble coalescence can now be omitted. Overpotentials caused by the resistance of the electrolyte to the ion flow can also be omitted since direct gas production is realised.

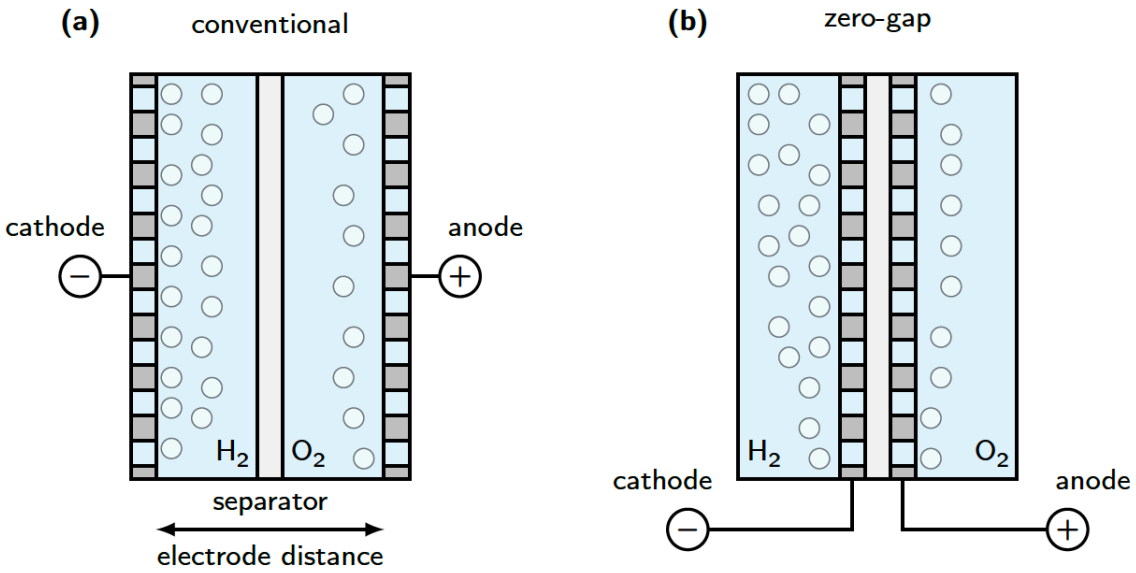

Figure 3.3: a) The conventional MEA for alkaline electrolyzers. b) The zero-gap MEA for alkaline electrolyzers. Retrieved from [15].

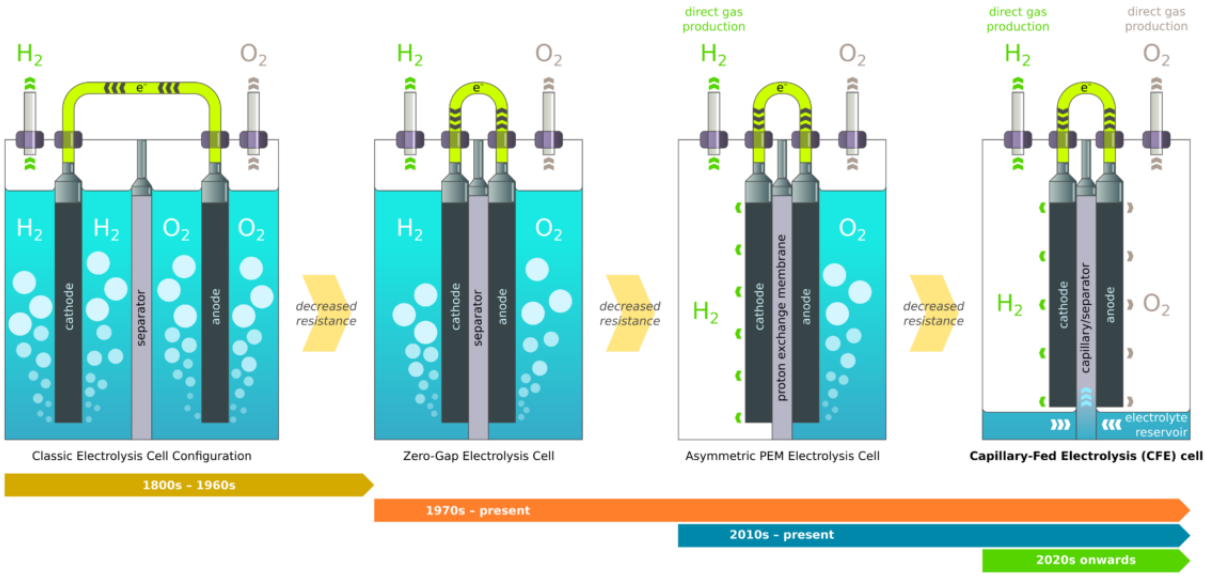

Figure 3.4: Evolution of electrolysis cell from the classic configuration up to the capillary-fed electrolysis cell. Retrieved from [13].

The paper by Hodges et al. [1] presents a capillary-fed electrolysis cell concept in which both product gases are produced directly in gas collection chambers. The design can be seen in Figure 3.5. The cell consists of bipolar plates which functioned also as gas diffusion layers. The choice for bipolar plates for a single cell was made to compare the cell to commercially available electrolyzers cells. A polyethersulfone material was used for the diaphragm. Gas collection chambers and an electrolyte reservoir can be seen as well. Additionally, narrow channels are built in that connect these chambers to the atmosphere. The researchers used a 27wt% KOH solution as the electrolyte which is drawn up by capillary forces through a hydrophilic polyethersulfone (PES) diaphragm. They demonstrated sustained electrolysis up till a height of approximately 18 cm at a current density of $j = 1$ Acm^{-2} and a temperature of at least $T = 80°$C.

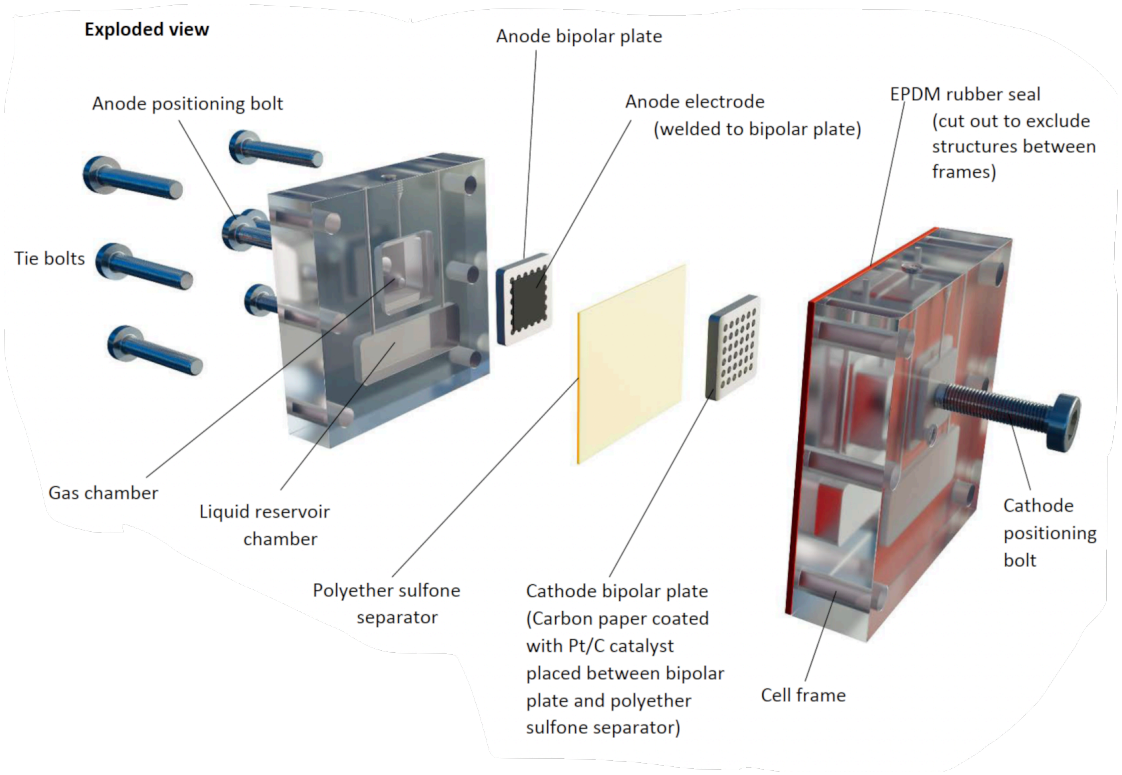

Figure 3.5: Exploded view of the capillary-fed electrolyzer from the study done by Hodges et al. Retrieved from [1][2].

Swiegers et al. provides additional cases of electrolyzers that make use of capillary forces with a lateral 6M KOH electrolyte feed through porous electrodes that are finished with a Goretex membrane which is inherently hydrophobic [39][6]. At $T = 80°$C the Goretex membrane displays gas capillary action by subsequently drawing out gas bubbles from the bulk electrolyte.

Bachelor thesis

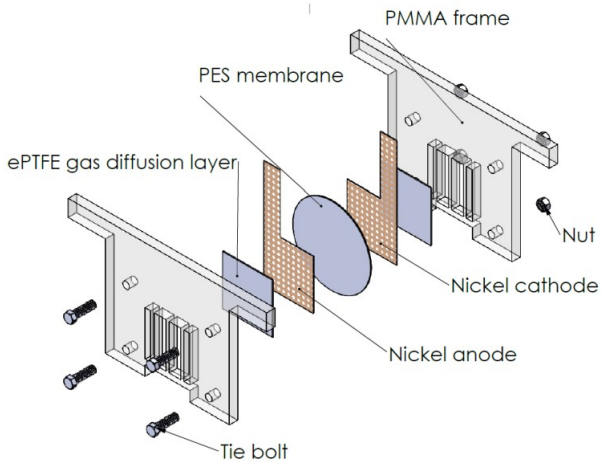

Figure 3.6: Exploded view of the capillary-fed electrolyzer from the Bachelor thesis by Leijn et al. [41]

Figure 3.6 shows the exploded view of the capillary-fed cell built by Leijn et al. [41]. The cell was used to study the capillarity, efficiency and heat production during water electrolysis under clamping and non-clamping conditions. In the presented design, they concluded that most of the electrolyte stays in the bottom of the cell compared to the the top, limiting its ability for heat dissipation to the environment. Loosely clamping the cell proved to be beneficial as the cell efficiency increased by 18% compared to

clamping. Gas diffusion layers improved efficiency by 4% at a current density of 300 mAcm^{-2}.

3.5.1. Gas Diffusion Layers

The use of gas diffusion layers in water splitting processes is not uncommon [39][1][38]. In traditional electrolyzers trapped bubbles lead to a large source of overpotential. Hydrophobic outer layers can be used to directly extract the produced gases while liquid is confined to only one side of the diffusion layer. Expanded Polytetrafluoroethylene (ePTFE) is a commonly used material for gas diffusion layers. It is comprised of microscopic Teflon filaments arranged in a web structure as seen in Figure 3.7. Tiwari et al.[39] describe the use of PTFE based Goretex gas diffusion layers in their electrolyzer. The bubble free electrolyzer comprised of a Nickel mesh PTFE cathode and anode. The electrolyte used was a 6M KOH solution. It was observed that at increasing temperatures the onset potential decreased to approximately $E \approx 1.30$ V at $T = 90°$C. Furthermore, increasing the temperature resulted in an almost linear relation between voltage and current, indicating only a narrow region that is lost to activation overpotential. Winther-Jensen et al. [38] used ePTFE in their electrochemical cell as well. PTFE Goretex membranes were plasma treated, sputtered with gold and then platinum sputtered. No bubbles were observed on the anode and cathode during the experiment.

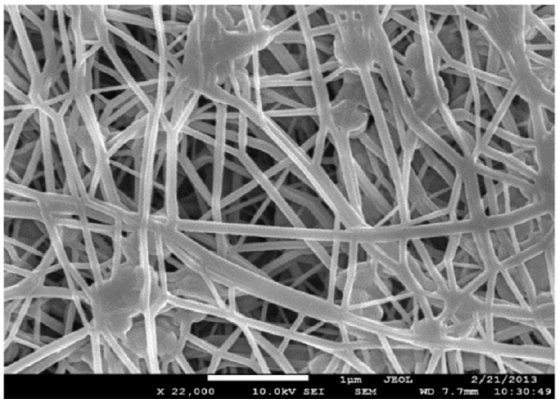

Figure 3.7: Scanning electron micrograph of ePTFE material. Retrieved from [39].

Tsekouras et al. [7] place the focus towards the electrodes themselves. They manufactured and tested an oxygen generating nickel mesh electrode. The porous gas generating electrode was comprised of three separate layers, namely a gas generating primary layer topped with a hydrophobic aerophilic layer to promote gas crossover to the outer hydrophobic ePTFE layer under a pressure differential. Their experimental results have shown that the current density with use of a combination of these layers decreases the required applied potential at a constant current density. Furthermore, visual observation confirmed absence of oxygen bubbles on the electrode surface, indicating that the rate of oxygen generation was in fact lower than or equal to the oxygen extraction through the ePTFE outer layer.

3.6. Capillary-fed electrolyzer design

A small scale capillary-fed electrolyzer was designed in order to perform a variety of experiments early into the thesis. The main objective here was to gain understanding into the working mechanisms and log any complications that might occur during assembly and experimenting. Furthermore, this cell would be a precursor to the final design of a capillary-fed cell. Figure 3.8 shows an exploded schematic of the cell and the cell architecture in detail is tabulated in Table 3.1.

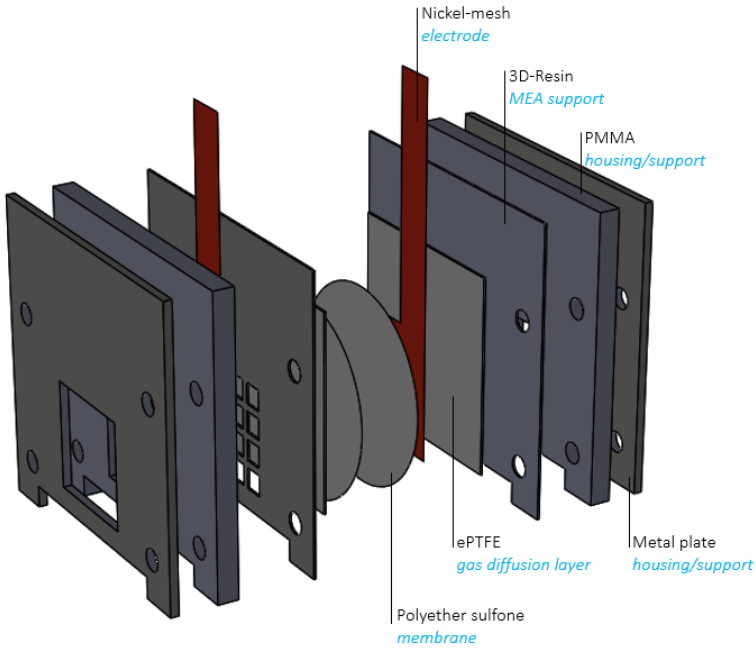

Figure 3.8: Exploded view of the small capillary-fed electrolyzer. The cell has the following architecture: Stainless steel plate - PMMA - 3D printed resin - ePTFE - Nickel mesh - PES - PES - Nickel mesh - ePTFE - 3D printed resin - PMMA - Stainless steel plate.

Cell Architecture

Material	Function	Quantity	Thickness	Dimensions
Unpolished Stainless Steel Gr. 304	Pressure distribution	2	1 mm	70x70 mm plates, 25x25 mm square cut-out, 50x5 mm rectangular cut-out.
PMMA	Pressure distribution/ Frame	2	2 mm	70x70 mm plates, 25x25 mm square cut-out, 50x5 mm rectangular cut-out.
3D-Resin	Membrane-electrode reinforcement	2	0.5 mm	70x70 mm plates, 16 square cut-outs of 5x5 mm.
Expanded PTFE	Gas diffusion layer	2	0.5 mm	25x25 mm.
Nickel Mesh	Gas generating electrode	2	0.5 mm	Flap: 10x70 mm, Center: 25x25 mm.
Polyethersulfone	Diaphragm	2	140 µm	$\varnothing_{membrane}$ = 47 mm, $\varnothing_{pore}$ = 0.45 µm.

Table 3.1: Architecture of the small capillary-fed electrolyzer from Figure 3.8 in detail.

Membrane

Various membranes were researched for their suitability in capillary-fed electrolysis. These are listed below in Table 3.2. The aim is to compare different available membranes. The prerequiste is that all membranes should have their degree of wettability in common, i.e. they should all be hydrophilic. The membranes have been tested and compared to Equation 2.46 where the Lucas-Washburn equation was presented. A mathematical expression of the penetration depth into a capillary over time. Polyethersulfone was chosen as the membrane for the subsequent experiments and final design.

Overview of Membranes					
Membranes	**Manufacturer/ Supplier**	**Pore [μm]**	**Diameter [mm]**	**Thickness [μm]**	**Reference**
Ashless Filter Paper	Whatman	2.5	55	200	[56]
Mixed Cellulose Esters	Sartorius	5.0	47	130	[18]
Nylon Filter	Whatman	0.45	47	150-187	[55]
Polyethersulfone	Dispolab	0.45	47	140	[40]
Zirfon PERL UTP500	Agfa	0.15 $\pm$ 0.05	N/A	500	[47]

Table 3.2: Overview of researched hydrophilic membranes for capillary-fed electrolysis.

Gas diffusion layers
Section 3.5.1 elaborated on the role of gas diffusion layers in electrochemical cells. In order to prevent gas build-up within the pores of the gas diffusion layers a very thin sheet was used. Furthermore, gas should quickly and easily exit the cell. The choice has been made to use 0.5 mm thick Expanded Polytetrafluorethylene (ePTFE[1]) in this cell.

3D-printed resin
The cell should promote a well distributed current as much as possible. However, due to the flimsy nature of the nickel mesh electrode, the choice has been made to add an additional reinforcement plate to evenly press the electrodes to the diaphragm. In order to promote easy gas expulsion a much as possible, the choice has been made to introduce small windows into the material from which gas could escape. 3D printing here ensures that these plate can be printed as thin as possible (sub-millimetre range). Various 3D printing filaments were available, such as Polylactic Acid (PLA) and Acrylonitril-Butadieen-Stryeen (ABS). However, printing with (use of stereolithography (SLA)) resin was chosen since there was a need to print the small square cut-outs. Furthermore, printing with resin also ensures we have a material that can withstand the strong basic electrolyte solutions.

PMMA
PMMA was used to build the cell. It ensures all parts are centered and pressed together through bolts. Additionally, PMMA can withstand high pH solutions.

Metal
Unpolished stainless steel plates are used to finalize the cell. Due to the small architecture, a total of 4 bolts was not enough to ensure even pressure distribution along the cell. Using a metal plate on the outside of the cell, we could ensure a more controlled pressure distribution.

Important design considerations
This cell has had important conclusions for the final design. The main design considerations revolve around the membranes and membrane-electrode reinforcements. Figure 3.8 and Table 3.1 show that two Polyethersulfone membranes were used. It occurred that the flimsy nickel-mesh would puncture the membrane under compression which led to short-circuiting. Consequently, an additional membrane was introduced for extra support. Furthermore, the choice for 3D-printed resin was let go to simplify the final design and prevent risks of degradation of the resin material as it heats up and cools down.

[1] 0.5 mm thick ePTFE sheets were supplied on request by ERIKS N.V. and KLINGER B.V.

3.7. Realized capillary-fed electrolyzer design

A 40 cm tall capillary-fed electrolyzer was designed in order to perform a variety of experiments. The main objective is to gain understanding into the thermal and electrochemical characteristics of the cell along its vertical axis. The cell design is shown in Figure 3.9 and 3.10.

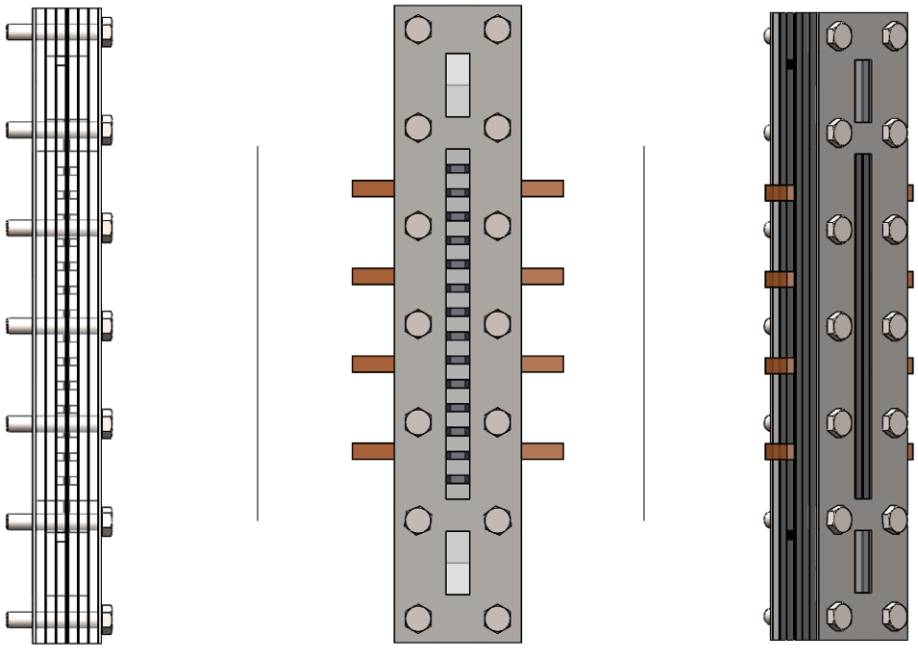

Figure 3.9: Realised design of the segmented capillary-fed electrolyzer. Left: side view. Middle: front view, Right: isometric view showing the square inlets to the upper and lower electrolyte reservoirs.

Figure 3.10: Design of the segmented capillary-fed electrolyzer. Left: Isometric side view, showing the inlets to the reservoirs. Right: Front view.

An exploded view can be seen in Figure 3.11 and details on the cell architecture are tabulated in Table 3.3. The utilised membrane strips uninterruptedly span almost the complete length of the cell to ensure that it sticks out into the top and bottom reservoirs for capillary imbibition. A similar approach has been taken with the gas diffusion layer strips. However, these only uninterruptedly span the complete middle section of the cell, where the bulk gases are produced. There are key differences that distinguish it from the small cell introduced earlier, such as the introduction of electrode segments and electrolyte reservoirs.

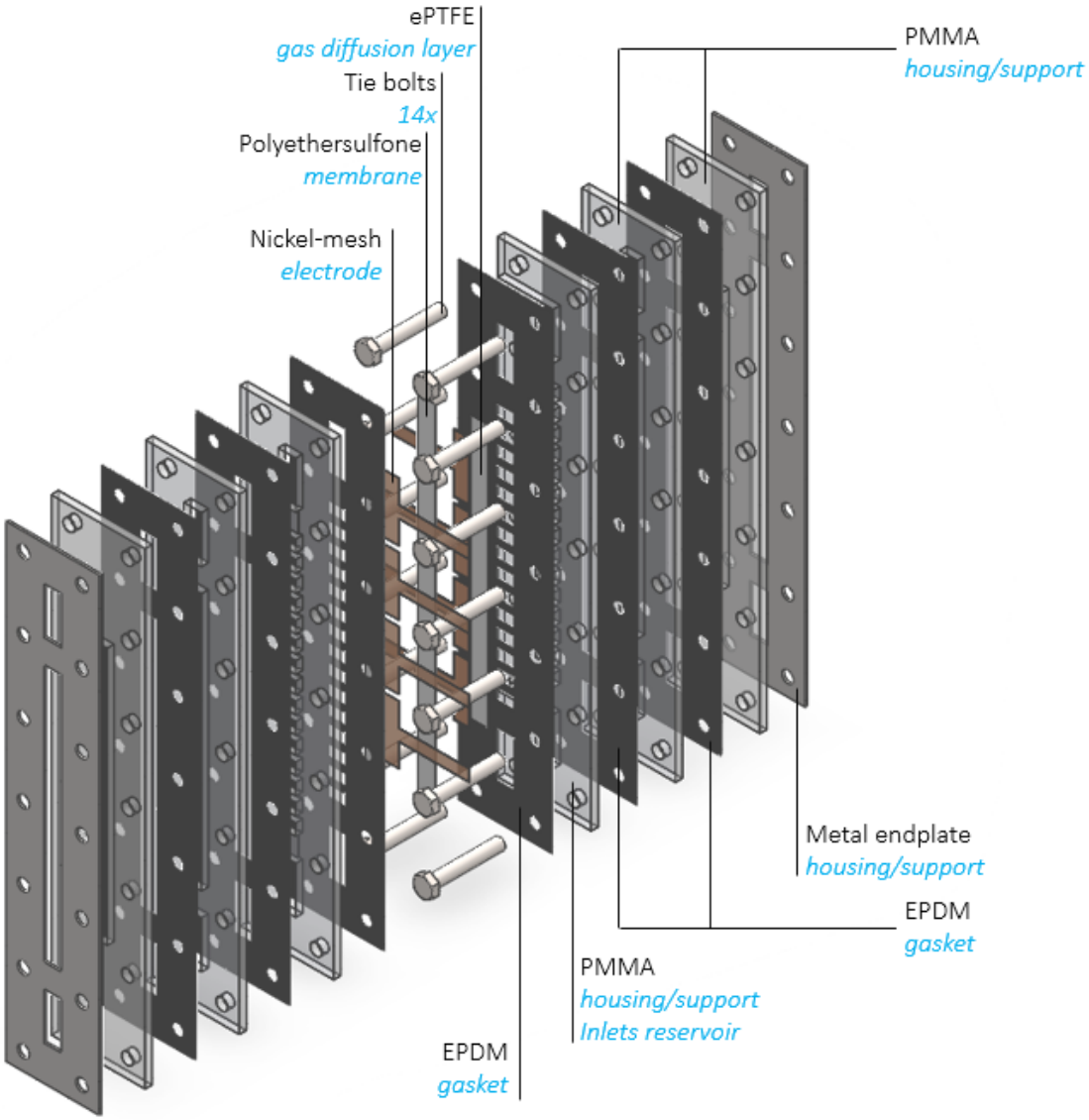

Figure 3.11: Exploded view of the realised segmented capillary-fed electrolyzer. The cell has the following architecture: Stainless steel plate - PMMA - Gasket - PMMA - Gasket - PMMA - Gasket - ePTFE GDL - Nickel mesh electrodes - PES membrane 2x - Nickel mesh electrodes - ePTFE GDL - Gasket - PMMA - Gasket - PMMA - Gasket - PMMA - Stainless steel plate.

Cell Architecture				
Material	**Function**	**Quantity**	**Thickness**	**Dimensions**
Stainless Steel Tie Bolts	Pressure distribution; (Leak) tightening	14	M10	$\varnothing_{\text{bolt}} = 10$ mm, $L_{\text{thread}} = 60$ mm.
Unpolished Stainless Steel Gr. 304	Pressure distribution	2	2 mm	80x400 mm plates, 15x40 mm square cut-out *(2x; reservoirs)*, 15x220 mm rectangular cut-out.
PMMA	Pressure distribution/ housing/support	4	6 mm	80x400 mm plates, 15x40 mm square cut-out *(2x; reservoirs)*, 15x220 mm rectangular cut-out.
PMMA	Membrane-electrode reinforcement	2	6 mm	80x400 mm plates, 15x40 mm square cut-out *(2x; reservoirs)*, 10x15 mm rectangular cut-out *(15x; 5 mm spaced)*.
EPDM	Rubber gasket; Leak tightening	6	0.5 mm	80x400 mm sheets, 15x40 mm square cut-out *(2x; reservoirs)*, 15x220 mm rectangular cut-out.
Expanded PTFE	Gas diffusion layer	2	0.5 mm	15x220 mm rectangular strips.
Nickel Mesh	Gas generating electrode	8	0.5 mm	Flap: 10x60 mm, Center: 13x50 mm.
Polyethersulfone	Diaphragm	2	140 µm	$\varnothing_{\text{membrane}} = 47$ mm, $\varnothing_{\text{pore}} = 0.45$ µm.
Electrolyte Reservoirs, Channel & Inlets				
Item	**Dimensions**	**Volume**	**Function**	
Top Reservoir	15x40x44.5 mm	26.7 ml	Facilitate top-down wetting through capillary wicking.	
Bottom Reservoir	15x40x44.5 mm	26.7 ml	Facilitate capillary rise of electrolyte.	
Channel	0.15x9x220 mm	0.30 ml	Facilitate capillary dynamics towards gas generating section.	
Inlet	6x6x32.5 mm	1.17 ml	Electrolyte injection into reservoirs.	

Table 3.3: Detailed description of the segmented capillary-fed electrolyzer architecture as shown in Figure 3.11.

3.7.1. Working Principle

The capillary-fed electrolyzer is designed to obtain insight into the thermal characteristics of the cell as a function of height, current density and cell potential. Furthermore, insight into how electrolyte feed from the bottom compares to feed from the top should yield interesting results when we look at heat transfer. Electrolyte introduced to the cell from either the bottom or top reaches the whole length of the cell through capillary imbibition. Water electrolysis takes place at every electrode pair and should result in an autonomous feed of fresh electrolyte due to water evaporation at the electrodes. This feed is established due to an increased concentration of KOH at the electrodes which would lead to a capillary flow of electrolyte through osmosis and hydrophilic nature of the membrane.

3.7.2. The segmented cell

The segmented cell contains 4 pairs of nickel mesh electrodes. Connecting every electrode pair to its own power supply would give valuable insight into the current distribution along the vertical axis of the cell and what influence a top-down wetting has compared to bottom-up wetting or even a dual feed wetting. Utilising single large electrodes, spanning the whole length would not only result in an inhomogeneous current distribution, i.e. electrons would easily take a horizontal path instead of also reaching the outskirts of the electrode area, but would also prevent any valuable data regarding the current distribution along the vertical axis of the cell. The measured potential and current would be averages over the whole cell whereas utilising segments would give more insight into what dynamics are at play along predefined heights along the cell. Hine et al. [27] approached their one meter tall electrolyzer in a similar manner. The cell had a 10 segment electrode division to obtain the current distribution along the vertical length of the cell to research the effects of electrolytic bubbles on the ohmic drop of caustic soda solutions. Czarnetzki et al. [31] divided the working electrode of their vertical cell into 20 segments to research the influence of various parameters on the current distribution along the length of the cell. These parameters are e.g. the gas void fraction, temperature, electrolyte concentration and size of separator-electrode gap.

3.7.3. Housing architecture

Figure 3.11 shows a distinct number of PMMA plates all of which have a specific purpose next to those that they have in common. All plates are utilised for structural rigidity and to provide depth into the electrolyte reservoirs. PMMA plates directly adjacent to the MEA assembly incorporate a set of two inlets for the top and bottom reservoir respectively. Furthermore, these plates introduce a ”ladder” profile which ensures the gas diffusion layers and flimsy electrodes are evenly pressed against the membrane strips running along most of the vertical length of the cell. To ensure that liquid could still reach the remaining part of the membrane through capillary dynamics, a narrow channel has been milled for the membrane to relax and keep its pores open rather than pressed shut. Appendix B.2 and Figure B.2 show the milling work that has been done on the PMMA plates adjacent to the MEA assembly. The outer two PMMA plates function as spacers and end plate, respectively. In which the latter provides the reservoir wall. EPDM rubber gaskets are used between PMMA plates to ensure a leak tight cell.

3.7.4. Electrolyte feed

Important in the design was the location of the in- and outlets to the electrolyte reservoirs. The choice for introducing the inlets on the same side eases cleaning, flushing and ensures experiments can be done while laying the cell in a horizontal position to exclude the influence of gravity on capillarity.

4

Methods

Two capillary-fed electrolyzers have been presented in the previous section. Added to these two, a zero-gap electrolyzer built by Haverkort et al. [29] has been utilised to perform experiments. This cell is shown on Figure 4.1. The aim of this section is to lay out the experimental groundwork to answer the subquestions posed in section 1.1 and finally answer the main research question. Table 4.1 shows a brief summary of the experiments that will be presented in this section. All mentioned electrolyte solutions are prepared with 85% purity KOH pellets from Sigma-Aldrich [44].

Overview of Experiments

Name	Used Cell	Objective
Variation of electrolyte level	Zero-gap; Small cell	Compare different membrane materials when the electrolyte level is lowered.
Capillary rise	Diaphragm only; Small cell; Segmented cell	Research capillary dynamics and degree of imbibition.
Horizontal capillary penetration	Segmented cell	Research capillary dynamics and degree of imbibition in absence of gravity effects.
Constant current	Small cell; Segmented cell	Cell performance (j, U, T) over time.
Contact angle	Diaphragm only	Research surface tension effects of different KOH concentrations.
Constant current bottom-up	Segmented cell	Cell performance (j, U, T) over time.
Constant current top-down	Segmented cell	Cell performance (j, U, T) over time.

Table 4.1: Brief overview of experimental work. The cell used during the experiments and the objective of the study have been shown.

4.1. Variation of electrolyte level

The objective of these experiments is to compare different membrane materials on their performance when the electrolyte level is lowered. Hence, the aim is to promote direct-gas production with every subsequent lowering of the level and measure which material performs better over time. The cells in question have a zero-gap configuration and can be seen in Figure 4.1. The materials used are tabulated in Table 4.2. The initial condition for both cells is complete immersion in electrolyte, i.e. specifically the electrodes should be completely immersed.

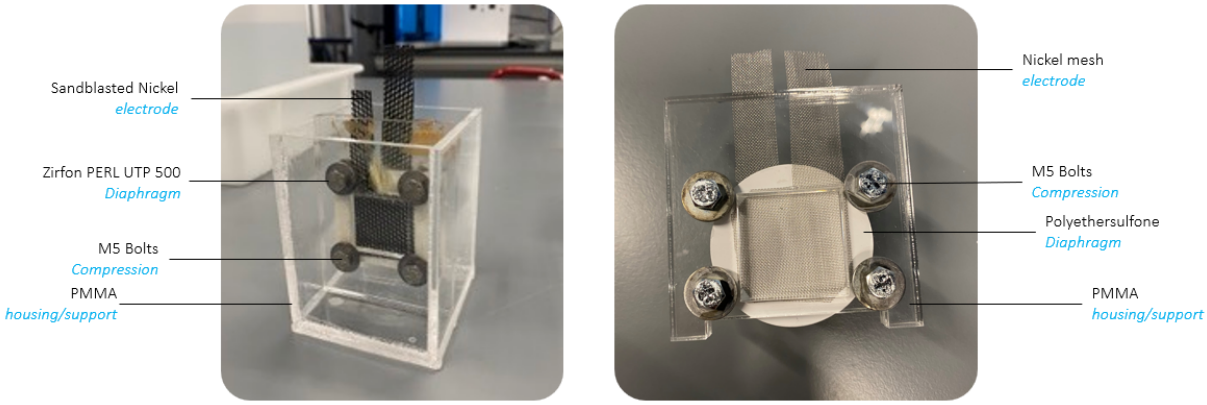

Figure 4.1: Cells used for the level height variation experiments.
Left: the zero-gap cell by Haverkort et al [29]. Right: Small cell.

Setup Summary			
	Zero gap cell from [29]	**Small cell**	Units
Electrode Material	Sandblasted Nickel	Nickel mesh	-
Electrode Area	3.5x3.5	3.0x3.0	cm^2
Separator Material	Zirfon PERL UTP500	Polyethersulfone	-
Separator Thickness	500	140 (x2)	μm
Separator Poresize	0.15	0.45	μm
Electrolyte	1M KOH	1M KOH	$mol \cdot L^{-1}$
Applied Potential	2.0	3.0	V
DC Power Supply	Delta Elektronika SM 15-200 D	Delta Elektronika SM 45-140	-
Ambient Conditions	Room Temperature	Room Temperature	°C

Table 4.2: Parameters for the level height experiments.

4.2. Capillary rise

The capillary rise experiments have been conducted to exploit the Lucas-Washburn equation as described in Equation 2.46. Furthermore, the effects of degree of compression on capillary rise were of interest. Capillary rise has been monitored from observation, by use of pH paper and by use of tracers such as fluorescein salt. The diaphragms of interest are tabulated in Table 4.3.

Overview of Diaphragms		
Material	**Pore diameter [μm]**	**Disc diameter [mm]**
Polyethersulfone	0.45	47
Nylon Filter	0.45	47
Filter Paper	2.5	55
Mixed Cellulose Esters	5.0	47

Table 4.3: Overview of diaphragms of interest for capillary rise experiments.

4.2.1. Horizontal capillary penetration

The above experiments were extended to include a horizontal setup, primarily in the case of the segmented cell. By placing the setup in a horizontal configuration, we could investigate the capillary imbibition while excluding any gravity effects that could potentially influence capillary rise. Liquid was injected from either the top or bottom reservoir, resulting in either a left-to-right wetting or a right-to left wetting.

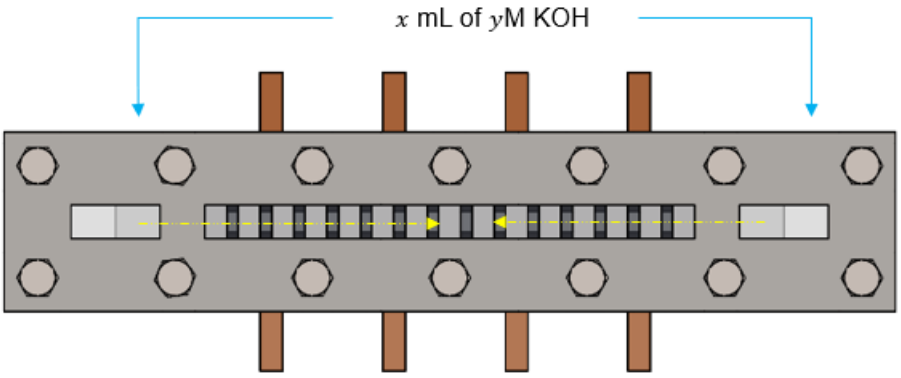

Figure 4.2: Schematic for the horizontal capillarity experiments.

4.3. Constant current

The small cell has primarily been utilised to research cell performance over time. Current density and temperature were recorded at certain applied potentials for given electrolyte concentrations. The experimental setup is shown schematically on Figure 4.3. A single Delta Elektronika SM 45-140 programmable DC power supply has been used to power the cell and a FLIR E75 infrared camera is used for thermal imaging. The power supply is connected to a computer for logging and subsequent data processing using MATLAB v2022 and Excel 2023 software. The FLIR Camera is operated through ResearchIR software.

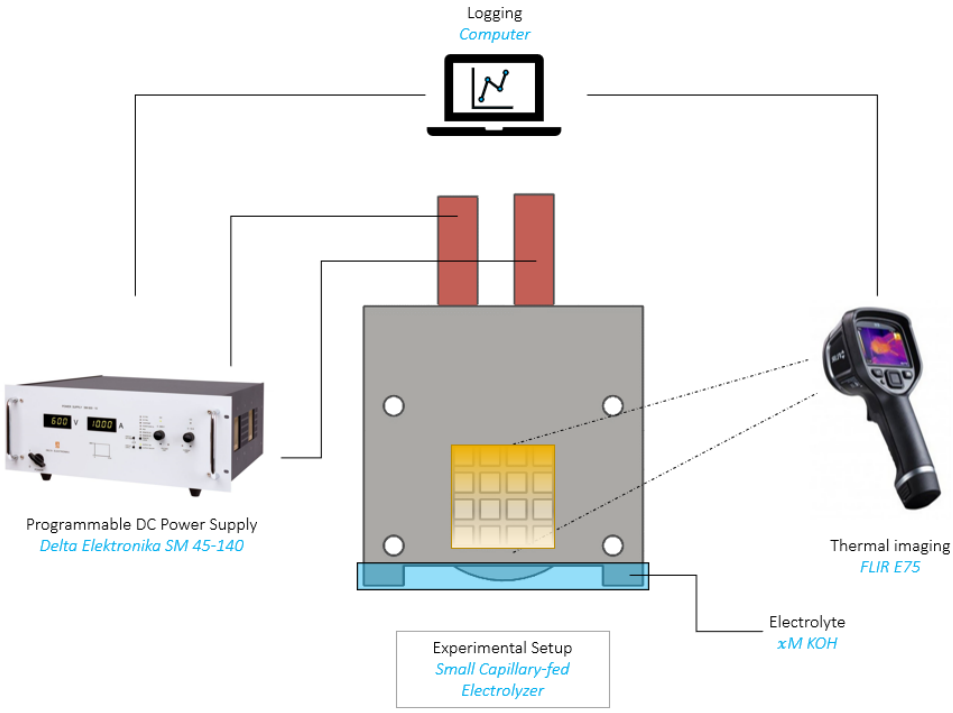

Figure 4.3: Experimental setup used for the small cell. Shown are the cell and the equipment used to log voltage, current and temperature. Images for power supply and camera are retrieved from [20] and [53], respectively.

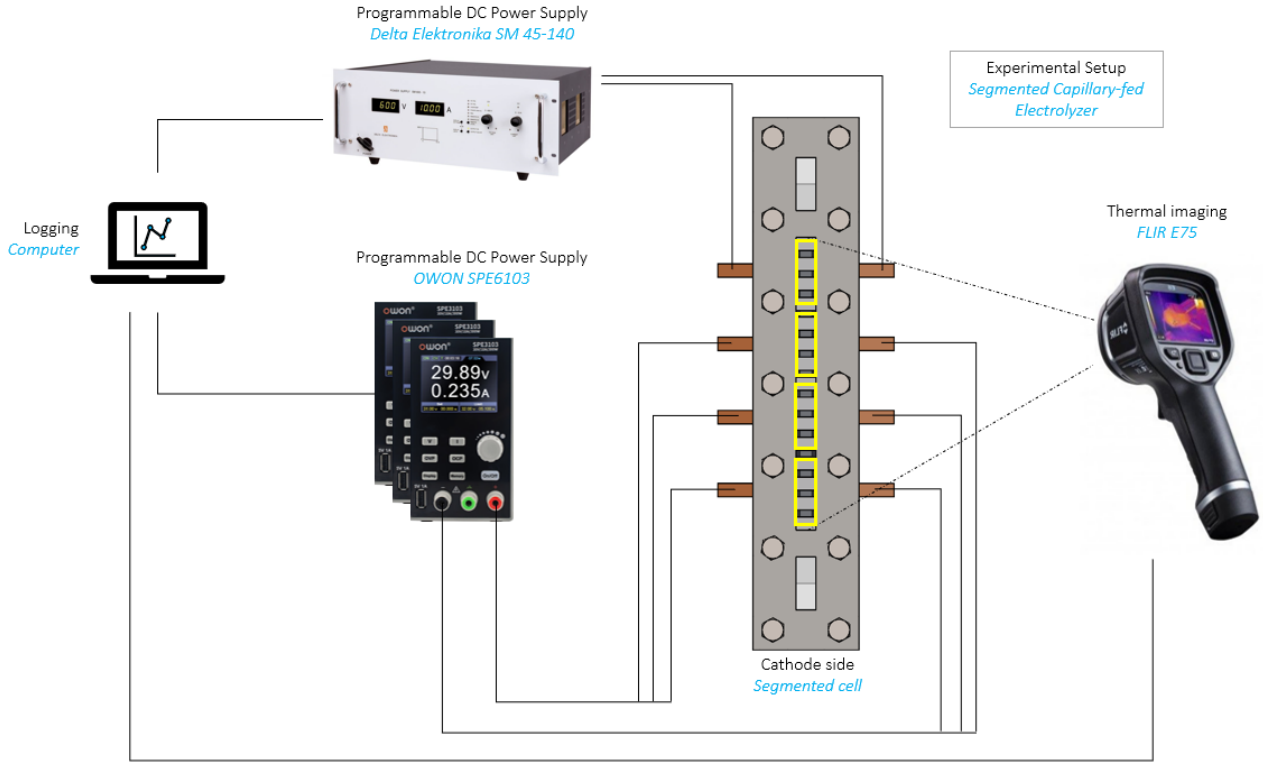

Figure 4.4: Experimental setup used for the vertical cell. Shown are the cell and the equipment used to log voltage, current and temperature. Images for power supplies and camera are retrieved from [20], [23] and [53], respectively. The yellow arced regions show the segments.

The constant current experiments were the primary focus within the thesis. For the segmented cell the current distribution over the vertical axis of the cell was of interest. The experimental setup for the segmented can be seen in Figure 4.4. Two different programmable DC power supplies have been used to power the four segments. These are a Delta Elektronika SM 45-140 unit, primarly connected to the top segment, and three OWON SPE6103's for the remaining three segments. To obtain temporal temperature data the same infrared thermal imaging camera has been used as with the small cell. This has primarily been focused on the hydrogen - or cathode - side. Specifically for the segmented cell a sub-classification of experiments was designed which will be highlighted below.

4.3.1. Constant current bottom-up

The current distribution along the segmented vertical cell was of interest in these experiments. By only feeding electrolyte from the bottom reservoir we could research capillary-fed electrolysis, water consumption, temperature evolution and presence of precipitation at given electrolyte concentrations. Furthermore, the duration for which the cell could sustain electrolysis was researched. The membrane was made sure to be saturated with electrolyte solution ahead of starting these experiments.

4.3.2. Constant current top-down

Feeding electrolyte from the top with the aid of gravity was studied in the constant current top-down experiments. Compared to the constant current bottom-up experiments, we have more control of the temperature evolution along the cell and the accompanied potential evolution. To deal with a possibly supersaturated membrane, the setup as shown in Figure 4.5 was designed.

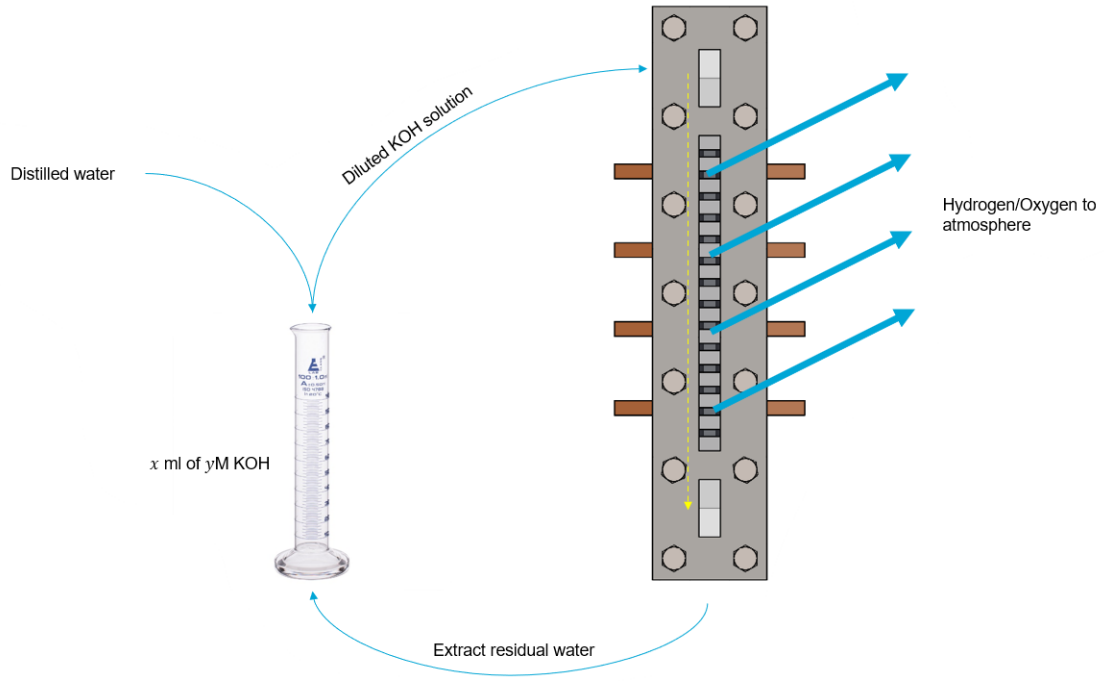

Figure 4.5: Constant current top-down experiments with dilution process. The residue electrolyte drips down into the bottom reservoir. This residue is extracted and diluted with distilled water before being reintroduced into the top reservoir.

After saturating the membrane with a fresh electrolyte solution, a constant current was applied to the cell. As will be shown later, some of the yM KOH electrolyte introduced in the top reservoir makes its way to the bottom reservoir. Effectively, the difference between the top and bottom reservoir volume is the amount of water, V_{evap}, that has presumably been evaporated during electrolysis. To account for precipitation at the electrodes the bottom residual volume, V_{bott}, is extracted and added to a separate container with x millilitres of yM KOH solution. The difference between the initial container volume and the current volume will be compensated by dilution with distilled water, V_{inject}, until the initial container volume, $V_{0,\text{cont}}$, is reached. Subsequently, this diluted solution is then introduced to the top reservoir and to the KOH crystals potentially present at the electrode segments to reestablish the KOH concentration

that was initially present. Iteratively this reads:

$$V_{0,\text{cont}} = V_0 \tag{4.1}$$
$$V_{i,\text{top}} = V_{\text{i,inject}} \tag{4.2}$$
$$V_{i,\text{bott}} = V_{i,\text{top}} - V_{i,\text{evap}} \tag{4.3}$$
$$V_{i,\text{add}} = V_{0,\text{cont}} - V_{\text{i,inject}} + V_{i,\text{bott}} \tag{4.4}$$

In which $i = \{1, \ldots, n\}$ is the amount of refills - or flushing - cycles into the experiments.

4.4. Contact angle

Contact angle measurements were carried out using a Theta Lite Optical Tensiometer, specifically for the polyethersulfone material that is used as a diaphragm. Figure 4.6 shows the schematic of a droplet on a hydrophic substrate. The surface tension between the liquid-gas, solid-gas and solid-liquid interfaces are represented as $\gamma_{\text{LG}}, \gamma_{\text{SG}}$ and γ_{SL}. The contact angle between substrate and droplet is shown as θ_{C}.

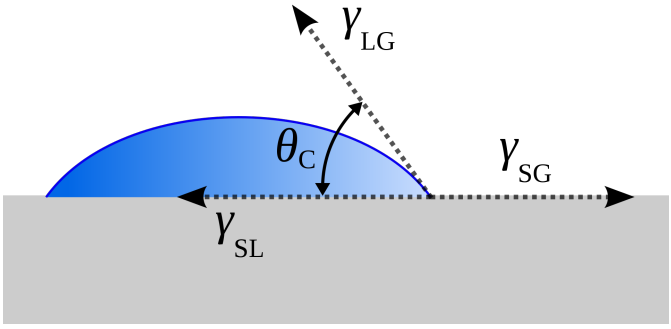

Figure 4.6: Droplet with contact angle θ_{C} on solid substrate. Shown are the solid-liquid interfacial energy, γ_{SL}, solid-gas interfacial energy, γ_{SG} and gas-liquid interfacial energy, γ_{LG}.

Figure 4.7 shows the schematic of the experimental setup and Appendix B.3 shows the experimental setup as it is in the lab. The setup illuminates a droplet of KOH solution and a camera logs the contact angle (evolution) over time.

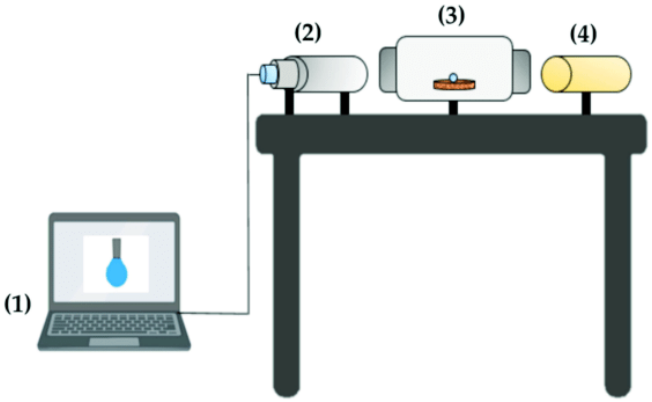

Figure 4.7: Schematic of the working principle of the Theta Lite Optical Tensiometer. 1) Software, 2) Camera, 3) Substrate with droplet and 4) Light source. Retrieved from J. Archila et al. [8]

Although the polyethersulfone membrane is of hydrophilic nature, the KOH solution may pose to be a limiting factor insofar capillary imbibition goes. Increasing the concentration of the KOH solution also increases its surface tension, density and dynamic viscosity. Consequently, a difference in cell performance can be expected. Since the membrane substrate is of hydrophilic nature, we also take into account the contact angle evolution over time. This will be discussed in the following section.

5

Results and Discussion

The Results and Discussion section presents the outcome and evaluation of experimental work with respect to capillary-fed electrolysis. The results will be presented following the order that is given within the Methods section.

5.1. Capillary rise

Various experiments have been carried out to research membrane performance. The effects of membrane compression has been studied with the different diaphragms as was presented in Table 3.2. Membrane compression is of great importance for cell design and capillary-fed electrolysis. Closing the pores under compression would not yield any mass flux into the capillary tubes. The diaphragm materials compared in this section are polyethersulfone, filter paper, mixed cellulose esters and nylon.

Uncompressed diaphragms

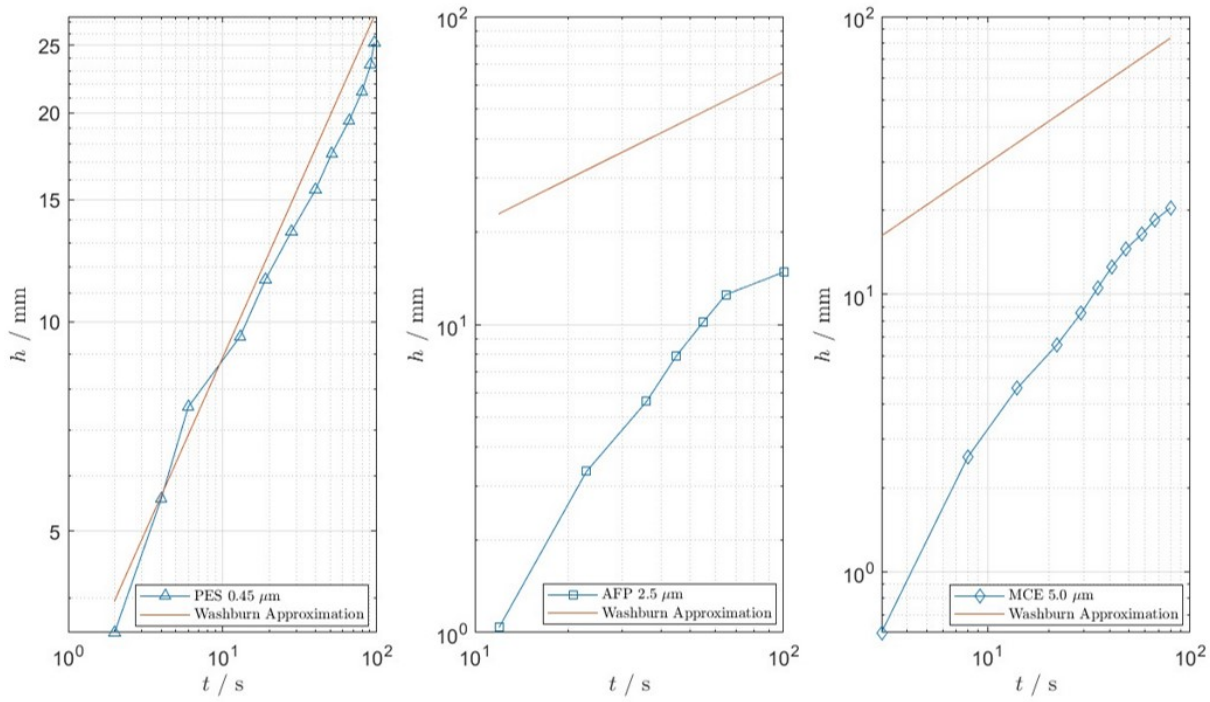

Figure 5.1: Penetration depth versus time for various membranes. Left: 0.45 μm Polyethersulfone (PES), Mid: 2.5 μm Ashless Filter Paper and Right: 5.0 μm Mixed Cellulose Esters. The plots shows the membranes without compression through tie bolts. Lucas-Washburn approximation follows Equation 2.46 with $\theta = 30°$ at standard conditions for water.

Figure 5.1 shows the penetration depth over time on a log-plot with water as the medium. Additionally, the penetration depth as modelled through the Lucas-Washburn approximation (Equation 2.46) has been added. Room temperature and a contact angle with the capillary tube wall of $\theta = 30°$ has been assumed for the Lucas-Washburn approximation. Furthermore, standard properties of water have been assumed at this temperature. Polyethersulfone shows to follow the Lucas-Washburn approximation reasonably well over time. Ashless Filter Paper and Mixed Cellulose Esters show evident increasing trends over time. However, the modelled approximation shows an up to 7 times higher penetration depth at the same time for Ashless Filter Paper and even up to 8 times higher for the Mixed Cellulose Esters.

Compressed diaphragms

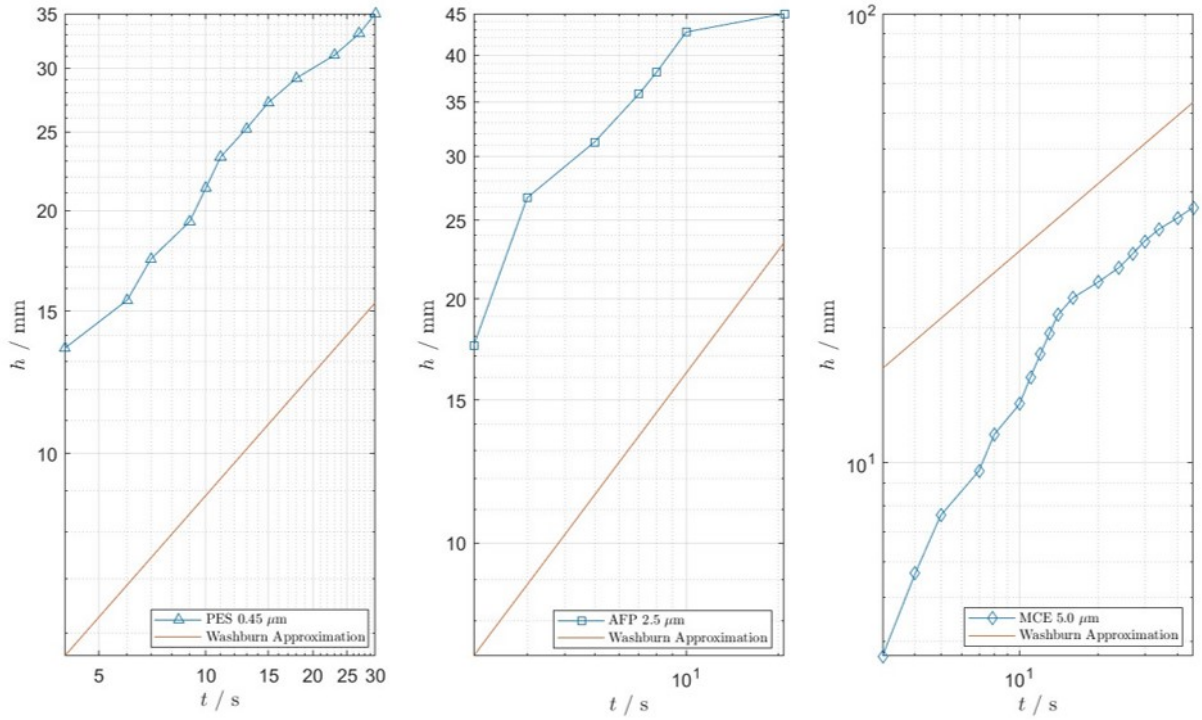

Figure 5.2: Penetration depth versus time for various membranes. Left: 0.45 μm Polyethersulfone, Mid: 2.5 μm Ashless Filter Paper and Right: 5.0 μm Mixed Cellulose Esters. The plots shows the membranes with compression through tie bolts. Lucas-Washburn approximation follows Equation 2.46 with $\theta = 30°$ at standard conditions for water.

Figure 5.2 presents the same diaphragms, now with tie bolts utilised to further tighten the cell. Similar conditions have been applied here as with no compression. From these plots the rapid effect of slight compression becomes evident. Polyethersulfone exhibits up to 2 times deeper penetration compared to no compression. This indicates that slight compression of the pores aids penetration velocity greatly for polyethersulfone materials with a pore size of this magnitude. Similarly, Ashless Filter Paper now has its trend opposite to the Lucas-Washburn approximation. Furthermore, the penetration profile shows only up to 0.65 times increase in penetration depth at the same time. The Mixed Cellulose Esters membrane still underperforms the Lucas-Washburn approximation. The measurements still deviate from a factor of 8 at the start of the experiment to roughly 1.7 towards to end.

Scaling of capillary rise with time

Plotting the capillary rise against time on a log scale could give insight into whether or not compressed pores still follow a power law and more importantly if this is similar to the Lucas-Washburn approximation that scales the capillary rise against time via:

$$L \propto t^n \tag{5.1}$$

With $n = 0.5$. Furthermore, fitting the Lucas-Washburn approximation to the capillary rise measurements can give insight into the effective pore size. Figures 5.3 and 5.4 iterate the Lucas-Washburn-approximation for varying pore radii. The graph shows that the 0.45 μm PES diaphragm has reasonable similarity with an effective pore radius of 0.20 μm. A 49% decrease in pore radius. Interestingly, under compression the capillary rise in polyethersulfone agrees reasonably well with the Lucas-Washburn equation. In other words, Polyethersulfone material exhibits a trend similar to a power law as it scales with $L_{\text{PES}} \propto t^{1.30}$. Similar experiments for Filter Paper and Nylon Filter Membranes are shown in Appendix C.2. Ashless Filter Paper clearly shows scaling of the form $L_{\text{AFP}} \propto t^{0.15}$ whereas compression results in a profile for which $L_{\text{AFP}} \propto t^{6.0}$. For Nylon no compression shows measurements close to $t^n \to t^{0.07}$ and under compression a profile that clearly deviates from the Lucas-Washburn approximation. These findings are summarised in Table 5.1.

Time Exponents

Material	Pore diameter [μm]	Time exponent t^n No compression	Time exponent t^n Compression	Figure
Polyethersulfone	0.45	0.20	1.30	5.3, 5.4
Ashless Filter Paper	2.5	0.15	6.0	C.3, C.4
Nylon Filter	0.45	0.07	$0.20 \leq n \leq 1.60$	C.5, C.6

Table 5.1: Time exponents for diaphragms of interest from (un)compressed capillary rise experiments.

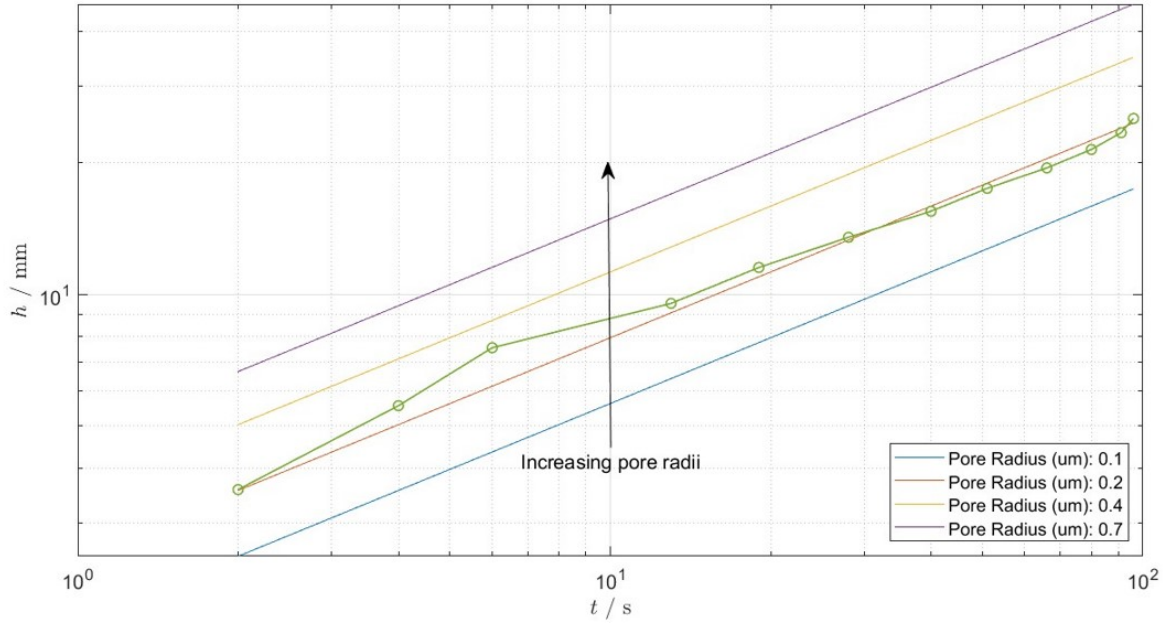

Figure 5.3: Penetration depth versus time for uncompressed 0.45 μm Polyethersulfone diaphragm. Lucas-Washburn approximations have been plotted to show what pore radii suit the membrane in question. Lucas-Washburn approximation follows Equation 2.46 with $\theta = 30°$ at standard conditions for water.

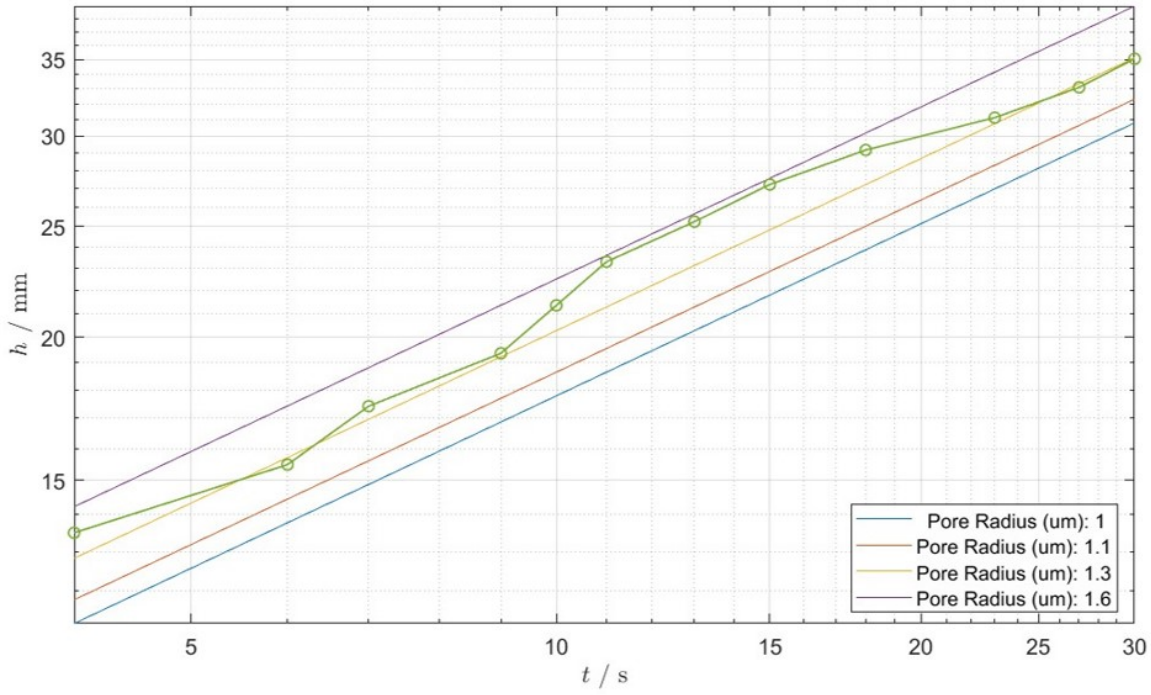

Figure 5.4: Penetration depth versus time for compressed 0.45 μm Polyethersulfone diaphragm. Lucas-Washburn approximations have been plotted to show what pore radii suit the membrane in question. Lucas-Washburn approximation follows Equation 2.46 with $\theta = 30°$ at standard conditions for water.

The presented results show that divergence from the Lucas-Washburn approximation is not uncommon when different membrane materials are compared. At submillimeter scale various effects could explain the difference between the compression and non compression plots. The Lucas-Washburn equation assumes smooth channels and does not take into account the wall roughness, ϵ and turtuosity, τ [54]. Additionally, this could be a measure for the hydrophilicity of the different materials and thus a measure for the rate of imbibition of water. Cai et al. [16] confirms that turtuosity has not been taken into account and has an effect on the capillary imbibition and on experimental results that compare with the Lucas-Washburn approximation.

Since Polyethersulfone material shows reasonable agreement with the Lucas-Washburn approximation (lest it be for a different time exponent), the material is very hydrophilic, can handle strong basic environments and high durability at elevated temperatures, it has been the chosen as the diaphragm for the vertical cell.

5.2. Relation KOH concentration and capillarity

In this section the influence of molality on capillary-fed electrolysis is researched through knowledge gained by performing contact angle experiments. Increasing the molality of a KOH solution increases the temperature dependent ionic conductivity through Equation 5.2 [25]:

$$\kappa = A(M) + B(M^2) + C(M \cdot T) + D\left(\frac{M}{T}\right) + E(M^3) + F(M^2 \cdot T^2) \tag{5.2}$$

With M the molality of the KOH solution, T the temperature in Kelvin and $A, \ldots, F$ constants reported by Gilliam et al. [25]. Graphically, this is represented in Figure 5.5.

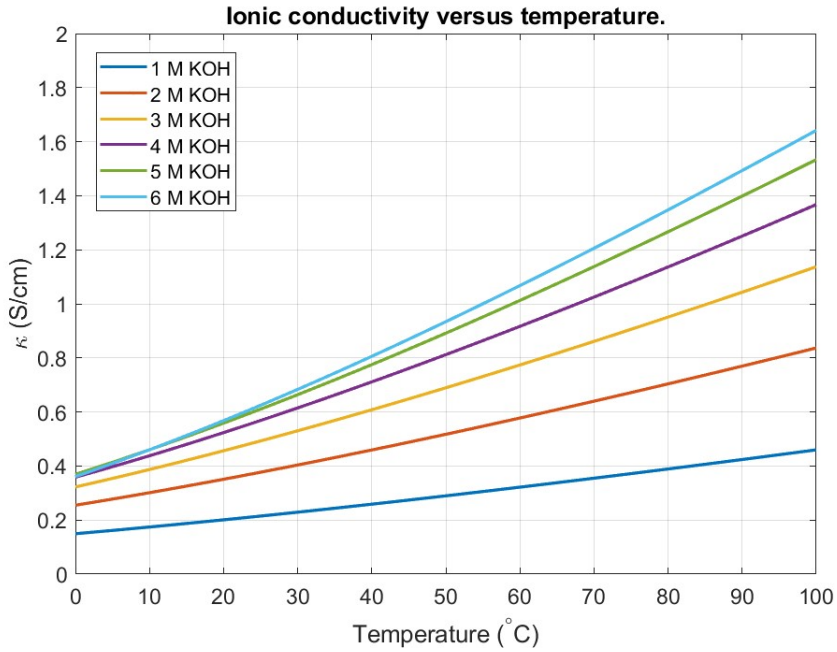

Figure 5.5: Ionic conductivity (S/cm) against temperature (°C) for different molalities of acqeous KOH.

The weight percent concentration of KOH can be converted to molality via Equation 5.3.

$$\text{wt\%}_{\text{KOH}} = \frac{100 \cdot M \cdot M_{\text{w}}}{\rho} \tag{5.3}$$

With the density of the KOH solution, ρ, expressed in units of kg·m^{-3} and the molar mass of KOH, M_{W}, in units of g·mol^{-1}. Hodges et al. [1] worked with a 27wt% KOH solution. Expressed in molality of KOH this translates to roughly a 6M KOH solution for their cell. Initial membrane wetting tests were performed. The aim was to verify if and how fast and deep liquid would rise or fall. For a 6M KOH solution, very poor capillary dynamics were observed. Capillary action was evident in similar tests utilising tap water, 1M KOH and 2M KOH. The difference in behaviour could be explained if we look at the properties of 6M KOH. Compared to 1M KOH, the dynamic viscosity, μ and density ρ of 6M KOH are equal to 1.902 mPa·s and 1260 kg·m^{-3}. In the vertical direction Jurin's law equates the hydrostatic force and surface tension force as:

$$2\pi r\gamma \cos\theta = \rho g h \pi r^2 \tag{5.4}$$

With r the capillary tube radius, h the penetration depth and g the gravitational acceleration. This shows the how the final penetration height is a function of surface tension and contact angle. However, Jurin's law incorporates a gravity term which could also be the limiting factor in the strip of polyethersulfone membrane that we use.

Excluding gravity

To exclude gravity effects, the segmented cell was placed in a horizontal configuration and both a 6M KOH and 1M KOH solution have been injected into the electrolyte reservoirs. A few crystals of fluorescein sodium salt ($C_2OH_{10}Na_2O_5$) have been introduced to both solutions such that it would act as a tracer whilst capillary action was taking place. The plot in Figure 5.6 is the result.

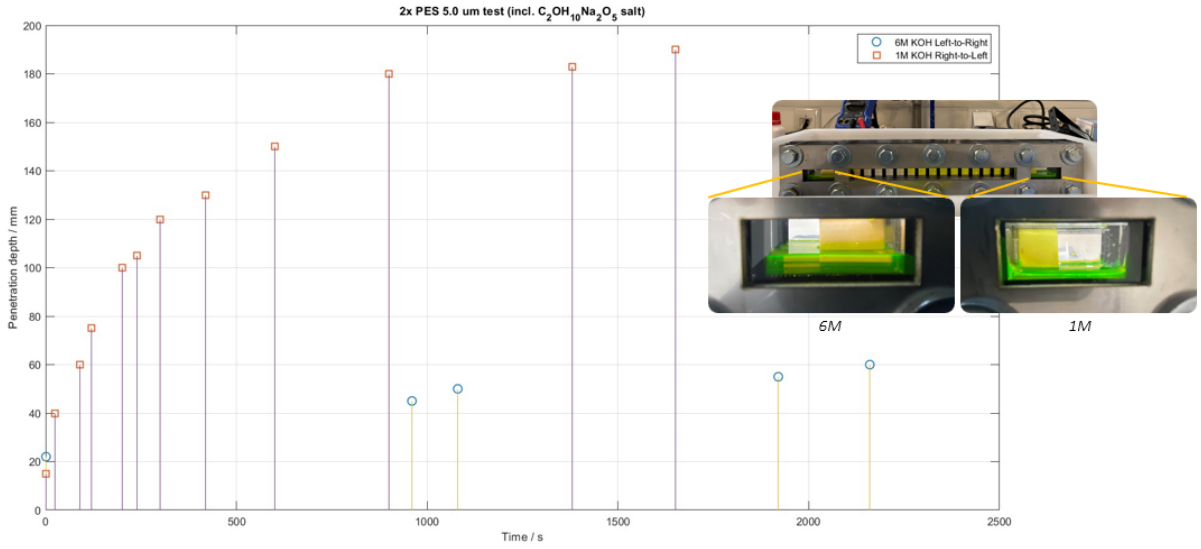

Figure 5.6: Penetration depth into the horizontal direction for both 1M (right reservoir, top right inset) and 6M (left reservoir, top left inset). Two polyethersulfone membranes with porediameter 5.0 μm have been used in the cell to prevent potential puncturing of the membrane during electrolysis.

The measurements show a large difference in penetration depth over time. The 6M KOH solution shows poor penetration into the polyethersulfone material, seen from the inhomogeneous white/yellow color saturation. The 1M KOH solution shows relatively good activity over time. After approximately 2000 seconds the 1M KOH solution has penetrated roughly 3 times as deep compared to 6M KOH. The tracer completely saturates the membrane and can also be seen to traverse from right to left in the top inset picture. From this experiment gravity seems not to be predominantly influencing the effect that high concentration KOH has on capillary imbibition.

5.3. Contact angle experiments

Contact angle measurements were performed to gain insight into how a high concentration KOH droplet would interact with the polyethersulfone membrane. It should be noted that this experiment is only meant to give insight into the solid-liquid interaction. In other words, we utilise a hydrophilic substrate opposed to a hydrophobic substrate. Hence, the contact angles that are measured should also clarify whether or not imbibition is actually taking place and at what time scale. Experiments have been performed at atmospheric conditions using the Theta Lite Optical Tensiometer shown in Figure B.3 and for which the schematic had been shown in Figure 4.7. The substrate is made of hydrophilic polyethersulfone. Fresh pieces are used in every subsequent test. The Theta Lite Optical Tensiometer has a resolution of $f = 10$ Hz and measures the left and right contact angles with the solid substrate over time as well as the average value for the contact angle. The latter has been collected in Table C.1 in Appendix C.3 Furthermore, volumetric measurements have been done to account for variable droplet sizes. Subsequently, these are compared to a capillary length scale which gives insight into when gravity effects can be disregarded.

6M KOH

This section highlights experiments in which a 6M KOH solution has been used. Six separate 6M KOH samples were analysed at atmospheric conditions and room temperature. The samples are presented in Figure 5.7. Shown here are six droplets. Since the Theta Lite Optical Tensiometer still requires a manual hand in separating the droplet from the syringe, the droplets vary in volume and size. Droplet volumes between $1.0 \leq V_{\text{sample}} \leq 8.5$ µl were recorded.

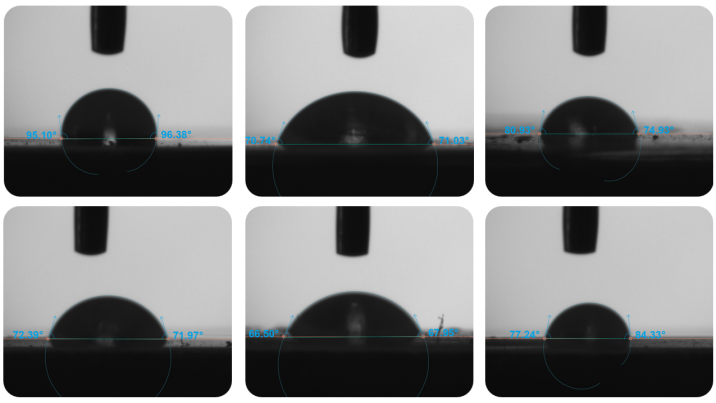

Figure 5.7: Six separate 6M KOH samples were analysed. The substrate is made of hydrophilic polyethersulfone. Fresh pieces are used in every subsequent test. Experiments have been performed at atmospheric conditions using the Theta Lite Optical Tensiometer.

Figure 5.8 shows the average contact angle measurements over time for the six separate drops. An average contact angle of $\bar{\theta}_{\text{6M}} = 78.14°$ was found.

Volume versus time

Figure 5.9 shows the trend associated with the droplet volume and shows evident decrease over time for sample 5. Wetting the membrane results in a flattening of the droplet, i.e. the contact angle should go down. This can be confirmed from Figure 5.8. The remaining graphs show fairly constant volume over time. Droplet 2 shows an increasing trend. However, these measurements are widely distributed and are less reliable to draw conclusions from when linearly fitting.

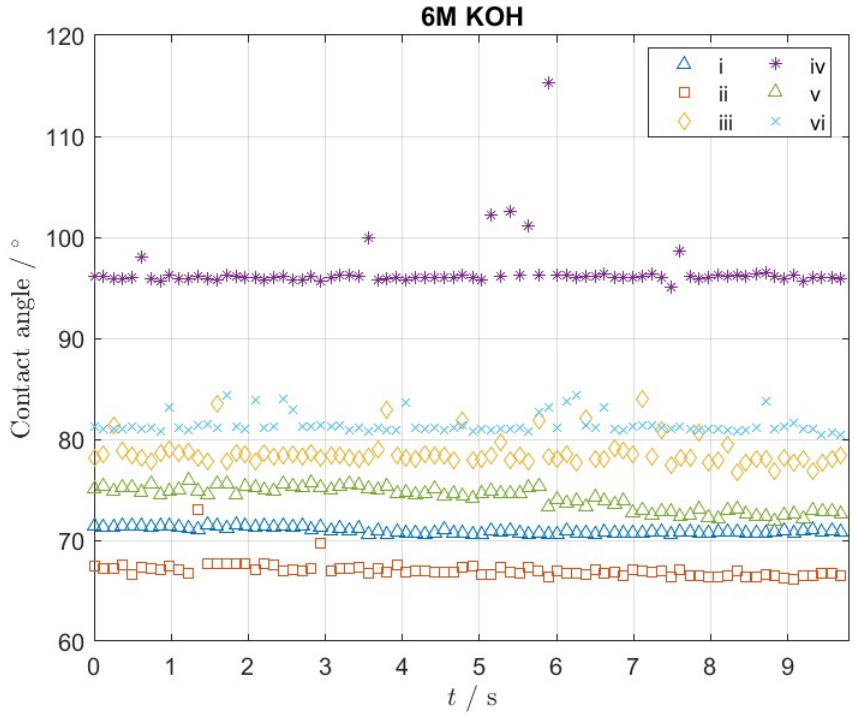

Figure 5.8: Contact angle measurements from 6M KOH droplet samples i,...,vi. Plotted against time.

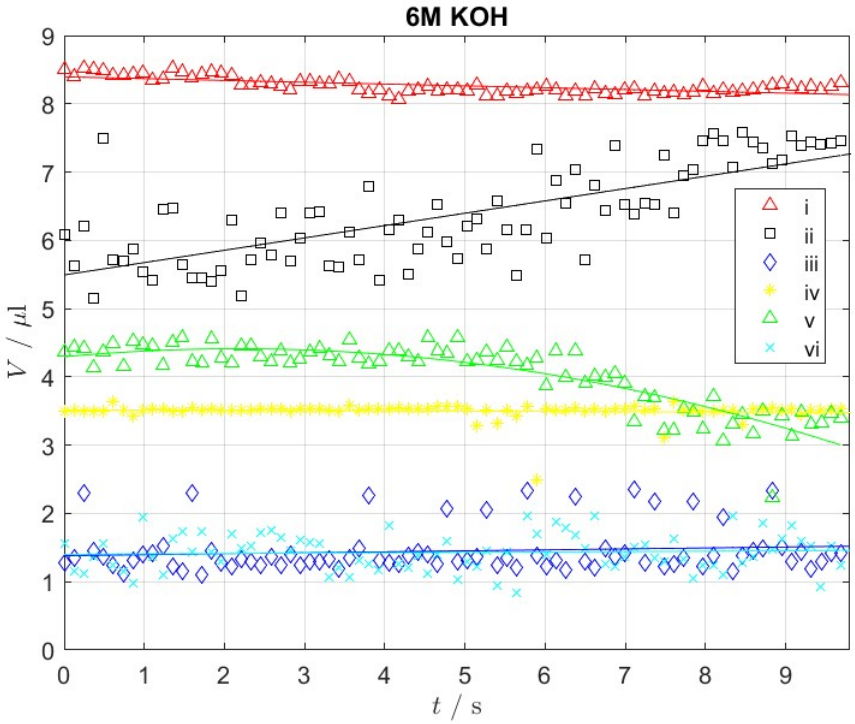

Figure 5.9: Left: Volume versus time of the six droplet samples i, . . . ,vi of 6M KOH solution. Right: Fitted profiles to the measurements.

Volume versus droplet radius

To verify whether gravity has an influence on the presented results, we can determine the capillary length that accompanies the electrolytic solution. Note that we deal with dynamic droplets when we consider large time scales, e.g. due to imbibition. For 6M KOH a capillary length of $r = 2.84$ mm was determined based on a surface tension of approximately $\gamma_{6M} = 97.6 \cdot 10^{-3}$ kgs^{-2} and density of $\rho_{6M} = 1236$ kgm^{-3}. These are rough estimates retrieved from [4] and experimental work by Dunlap et al. [22]. Figure 5.10 shows the volume versus radius and shows that for the six samples shown in Figure 5.7, all radii are well below the capillary length. Indicating that gravity effects are of minor influence.

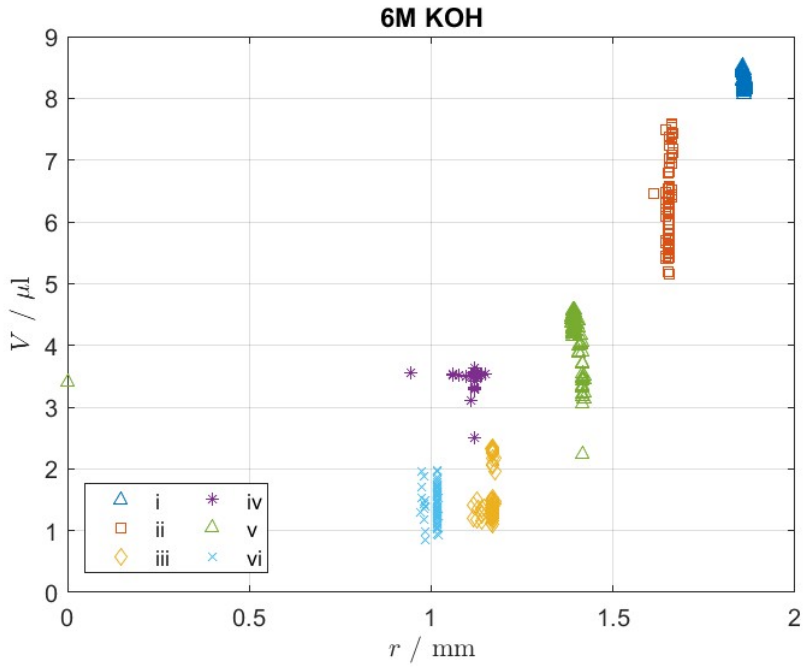

Figure 5.10: Volume versus radius of the six droplet samples i, . . . ,vi of 6M KOH solution.

6M KOH (fluorescein)

Experiments have been performed where a 6M KOH solution has been used in which fluorscein salt has been added. During testing for leak tightness the fluorescein salt serves as a tracer. However, the impact this addition has on capillary imbibition is not yet well understood. Six separate samples were analysed at atmospheric conditions and room temperature. Droplet volumes between $2.5 \leq V_{\text{sample}} \leq 5.0$ μl were recorded. The samples are presented in Figure 5.11. For all samples a clear decreasing trend can be observed over time. This decrease can be attributed to capillary imbibition taking place at the solid-liquid interface, i.e. some of the liquid makes its way into the membrane over time. Analysing the samples over time, for which results are displayed in Figure 5.12, it shows that the average contact angle measurements for all samples drops. Over the displayed time interval an average contact angle of $\bar{\theta}_{6M(\text{Fluor})} = 77.54°$ was found.

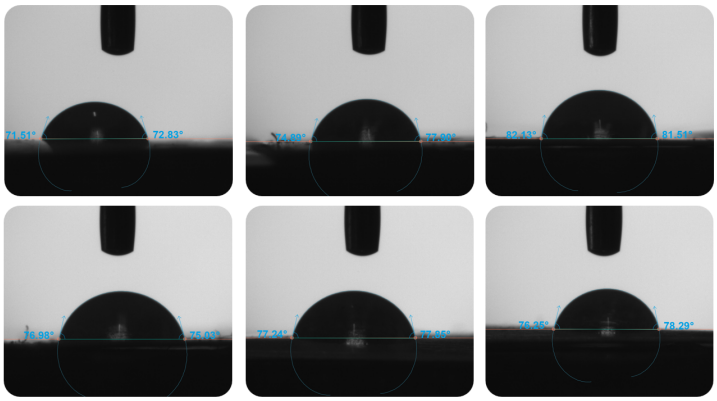

Figure 5.11: Six separate 6M KOH samples were analysed in which fluorescein salt has been added (to pose as a tracer). The substrate is made of hydrophilic polyethersulfone. Fresh pieces are used in every subsequent test. Experiments have been performed at atmospheric conditions using the Theta Lite Optical Tensiometer.

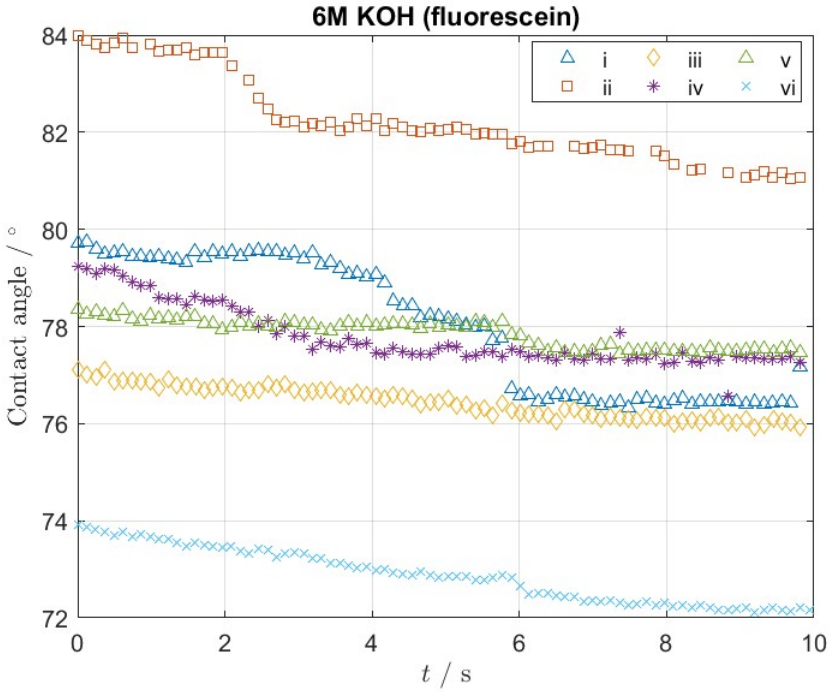

Figure 5.12: Contact angle measurements from droplet samples i,. . . ,vi. Plotted against time.

Volume versus time

Analysing the volume associated with the samples versus time, shown in Figure 5.13, it shows a decreasing trend for 4/6 samples, which would mean the difference in volume over the measuring time is presumably imbibed into the membrane.

Volume versus droplet radius

Assuming a capillary length roughly equal to the 6M KOH case we see from Figure 5.14 that the volume versus radius for these six samples are all below the capillary length.

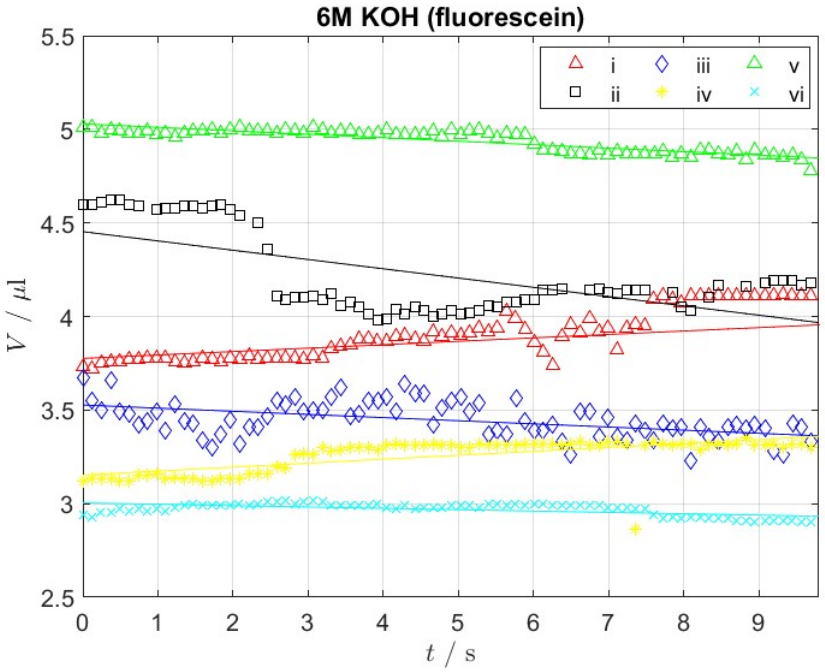

Figure 5.13: Left: Volume versus time of the six droplet samples i, . . . ,vi of 6M KOH + fluorescein solution. Right: Fitted profiles to the measurements.

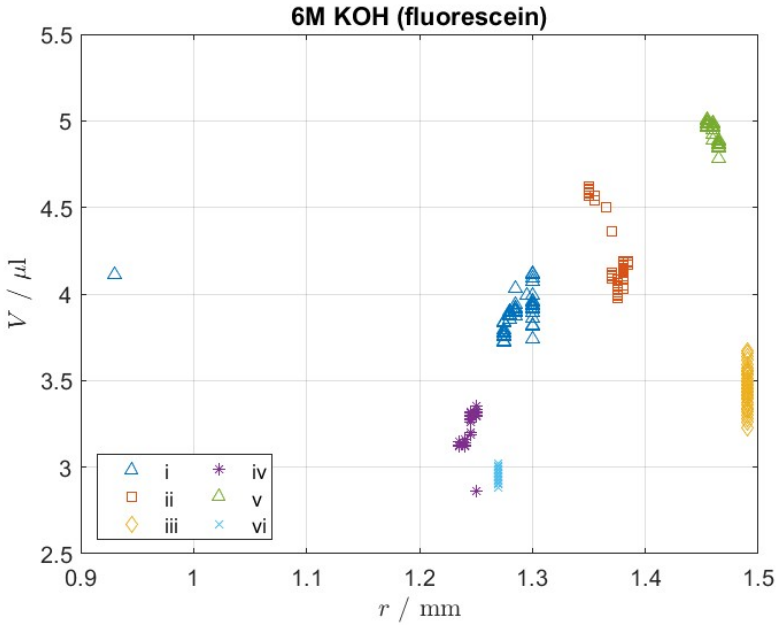

Figure 5.14: Volume over radius of the tested droplets of 6M KOH solution with added fluorescein tracer salt.

5M KOH

5M KOH solution has been used in this subsequent experiment. Similarly to the above two cases six separate 5M KOH samples were analysed at atmospheric conditions and room temperature. Droplet volumes between $1.8 \leq V_{\text{sample}} \leq 10.3$ µl were recorded. The samples are presented in Figure 5.15. Figure 5.16 shows the average contact angle measurements over time for the six separate drops. Over the displayed time interval an average contact angle of $\bar{\theta}_{\text{5M}} = 73.90°$ was found.

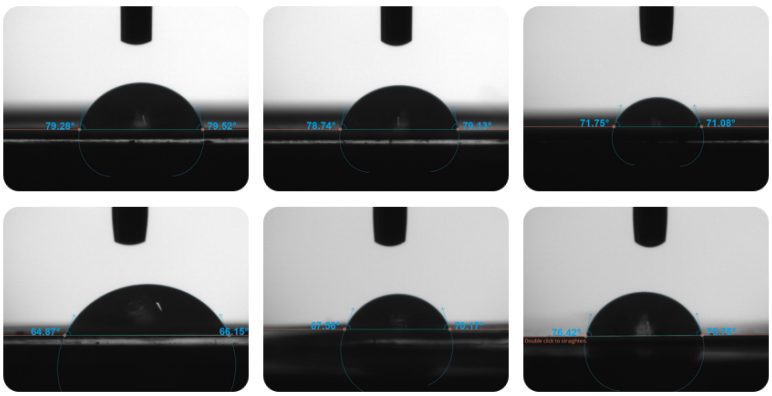

Figure 5.15: Six separate 5M KOH samples were analysed. The substrate is made of hydrophilic polyethersulfone. Fresh pieces are used in every subsequent test. Experiments have been performed at atmospheric conditions using the Theta Lite Optical Tensiometer.

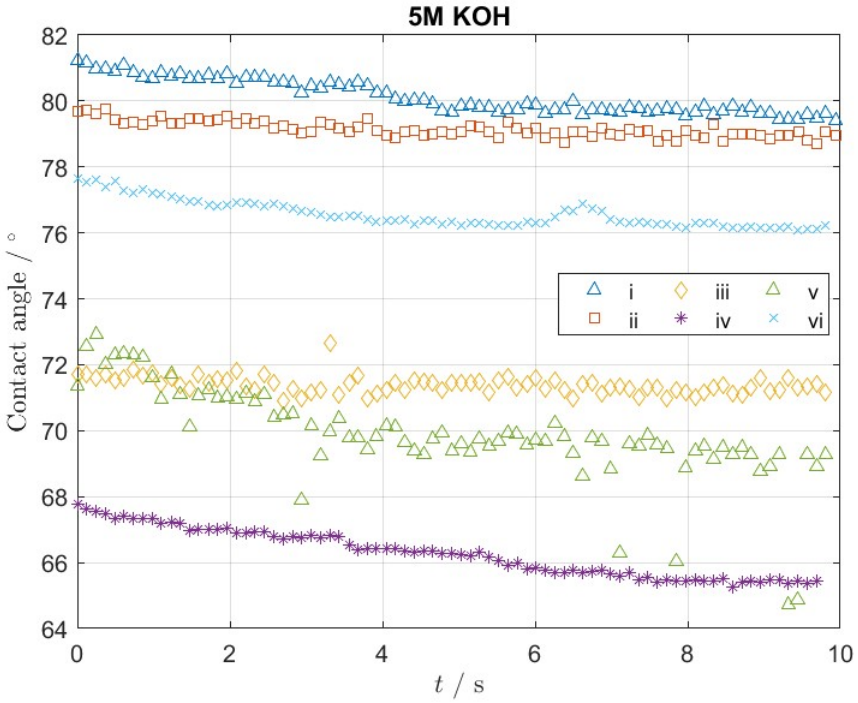

Figure 5.16: Contact angle measurements from droplet samples i,. . . ,vi. Plotted against time.

Volume versus time

Figure 5.17 shows the trend associated with the volume of the samples and results in fairly constant volume recorded over time. However, it can be seen that there are decreasing trends in contact angle over time and these are not seen in the volume measurements. Hypothetically, it could be that the measuring resolution of the Theta Lite Optical Tensiometer is a limiting factor, which is no larger than 10 hz. Alternatively, an imprecise determination of the border between the substrate and droplet could be a source for this deviating phenomena.

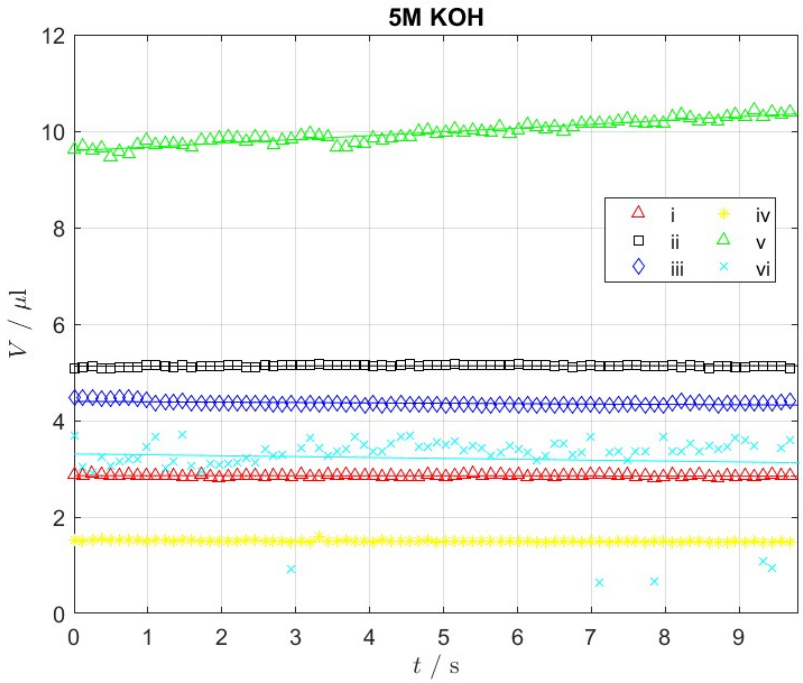

Figure 5.17: Left: Volume versus time of the six droplet samples i, . . . ,vi of 5M KOH solution. Right: Fitted profiles to the measurements.

Volume versus droplet radius

To verify whether gravity has an influence here, we can again determine the capillary length that accompanies the electrolytic solution. For 5M KOH a capillary length of $r = 2.71$ mm was determined based on a surface tension of approximately $\gamma_{5M} = 86.4 \cdot 10^{-3}$ kgs^{-2} and density of $\rho_{5M} = 1203$ kgm^{-3}. Figure 5.18 shows the volume over radius and shows that for the six samples in question, all radii are again well below the capillary length. From these experiments, the gravity effects can be seen not to be of dominant influence.

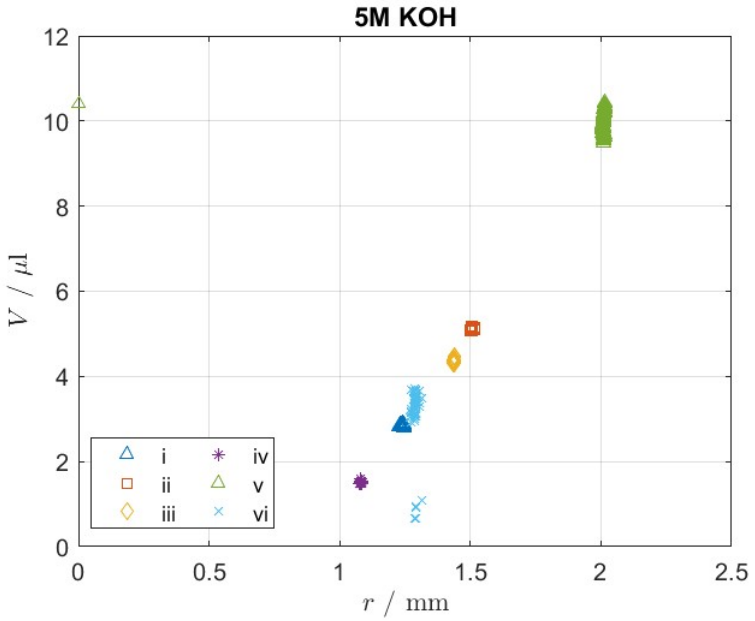

Figure 5.18: Volume versus radius of the six droplet samples i, . . . ,vi of 5M KOH solution.

5.4. Constant current experiments

This section will present the experimental results regarding the constant current experiments. Experiments have been performed with the small cell and bottom-up and top-down experiments have been performed with the segmented cell. These will be discussed below.

5.4.1. Small capillary-fed electrolyzer

The electrolyzer previously shown on Figure 4.3 was used to conduct a constant current experiment. Figure 5.19 shows the realised setup and two additional thermal snapshots of the cathode side during the experiment. These were taken with approximately 1.5 hours in between. It can be seen from the top right picture that drops of KOH solutions are deposited on the metal frame, eventually being captured by the camera in the infrared spectrum. Furthermore, towards $t = 11000$ seconds, KOH deposits can be observed around the square cutout with temperatures reaching close to $T = 83\ ^{\circ}\text{C}$. These deposits are due to gas bubbles that nucleate at the submerged part of the membrane and PMMA material. Bubbles escaping this region shoot upwards and splash onto the metal frame. The electrolyte is a 6M KOH solution. The cell is powered by a Delta Elektronika SM 45-140 power supply.

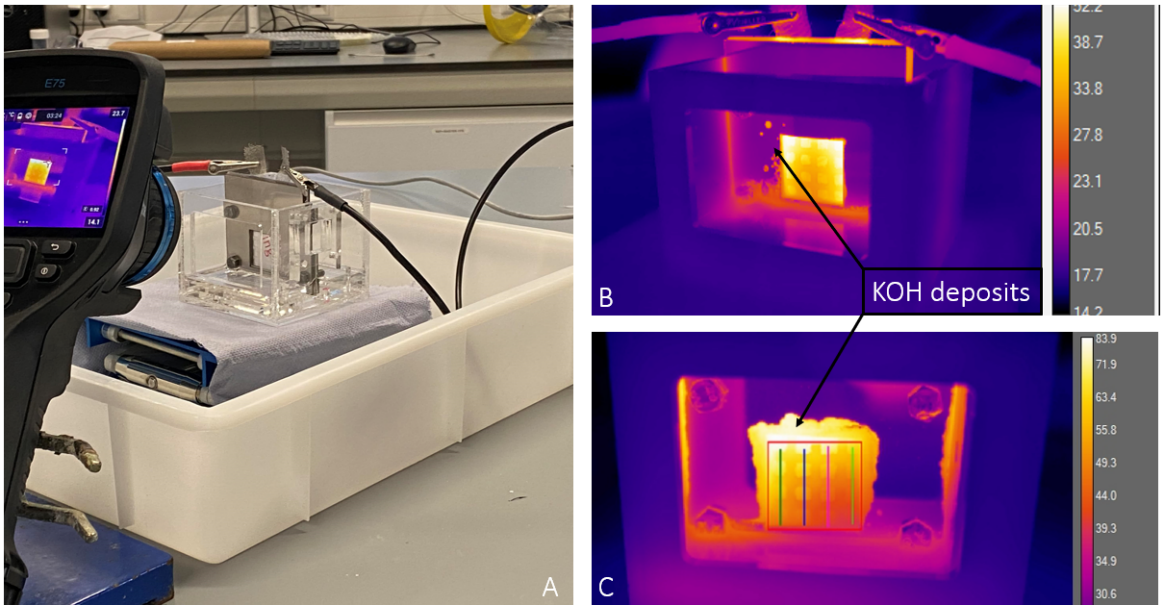

Figure 5.19: Shown are in A): The small cell with a thermal infrared camera focused on the cathode side. B) The infrared image take at $t \approx 6000$ s, C) Infrared image taken at $t \approx 11000$ s. Indicated vertical lines represent: Far Left, Mid Left, Mid Right and Far Right, respectively.

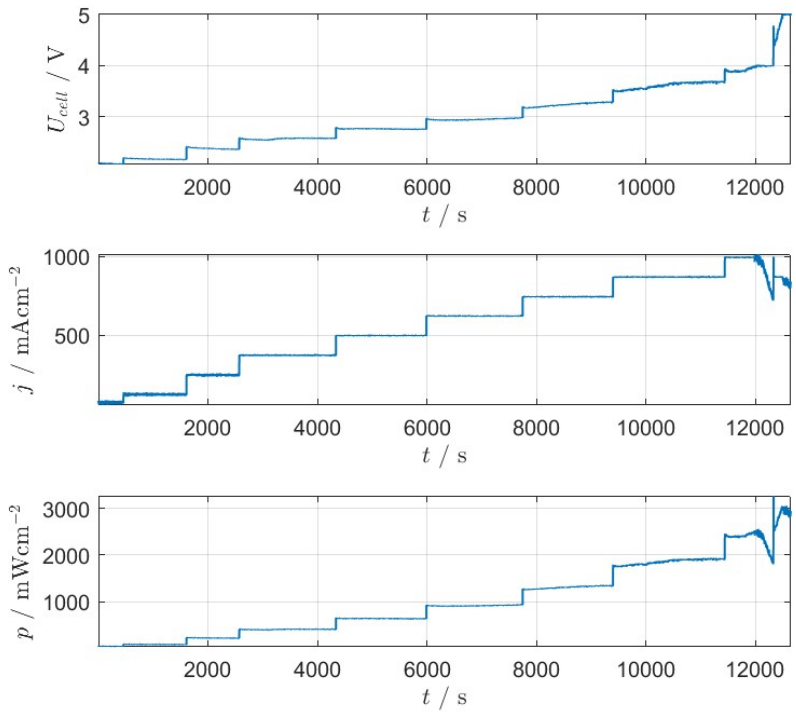

Figure 5.20: Experimental results for the constant current experiment performed with a 6M KOH solution as the electrolyte. Plots show voltage current- and power density versus time, respectively.

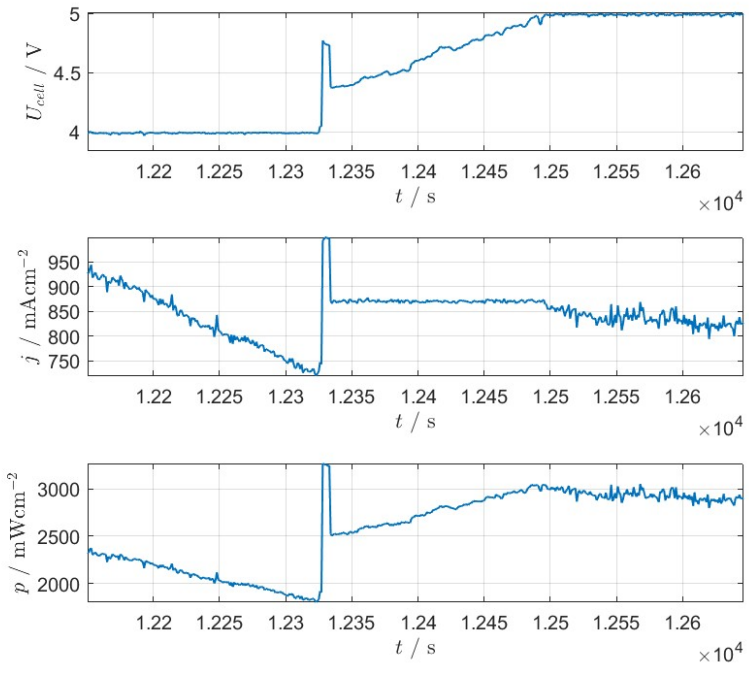

Figure 5.21: Zoomed-in plot of Figure 5.20 for $t \geq 12000$ s. The last increase in current density can be seen to lead to large nonlinear behaviour in voltage, current and power density.

Figure 5.20 presents the voltage, current- and power density graphs that have resulted from the experiment. Starting from approximately $j = 80$ mAcm^{-2} the current was increased predominately in steps of $j = 125$ mAcm^{-2} towards a current density of approximately $j = 1000$ mAcm^{-2}. Power density P has been calculated by subtracting the thermo-neutral potential $U_{\text{TN}} = 1.48$ V from the measured potential U as shown in Equation 5.6.

$$P = (U - U_{\text{TN}}) \cdot j \tag{5.5}$$
$$= (U - 1.48) \cdot j \tag{5.6}$$

The graphs show that an increase in current is generally followed by a finite temperature and voltage increase. However, applying currents close to $I = 4$ A - or $j = 1000$ mAcm^{-2} - shows highly nonlinear behaviour. A zoom is provided in Figure 5.21. This high applied current results in what is presumably primarily resistive heating of the cell components with damage to the cell architecture as a consequence. The resistive heating can be attributed to precipitation due to absence of flux of fresh electrolyte. Figure 5.22 shows the state of the MEA after disassembly. It shows that the observed nonlinear graphs are due to failure of cell components. Dark precipitation can be seen which presumably has heated up, burning through the polyethersulfone diaphragms and nickel-mesh electrode. Short-circuiting was probably prevented as the precipitate provided a barrier between the electrodes, preventing these from touching each other.

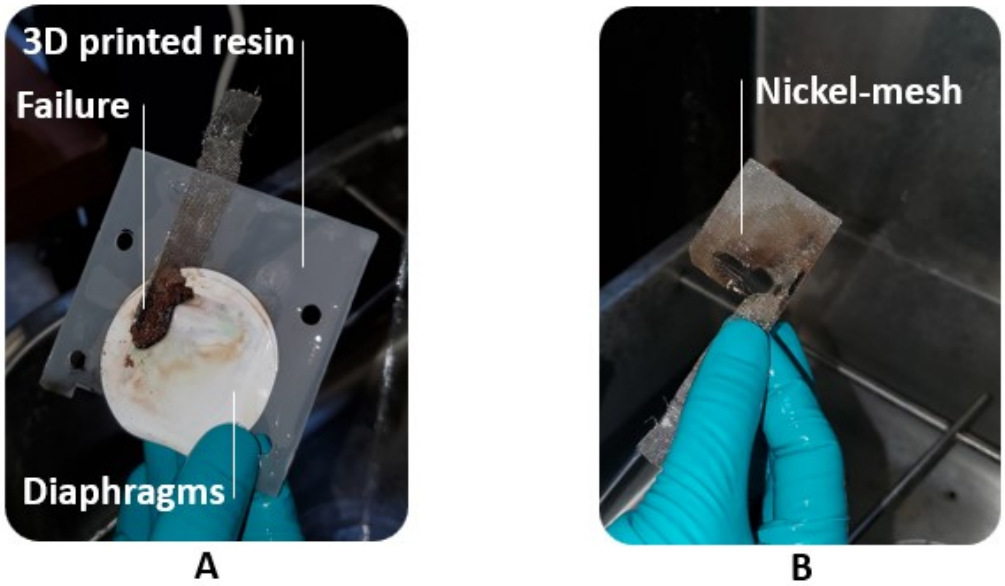

Figure 5.22: A: Illustration of polyethersulfone diaphragms, 3D printed resin and nickel-mesh cathode. The top left shows the burnt region. B) View of the nickel-mesh cathode showing the damage to the material.

Temperature

Figure 5.23 presents the temperature graphs that have resulted from the experiment. A narrow valley can be seen in the $T-t$ plots at $t = 11000$ seconds. This is due to battery replacement of the IR camera after which some finite time was needed for the camera to re-calibrate. For all temperature graphs shown random fluctuations can be seen towards the end of the experiment. The temperatures inside the square cutout reached close to $T = 120°$C within a relatively narrow time window of approximately 500 seconds. This rapid heating originating from the ”Far Left” measurements corresponds to the top left damage that is observed in Figure 5.22.

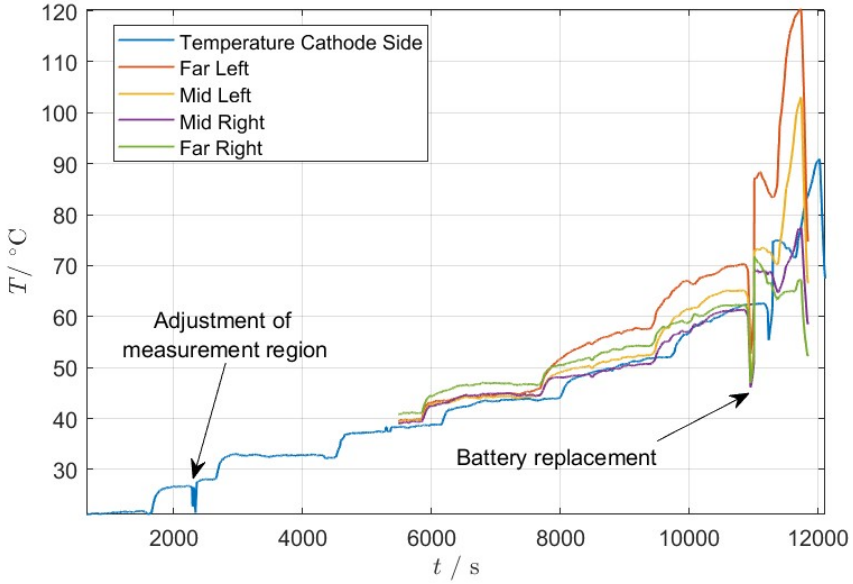

Figure 5.23: Temperature results for the constant current experiment performed with the small electrolyzer. Plots show temperatures for Far Left, Mid Left, Mid Right and Far Right regions of the cathode (analogous to the vertical lines shown in Figure 5.20-C). Additionally, the temperature of the square cut out has been recorded.

Power density - temperature characteristic

Figure 5.24 shows the associated power density versus temperature difference graph. A linear fit has been provided. The temperature difference is determine by subtracting the room temperature from the maximum obtained temperature at every current density. The ratio of power density and temperature difference divided by 2 results in the heat transfer coefficient for the cathode side which equates to $h = 121.04$ W/m^{2}K. However, this gives an overall heat transfer coefficient and does not indicate the contribution of convective, radiative and conductive components of the heat transfer coefficient.

To get an estimate of the convective heat transfer coefficient we can use Equations 2.31 and 2.34 provided by Mills [37] and Van Vliet et al. [51]. Figure 5.25 shows that the estimated convective heat transfer coefficient is very low at no larger than $h_c = 7.67$ W/m^{2}K. This indicates that the majority of the heat produced is dissipated through either conduction or radiation.

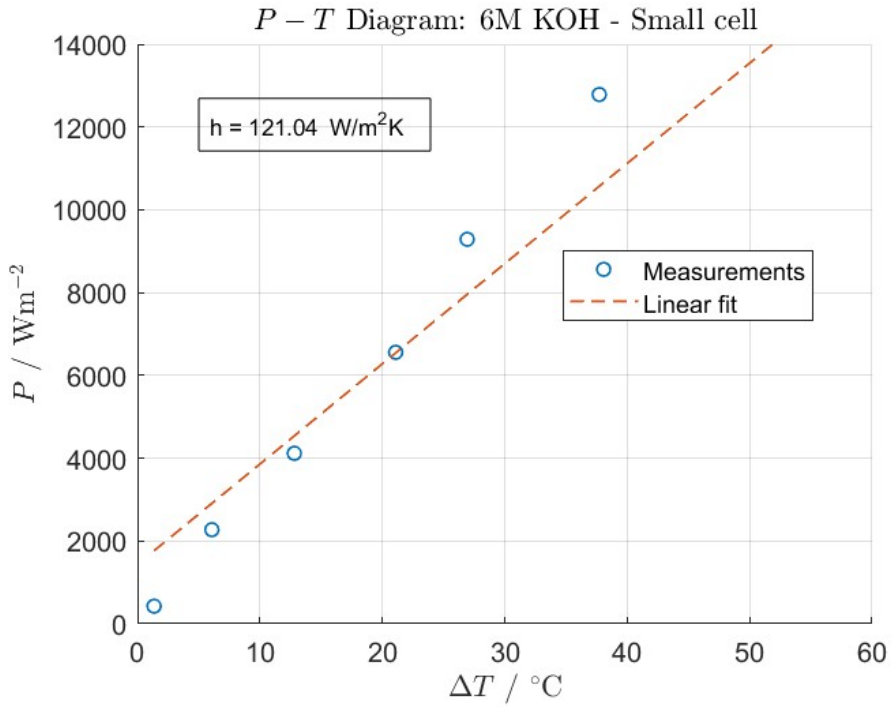

Figure 5.24: Power density versus temperature for the small cell. Measurements are linearly fitted. The accompanied heat transfer coefficient derived from the slope of the fits has also been shown.

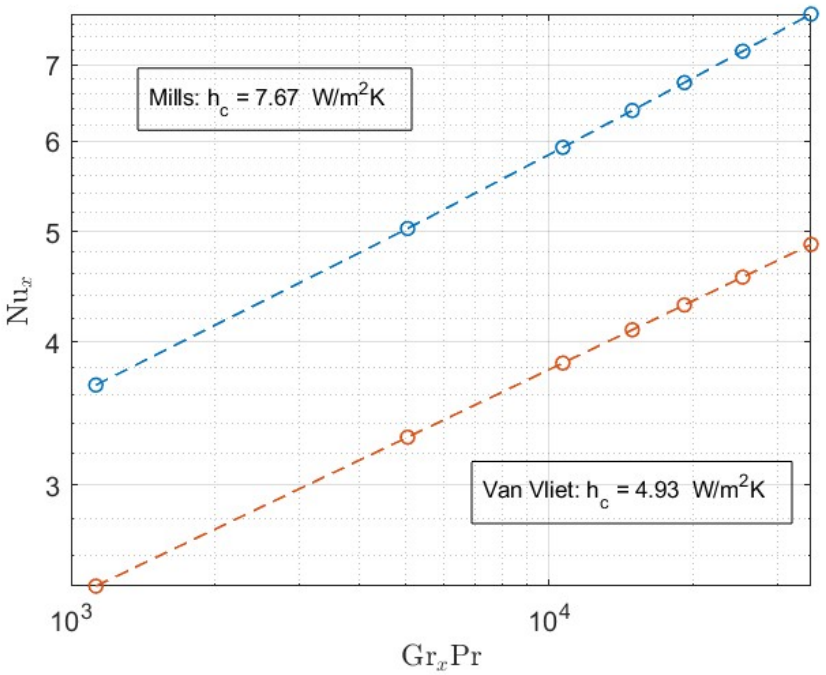

Figure 5.25: Local Nusselt number versus local Raleigh number. The latter consists of the local Grashof number and Prandtl number.

5.4.2. Constant Current Bottom-Up Experiment

The experiment utilising the small cell was conducted using a 6M KOH solution as the electrolyte. Initially, for the segmented cell, the same electrolyte was meant to be used. However, as previously presented, 6M KOH behaves differently on the hydrophilic membrane of choice in this thesis. Therefore, the choice was made to perform experiments utilising the segmented cell, starting from lower concentrations of KOH and gradually build up if capillary wicking was observed. Tests include the use of fluorescein salt as tracer which can be seen in Appendix B.4. Below, the single segment experiment was performed at constant current, focusing on bottom-up flow from the lower electrolyte reservoir. Afterwards, the top-down two segment and four segment experiments will be highlighted.

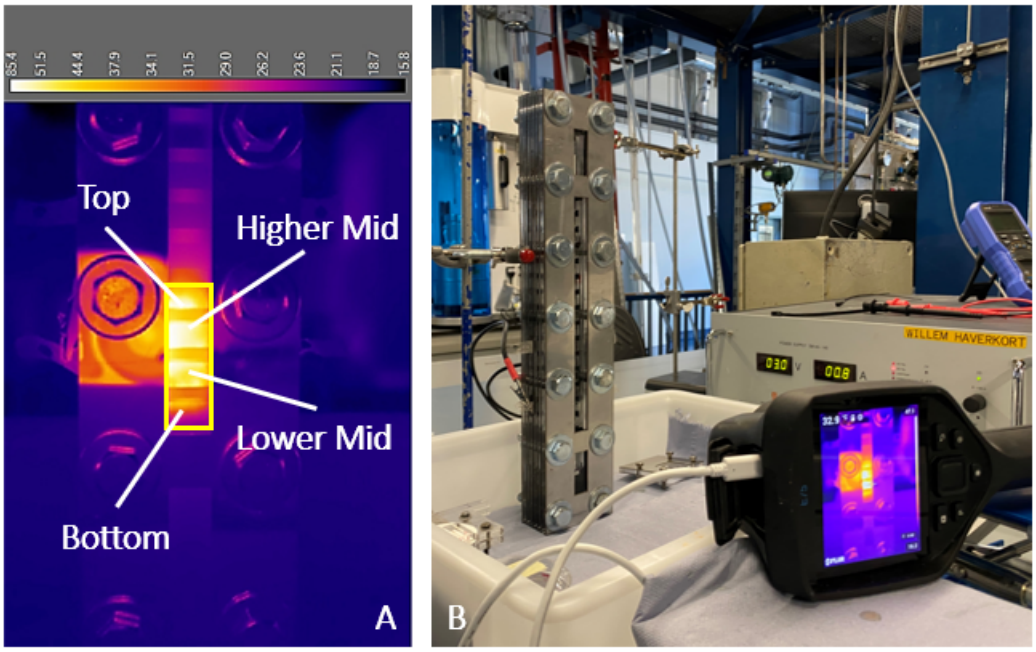

Figure 5.26: Shown are in A): The segmented cell with a thermal infrared camera focused on the lower segment on the cathode side. Point ROIs along the length of the segment are represented with labels ”Top”, ”Higher Mid”, ”Lower Mid” and ”Bottom”.. The yellow box takes the whole exposed electrode as a region of interest. B) The experimental setup with camera, power supply and cell in view.

Single segment experiment

The segmented cell was used to conduct a constant current experiment utilising a single segment. The lowest segment was used and a temperature analysis of the exposed segment was made. Figure 5.26 shows the experimental setup. A Delta Elektronika SM 45-140 power supply has been used to power the cell. A FLIR E75 camera performed thermometry via FLIR ResearchIR software. The electrolyte is a 2M KOH solution. A volume of $V = 6$ ml has been injected into the bottom electrolyte reservoir and half of the membrane was allowed to saturate. This took approximately 34 minutes after which power was supplied to the segment. Figure 5.27 presents the results from the experiment. Considering the segment in use has a surface area of $A_{\text{electrode}} = 12.5$ cm^2 the measured potential seems to be very high for this low current density. The presented overpotential more than doubles the thermo-neutral potential.

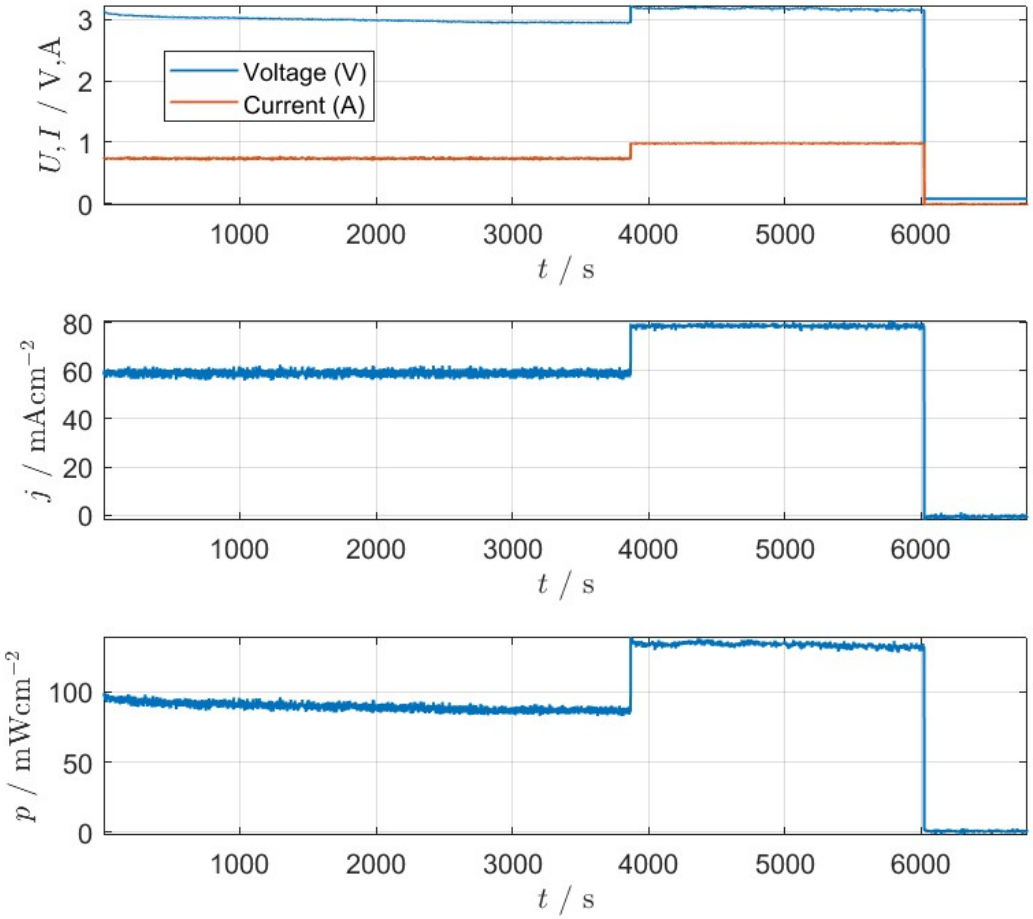

Figure 5.27: Plots show voltage, current density and power density versus time, respectively. Experiment has been performed at constant current with the bottom most segment with bottom-up feed of 2M KOH electrolyte.

Temperature

Figure 5.28 presents temperature measurements done for the whole segment and the point ROIs. During electrolysis the top and bottom region stay the coolest. For the bottom region this is where fresh electrolyte is introduced to the nickel mesh electrodes first. However, a clear distinction can be seen from the middle two regions of interest. Electrons travelling towards the electrodes naturally take the path with lowest resistance. Hence, the center of the electrode can be seen to reach the highest temperatures.

Heat transfer coefficient

Due to the limited power density range, the heat transfer coefficient was estimated for the separate power densities shown in Figure 5.27 as

$$h = \frac{P}{2\Delta T} \tag{5.7}$$

With h the heat transfer coefficient, P the power density that goes into heating (using Equation 5.6) and ΔT the difference in the maximum measured temperature and atmospheric temperature. Taking the average results in a heat transfer coefficient of

$$h = 19.13 \text{ W/m}^2\text{K} \tag{5.8}$$

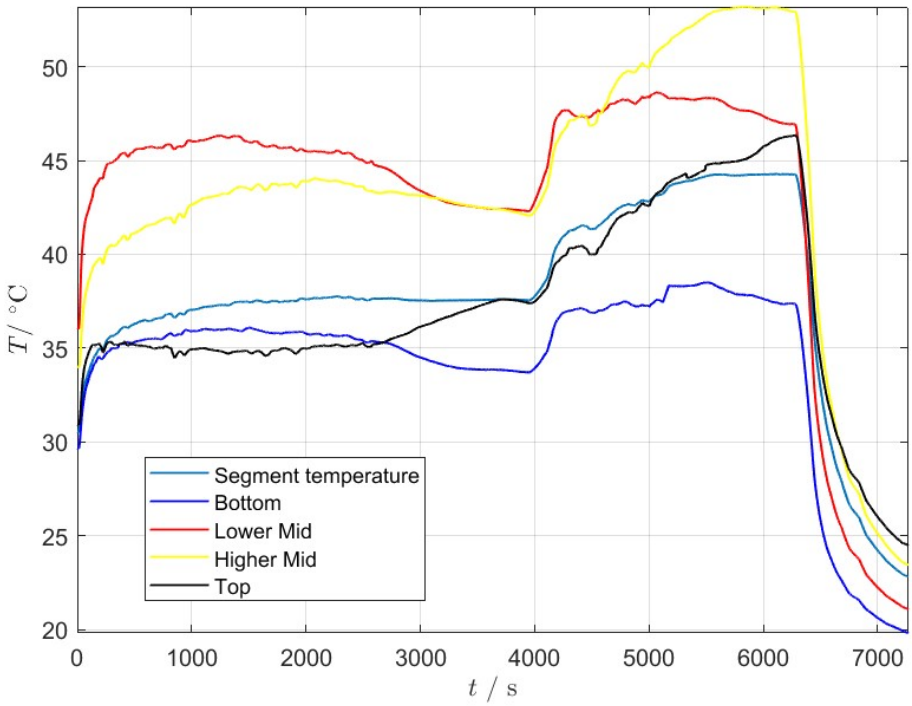

Figure 5.28: Shown are the temperature measurements for the segment and point ROIs along the length of the segment. The cool down profile starting at approximately $t = 6200$ s has also been shown.

From observation, precipitation was noticed on the electrode surface at $t \approx 6000$ s at the top point of the bottom segment. This is shown in Figure 5.29. To prevent the risk of damage to the electrodes and diaphragm the experiment was stopped at this time.

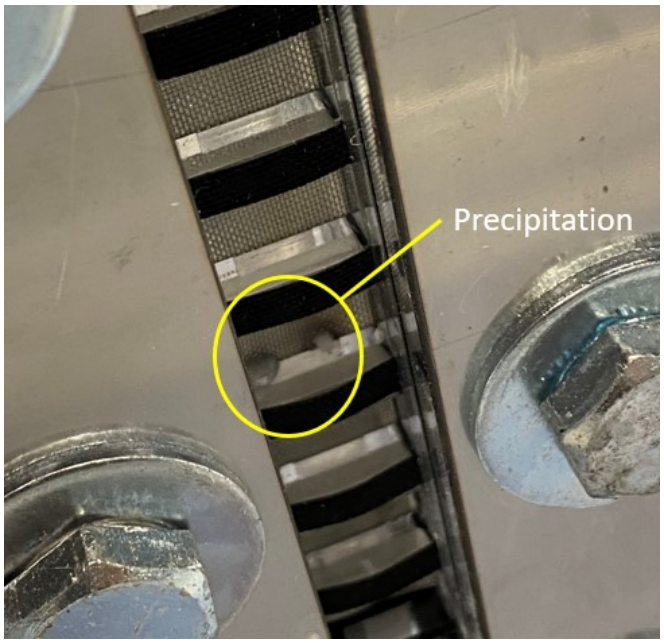

Figure 5.29: Shown is the lower part of the segmented cell. Indicated are precipitation and local discolouring of the nickel-mesh electrode at the top of the lowest segment.

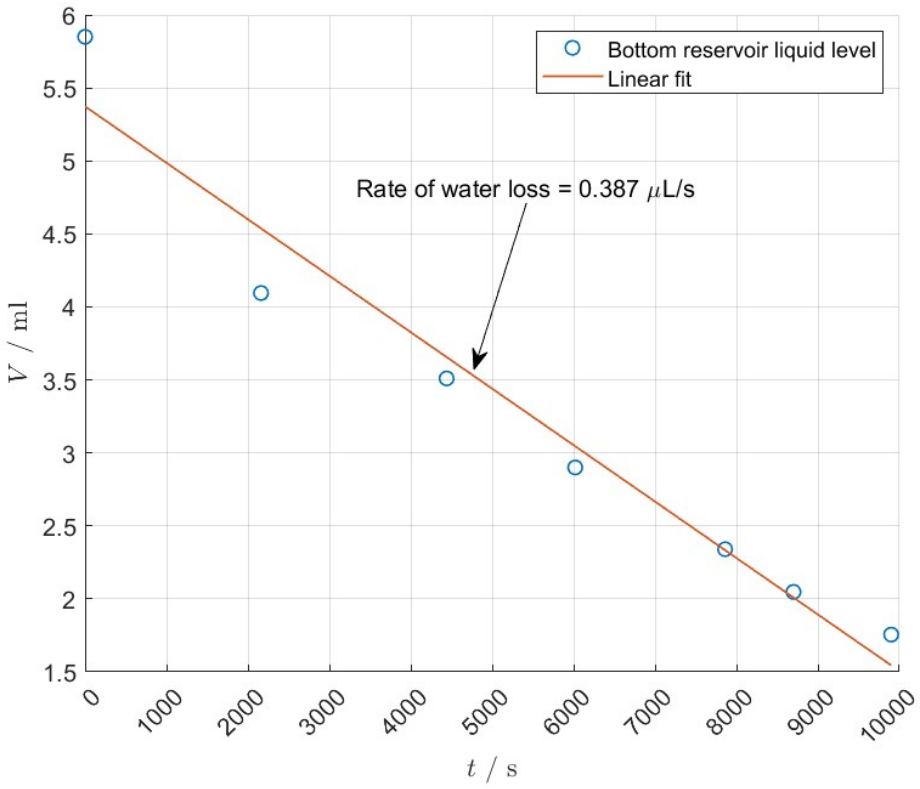

Figure 5.30: Measurements of the bottom reservoir liquid level versus time. The duration exceeds 6000 seconds as the water level was recorded also during cool-down. An initial 6 ml of 2M KOH solution was injected. Linear fitting the data points resulted in a rate of water loss equal to 0.387 μL/s.

Electrolyte consumption

The rate of water consumption by the cell has also been recorded. Figure 5.30 shows the measurements together with a linear fit from which the rate of water loss was derived. A total volume of 3.87 ml was utilised during the experiment. We can make an estimate of the volume of water that has evaporated. To do this we can use Faraday's law of electrolysis to relate the volume of water consumed, Q_{w}, to the volume we measure.

$$Q_{\mathrm{w}} = \frac{ItV_m}{4F} \tag{5.9}$$

With I the current, t the duration of the applied current, V_m the volume of a mole of water and F Faraday's constant. Figure 5.31 shows the resulting water consumption versus applied current. The total calculated water consumption equates to 0.23 ml. Subtracting this from the initial 3.87 ml that was utilised during the experiment results in 3.64 ml of evaporated volume.

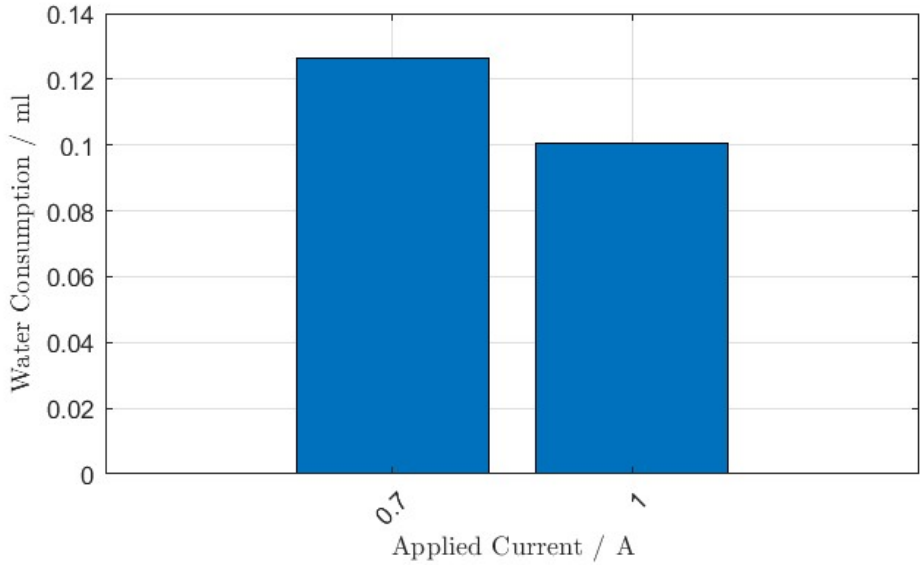

Figure 5.31: Total water consumption at the two applied currents. Standard conditions for water have been assumed here to gain an estimate for the consumed volume. Segment area is $A = 12.5$ cm^2.

Enthalpy of vaporization

We can also utilise the rate of water consumption to get an estimate for the heat transfer coefficient. We can use the enthalpy of vaporization and specific heat capacity of water to equate:

$$\dot{m} = 0.364 \cdot 10^{-6} \text{ kg/s} \tag{5.10}$$

$$\Delta \dot{H}_{\text{evap}} = 2260 \cdot 10^{3} \text{ J/kg} \tag{5.11}$$

$$c_p = 4180 \text{ J/kgK} \tag{5.12}$$

$$\Delta T \approx 33.2 \text{ K} \tag{5.13}$$

$$h = \frac{\dot{m}\left(\Delta H_{\text{evap}} + c_p \Delta T\right)}{2A\Delta T} \approx 10.34 \text{ W/m}^2\text{K} \tag{5.14}$$

With $\dot{m}$ the evaporation rate in kg/s, c_p the specific heat capacity in J/kgK and ΔH_{evap} the enthalpy of vaporization of water in J/kg. The temperature difference has been taken as the difference between the maximum measured temperature and the standard temperature at atmospheric conditions. This approach shows a 40% deviation compared to the heat transfer coefficient derived from the experimental measurement. Since the heat transfer coefficient contains the conduction, radiation and convective contributions it is likely that additional heat losses in the actual experimental setup are not fully accounted for. Similar to the procedure described in section 5.4.1 we can estimate the convective heat transfer coefficient from the emperical relations given by Mills and Van Vliet, which result in

$$h_c \approx 6.75 \text{ W/m}^2\text{K (Mills)}$$

$$h_c \approx 3.92 \text{ W/m}^2\text{K (Van Vliet)}$$

Capillarity and bottom-up feed

During the experiment precipitation was observed. Furthermore, the highest temperatures are measured in the top and higher-mid section. This shows that capillary action alone is not able to provide a feed much higher up in this cell. At these low current densities and conductivity, the volume of liquid could have evaporated away before reaching the top most part of the segment. As a consequence leading to resistive heating due to drying of the electrode. Since the measured temperature increase was already exceeding $T = 50°$C, the focus had been shifted to a top-down approach while keeping the same design for the cell.

5.5. Constant current top-down experiment

The top-down feed of electrolyte was studied in the segmented cell. A finite volume of electrolyte is injected in the top reservoir and allowed to be imbibed by the diaphragm under influence of gravity. A typical batch process could be distinguished here, i.e. subsequent injections of electrolyte have been supplied to the cell and allowed to react before each next injection (recall Figure 4.5 on dilution). All experiments have been conducted at constant current using either 1, 2 or 4 segments. Power supplies used are a Delta Elektronika SM 45-140 and the OWON SPE6103. A FLIR E75 camera is used for thermometry.

5.5.1. Single segment Constant Current Top-Down Experiment

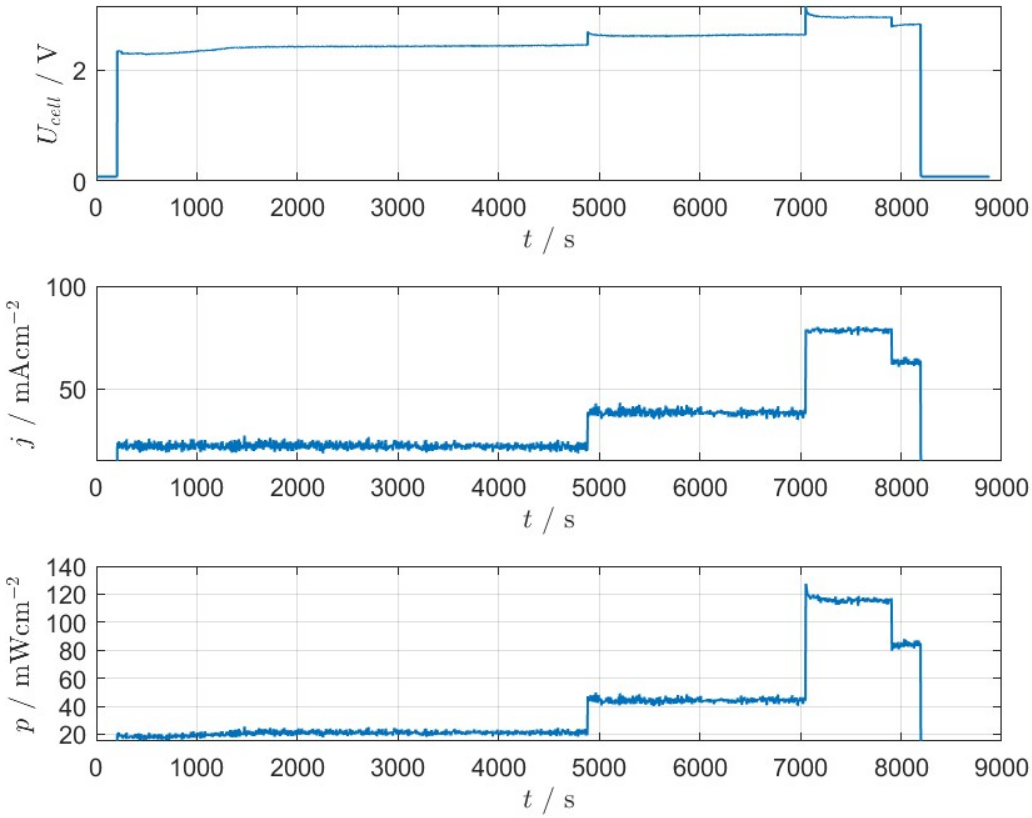

Figure 5.32: Results for 3M KOH single segment top-down experiment performed on constant current. The top most segment has been used. Plots show voltage, current density and power density versus time, respectively.

Figure 5.32 shows the results from experiments utilising a top-down feed on a single segment. The electrolyte is a 3M KOH solution. The membrane has been wetted for approximately 20 minutes.

Temperature

Four points along the vertical length of the segment are utilised to record the temperature. These are labelled as $1/4, \ldots, 4/4$. Also the segment as a whole has been recorded. Figure 5.33 shows temperature versus time for the segment. Similarly to the bottom-up experiment the center of the electrodes experiences the highest temperature increase. This is in part due to the smaller distance and lower resistance on electron paths from the flaps towards the center of the vertical strip. However, the influence of capillary wicking becomes more significant when we compare the 4 points of interest. Segment 1 - 1/4 shows a far lower temperature at all times which is presumably due to fresh electrolyte that not only promotes electrolysis but also actively cools the segment.

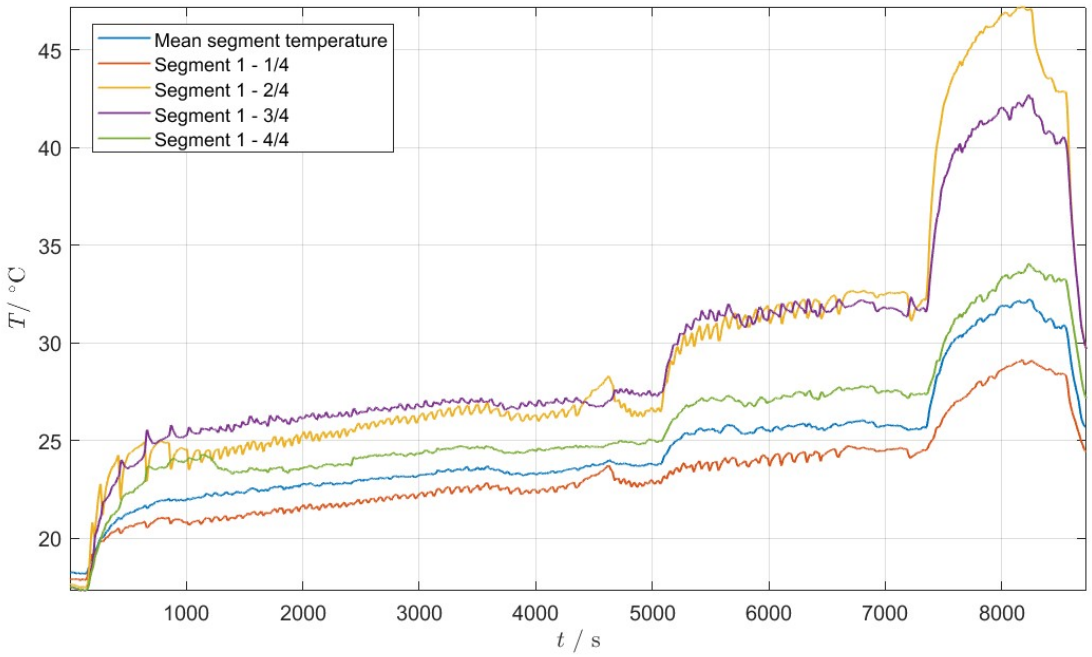

Figure 5.33: Temperature results for 3M KOH single segment top-down experiment performed on constant current. The top most segment has been used. Plot shows segment temperature and height-specific temperature versus time, respectively.

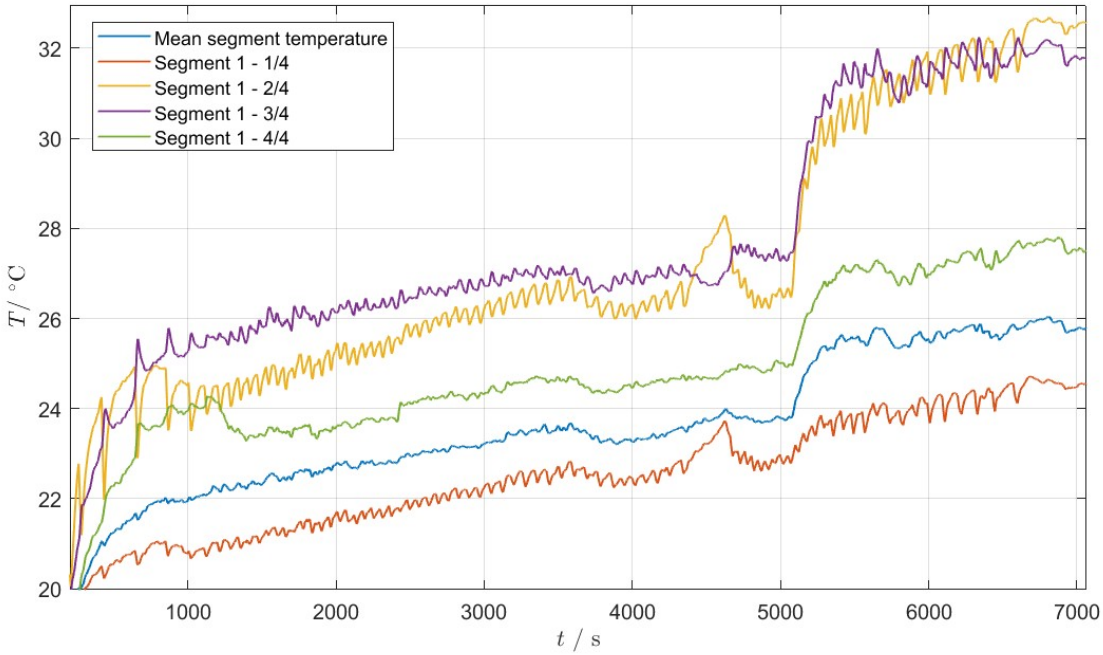

Figure 5.34: Zoom of Figure 5.33. Plot of temperature versus time to highlight oscillatory behaviour in the graphs.

Temperature oscillations

Figure 5.34 shows a zoomed in view of the temperature profiles. The temperature plots show a dynamic temperature oscillation over time. From the plot we can see roughly 10-15 oscillations per 1000 second window, i.e. a frequency of 0.01-0.05 Hz. The study by Leijn et al. [41] also shows oscillatory

temperature trends. This can be seen from Figure 5.35 and even shows out of phase graphs for the bottom region of the capillary-fed cell. The origin of those fluctuations is still unknown.

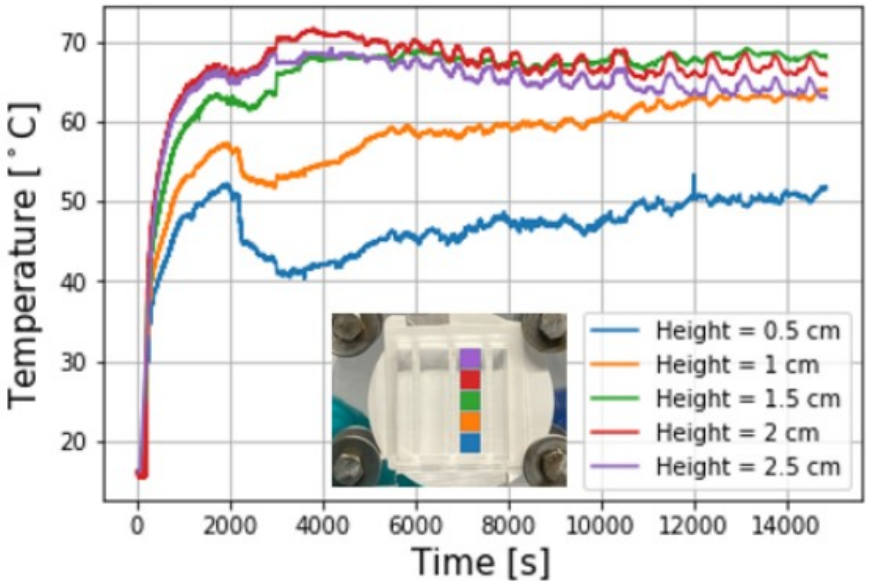

Figure 5.35: Temperature versus time plot at various height along the cell. Source: Leijn et al. [41]. Temperature oscillations can be seen for $t \geq 4000$ s. Heights 0.5 cm and 1 cm shown out of phase behaviour.

The dynamic temperature response for the segmented cell is absent at the moment electrolyte supply ceases. This can be seen from Figure 5.34 and the refilling frequency from Figure 5.36 at $t = 4140$ s when the top reservoir is empty and the volume of liquid in the bottom container is noted. Until $t = 4380$ s the cell shows a linear increase in temperature, indicating that locally the electrolyte has been evaporated.

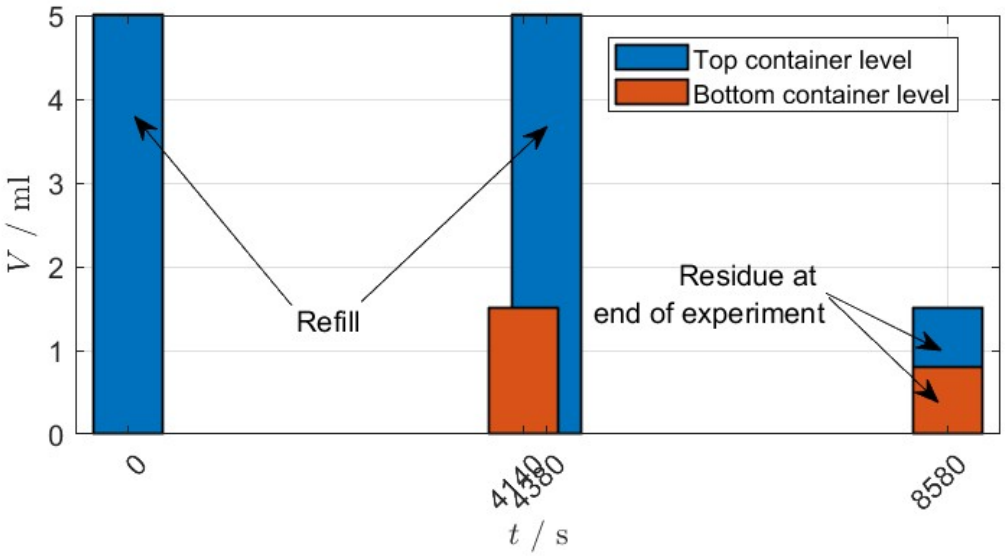

Figure 5.36: Refilling frequency versus time. Plot shows the top and bottom container liquid level. Bottom level is recorded at the instant the top reservoir is empty. The last measurement is done at the end of the experiment.

Electrolyte replenishment

Figure 5.36 shows the filling frequency of the top reservoir. Heat generated from exothermic electrochemical reactions leads to electrolyte evaporation with local scarcity of electrolyte as a consequence. Subsequently, resistive heating slowly takes over until a new injection of (diluted) electrolyte into the top reservoir, which happens at $t = 4380$ s into the experiment. The effect can be seen to bring the system back to an ”equilibrium” temperature before the current is increased and a similar pattern can be observed until the current is increased. This oscillatory effect is seen to be of larger amplitude for 5000 s$\leq t \leq$ 7000 s.

Water consumption

A total of 10 ml is supplied to the cell of which 2.3 ml is recovered via the bottom reservoir. This equates to 6.2 ml of water that is used by the cell. Figure 5.37 shows the calculated volume of water consumed according to Equation 5.9. The sum of consumed water from Figure 5.37 totals approximately 0.16 ml. Assuming the remainder is evaporated, this would equate to roughly 6.04 ml.

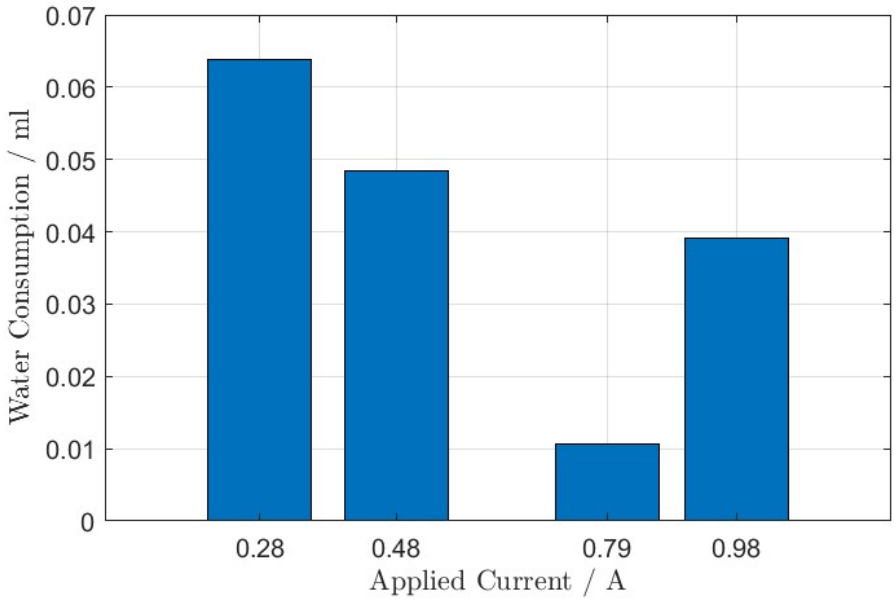

Figure 5.37: Total water consumption at the four distinct applied currents. Standard conditions for water have been assumed here to gain an estimate for the consumed volume. Segment area is $A = 12.5$ cm^2.

5.5.2. 2 Segment Constant Current Top-Down Experiment

Experimental results on the 2 segment constant current top-down experiment utilising 2M KOH as the electrolyte are shown discussed here. An OWON SPE6103 power supply has been used to power the second segment. Membrane wetting took approximately 13 minutes for the 2 segments. Figure 5.38 shows thermal images of the cell during membrane saturation and during start-up.

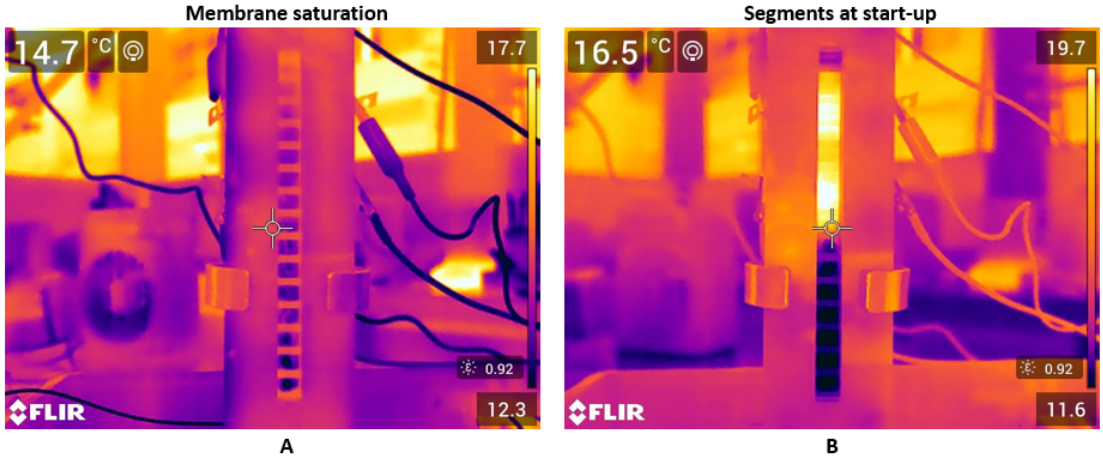

Figure 5.38: FLIR E75 thermal images taken during experiments with 2 segments. A: Shows the low temperature coloring of the electrolyte saturating the membrane. B: Snapshot of the cell at start-up of the experiment.

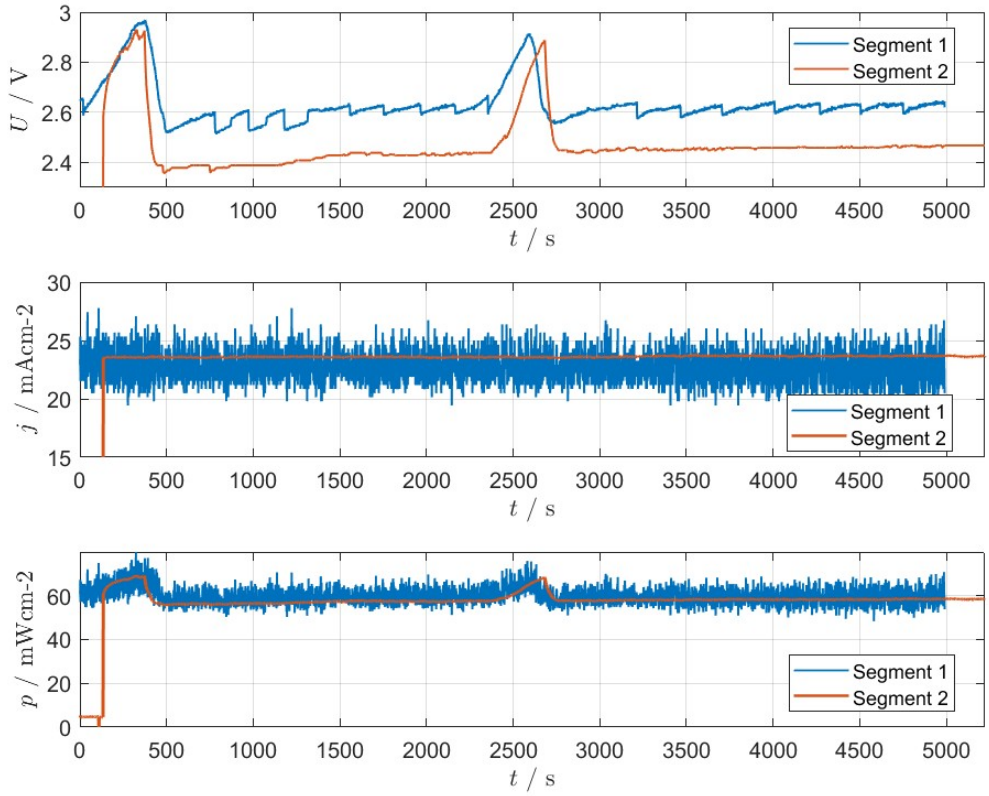

Figure 5.39: Results for 2-segment top-down experiment performed at constant current. The top two segments have been used. Plots show voltage, current density, power density and reservoir volume over time, respectively. The experiment was conducted at a single constant current density to expand the research on local flooding and downwards flow of electrolyte.

Figure 5.39 presents the voltage, current and power density data versus time. It can be seen that the voltage response of Segment 1 exhibits a rather repetitive profile of increase followed by subsequent decrease, resembling a sawtooth trend. This process repeats around an average potential of $U_{S1} = 2.63$ V. However, no new injection of electrolyte is introduced to the top reservoir until $t = 2700$ s.

Electrolyte replenishment

A total of 10 ml has been supplied of which 4.75 ml is retrieved through the bottom reservoir. Using Equation 5.9 for the 2 segments results in a total theoretical water consumption of 0.14 ml. Assuming the difference of 5.11 ml is evaporated.

The dynamic sawtooth behaviour is only seen with Segment 1. It is the first segment that comes into contact with fresh electrolyte. This can be seen from the refilling frequency shown on Figure 5.40.

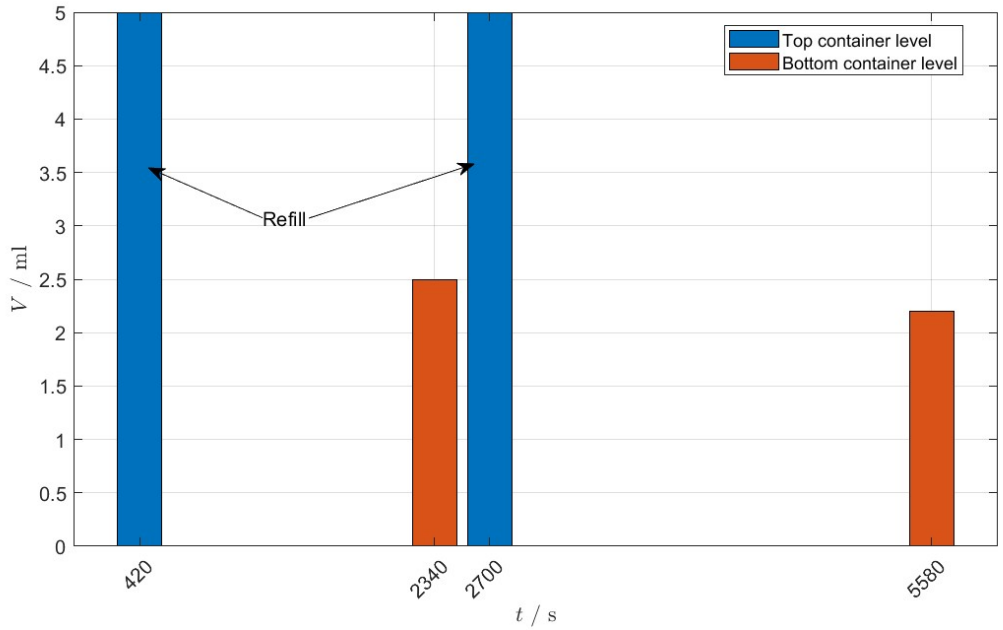

Figure 5.40: Refilling frequency versus time. Plot shows the top and bottom container liquid level. The bottom reservoir level is measured at the instant the top reservoir is empty. At $t = 5580$ s the residual water level is measured when the power supply has been turned off.

The observed profiles around the moments of refilling show how introducing small amounts of fresh electrolyte to the electrode affect the potential. At $t = 2340$ s the bottom reservoir contains the residue electrolyte. At this time the top reservoir contains no liquid. This can be observed for a period of 6 minutes during which the measured potential increases linearly before a feed is re-established at $t = 2700$ s by refilling. This electrolyte injection brings the system back down to an average cell potential similar to that before injection.

Presumably, a similar phenomena is present which leads to the sawtooth trend. As long as there is feed, the potential is affected. However, the origin of the subsequent increase is not clear.

Temperature

The accompanied temperature response for segment 1 is shown on Figure 5.41. The height specific measurements along the vertical length of the segments show oscillatory behaviour over time. This effect can be seen more prominently for Segment 2 in Figure 5.42. All ROIs experience this oscillatory behaviour. However, compared to those shown in section 5.5.1, the frequency of the oscillations in segment 2 appears to be significantly lower frequency at roughly 0.005 Hz, considering a 1000 second time window.

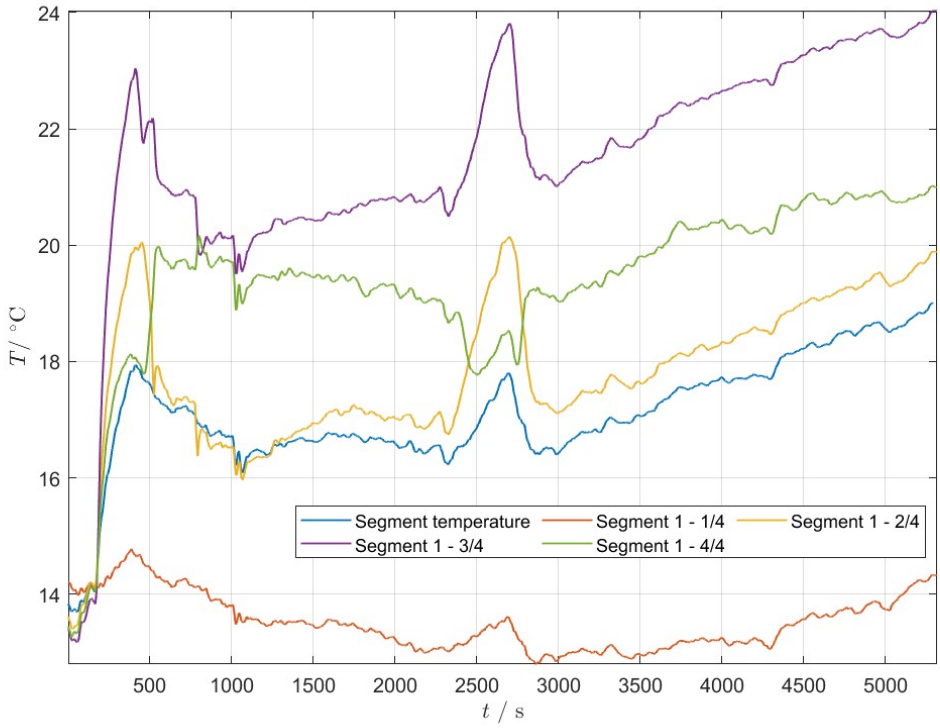

Figure 5.41: Temperature results for the top segment. Experiment has been performed on constant current and ambient conditions. Plots show segment temperature and height-specific temperature versus time, respectively.

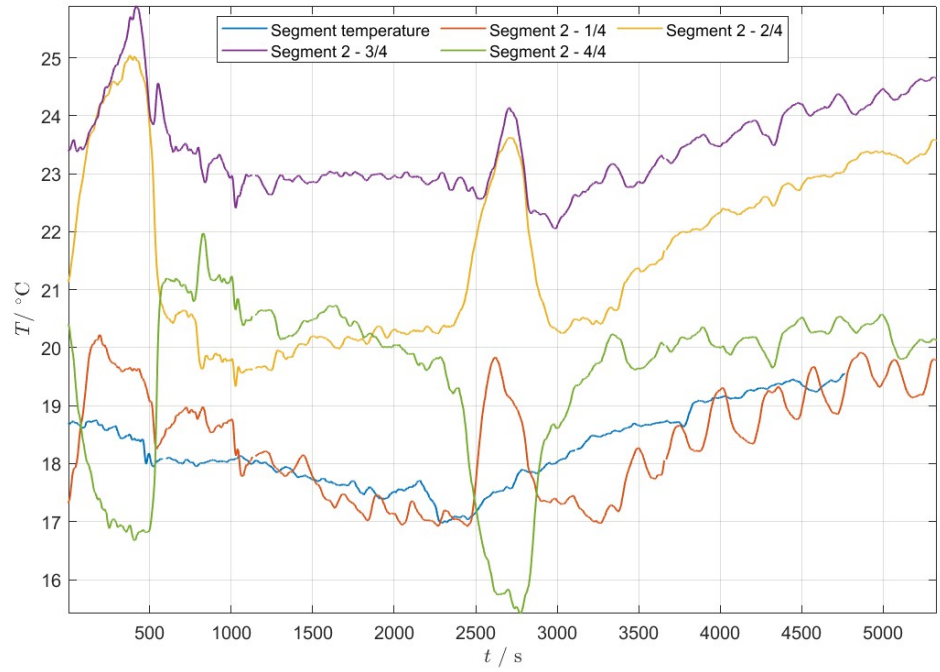

Figure 5.42: Temperature results for the second segment. Experiment has been performed on constant current and ambient conditions. Plots show segment temperature and height-specific temperature versus time, respectively.

5.5.3. 4 Segment Constant Current Top-Down Experiment

Experiments have been performed with the cell at full operation, i.e. all segments are powered. Similar to the previous experiments the topmost segment is powered by a Delta Elektronika SM45-140 and the remaining segments are all powered by their separate OWON SPE6103 power supply. Hence, a total of 4 power supplies are connected to the cell. Figure 5.43 shows the 4 segments that have been monitored during the experiment.

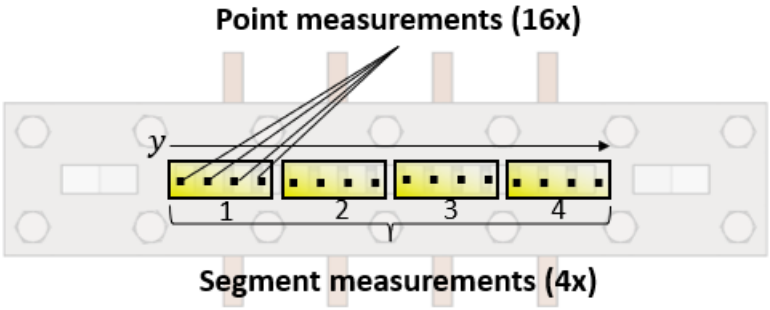

Figure 5.43: Sketch of the cell showing the 4 segments in use and 16 point measurements over the length of the cell (4 per segment). Note that the cell is in the upright position but is shown horizontally in this figure.

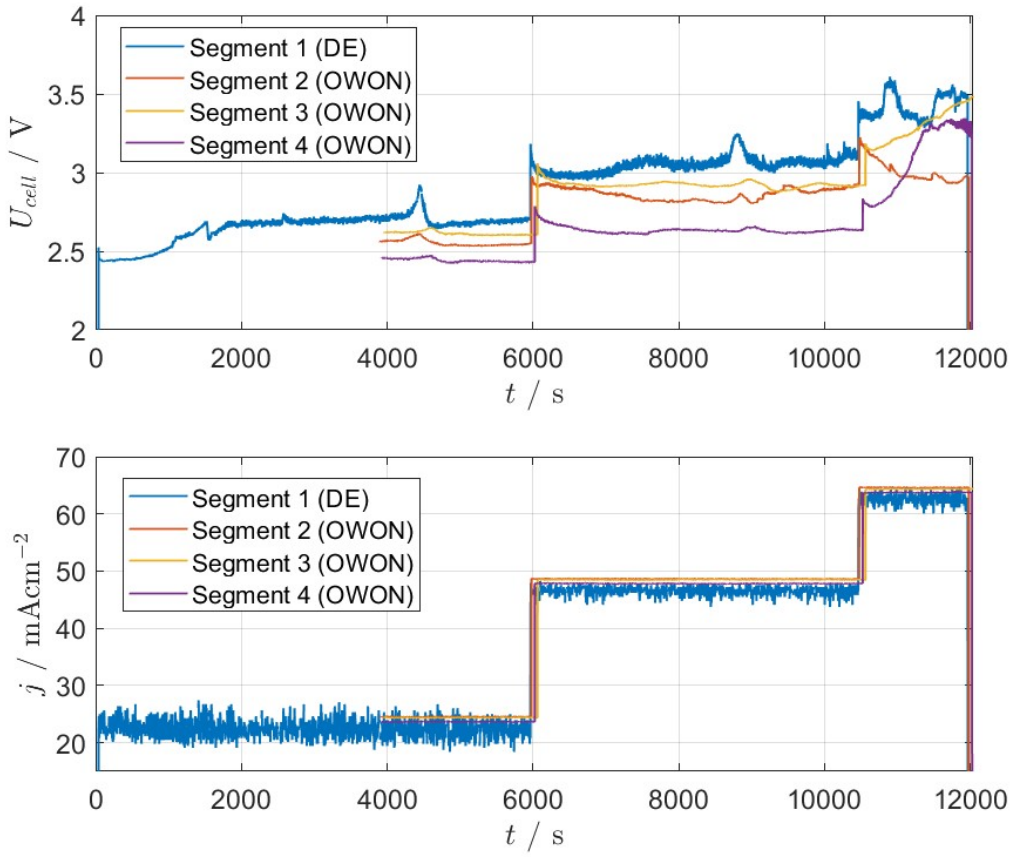

Figure 5.44: Results for 4-segment top-down experiment performed at constant current. Plots show voltage and current density versus time.

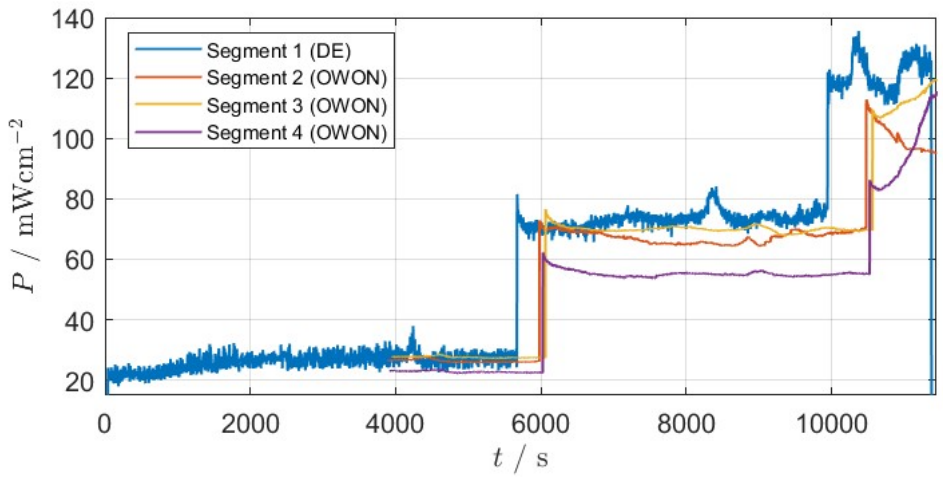

Figure 5.45: Results for 4-segment top-down experiment performed at constant current. Plots show power density versus time for every segment.

Figures 5.44 and 5.45 present the voltage current density and power density versus time, respectively. A 2M KOH electrolyte was used to facilitate top-down wetting of the membrane. Wetting was done during a period of 22 minutes. Segment 1, i.e. the topmost segment experiences the highest measured potential.

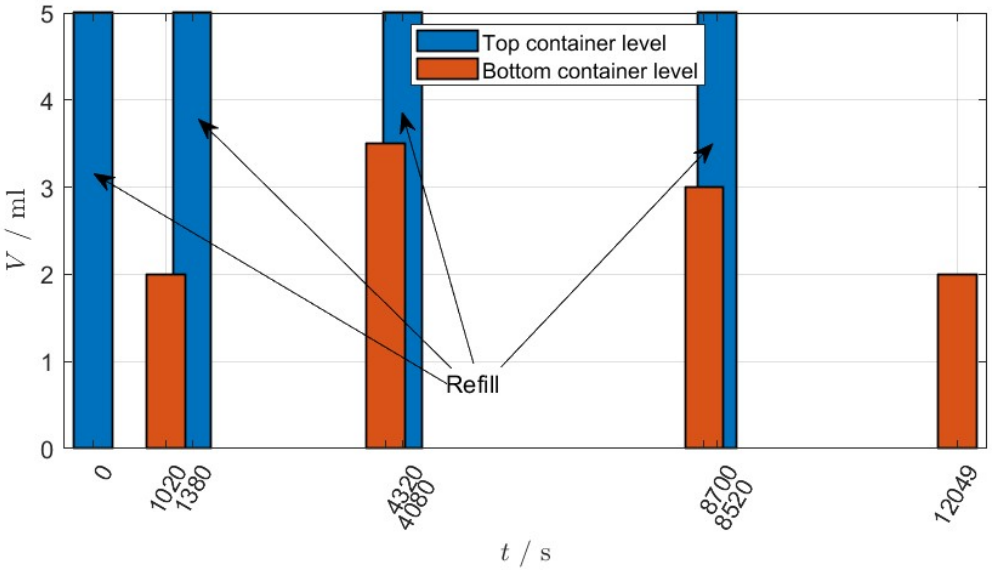

Figure 5.46: Plot shows the top and bottom container liquid level. The refilling of the top reservoir is indicated. The bottom reservoir level is measured at the instant the top reservoir is empty. This is the excess volume of water that drips into the reservoir. This volume is extracted, diluted and reintroduced to the top reservoir shortly after. Note that time instances $t = 4080$ s and $t = 8520$ s correspond to the bottom reservoir.

Electrolyte replenishment

During the experiment, three processes of flushing and refilling can be distinguished. These are shown on Figure 5.46. A total volume of 20 ml has been injected during the experiment. A volume of 10.5 ml has been recovered from the bottom reservoir. Meaning that 9.5 ml is consumed by the cell. The first peak observed in the $U-t$ plot is quickly diminished due to injection of new volume of electrolyte into the top reservoir at $t = 1380$ seconds into the experiment. However, the voltage keeps rising afterwards, indicating that electrolyte would have been locally evaporated and not along the whole segment. From the electrolyte injections it can be seen that the period of sustaining electrolysis without top or bottom feed seems to shorten. Naturally, the last process can be attributed to operation at current densities close to 3 times larger than initially started with. Local maxima observed in the $U-t, P-t$ and $T-t$ plot during the time interval $6000\ s \leq t \leq 10000\ s$ are recovered back to magnitudes before the increase had set in.

Water consumption

Figure 5.47 shows the water consumption at the various applied currents. Equation 5.9 describing Farday's law of electrolysis has been applied here. Theoretically, this shows that total volume of water consumed is approximately $V_{\text{cons}} = 1.05$ ml. Assuming that this is predominantly due to evaporation, this accounts to a volume of 8.45 ml that is evaporated during the experiment. Furthermore, we also assuming the evaporation rate follows a linear trend between subsequent refilling of the top reservoir.

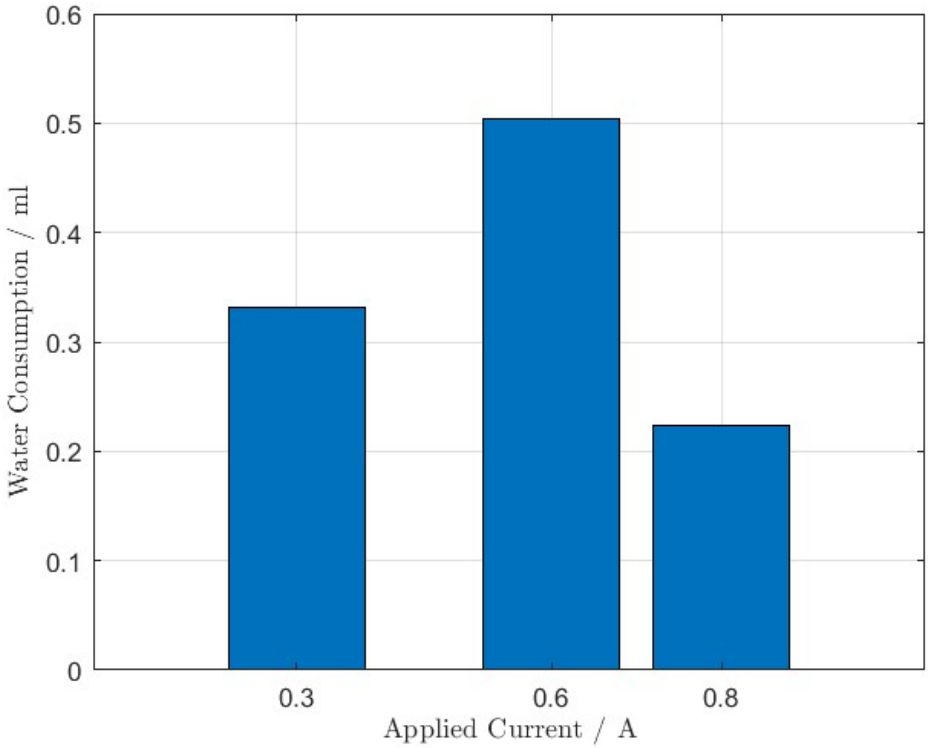

Figure 5.47: Total water consumption at three distinct applied currents. Standard conditions for water have been assumed here to gain an estimate for the consumed volume.

Enthalpy of vaporization

We can again utilise the rate of water consumption, enthalpy of vaporization and specific heat capacity from Equation 5.14 to estimate the associated heat transfer coefficient per segment. These are shown in Table 5.2.

Est. heat transfer coefficients		
Segment	$\dot{m}(\cdot 10^{-6})$	h
-	**kg/s**	**W/m^{2}K**
1	2.9	85.93
2	0.6	16.23
3	0.5	13.91
4	0.9	26.17

Table 5.2: Estimated heat transfer coefficient. Equation 5.14 has been utilised for every segment. Assuming the evaporation rate follows a linear profile between subsequent replenishments of the top reservoir.

Oscillations

Large irregularities can be observed at $t \approx 10500$ s for voltage and power density. Figure 5.48 shows a zoom of this region from the voltage versus time plot. At this time there is still a feed of electrolyte from the top reservoir. Presumably, liquid is evaporated quicker than that it can reach segments further down. This can also be seen from the measured potential. There is no replenishment. Segment 1 shows an increase followed by a decrease without reaching a steady state value. Segments 3 and 4 experience a steep rise. Particularly segment 4 shows high frequency oscillations for $t \geq 11700$ s.

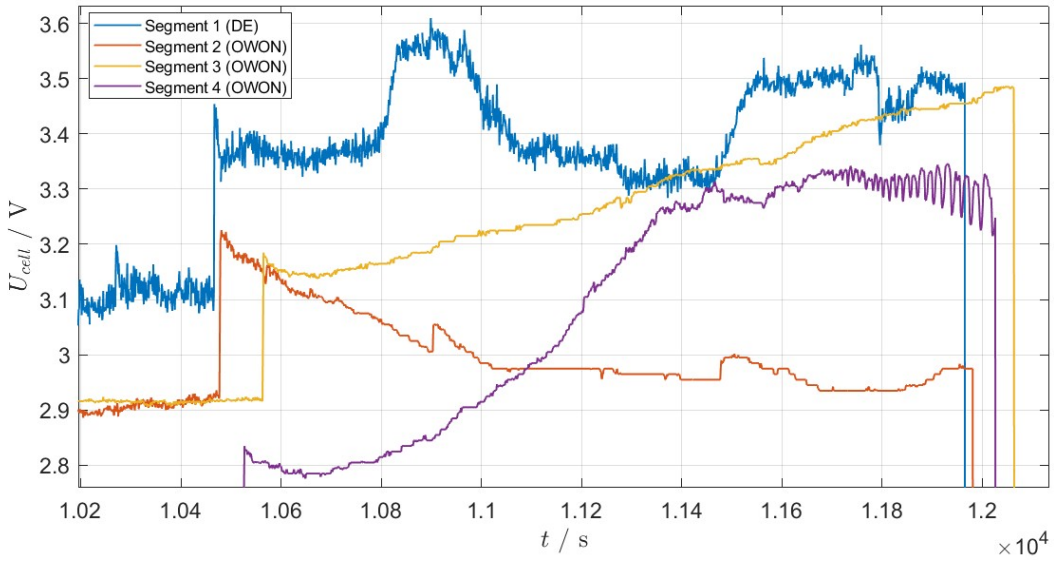

Figure 5.48: Voltage versus time plot from Figure 5.44. The highly oscillatory region starting at approximately $t \geq 10500$ s has been zoomed in.

Temperature versus time

The trend shown for Segment 1 and 2 grows towards a steady state, i.e. the slope decreases. However, for Segments 3 and 4 the linear rise is unobstructed. Due to the increasing irregularities in the measured voltage at this time the experiment was ceased to preserve the membrane and electrodes. Figures 5.49 and 5.50 highlight every segment together with 4-point ROIs along each segment. With the first two increases in current it can be seen that all segments exhibit a close to parallel temperature evolution over time. Increase and decrease due to fresh electrolyte injection can also be seen. The top segment experiences the introduction of cooler fresh electrolyte first. Segment 1 - 1/4 remains at low temperature followed by segment 1 - 4/4, with the center comprising the hottest part. Segment 2 deviates from this behaviour. The two lower parts of the segment remain the coolest whereas the top half experiences higher temperatures. Interestingly, segment 4 - 4/4 shows inactivity during the experiment which is very likely due to poor electronic conductivity.

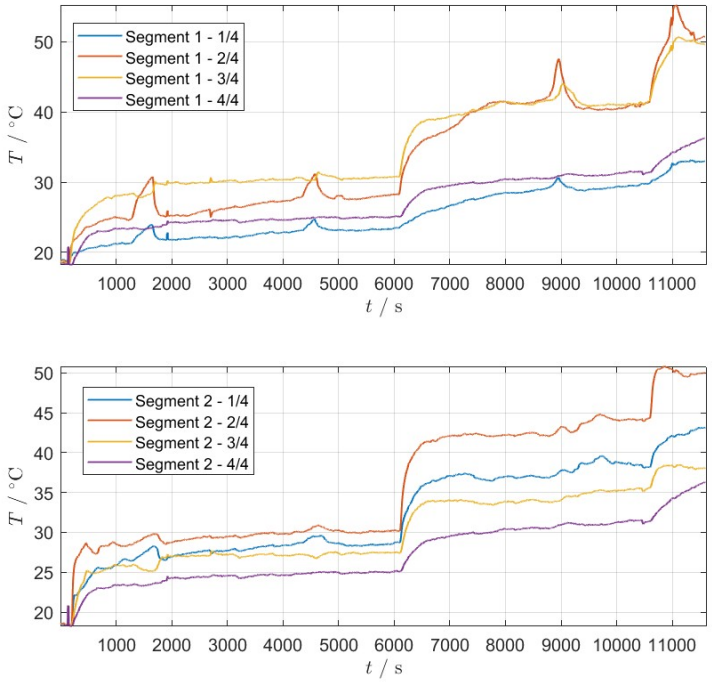

Figure 5.49: Results for 4-segment top-down experiment performed at constant current. Plots show height-specific temperature versus time for segment 1 and 2, respectively.

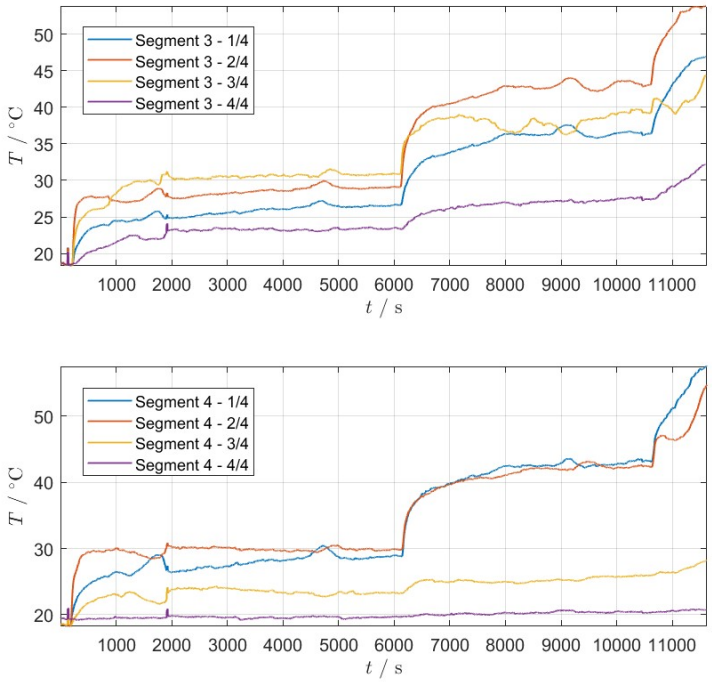

Figure 5.50: Results for 4-segment top-down experiment performed at constant current. Plots show height-specific temperature versus time for segment 3 and 4, respectively.

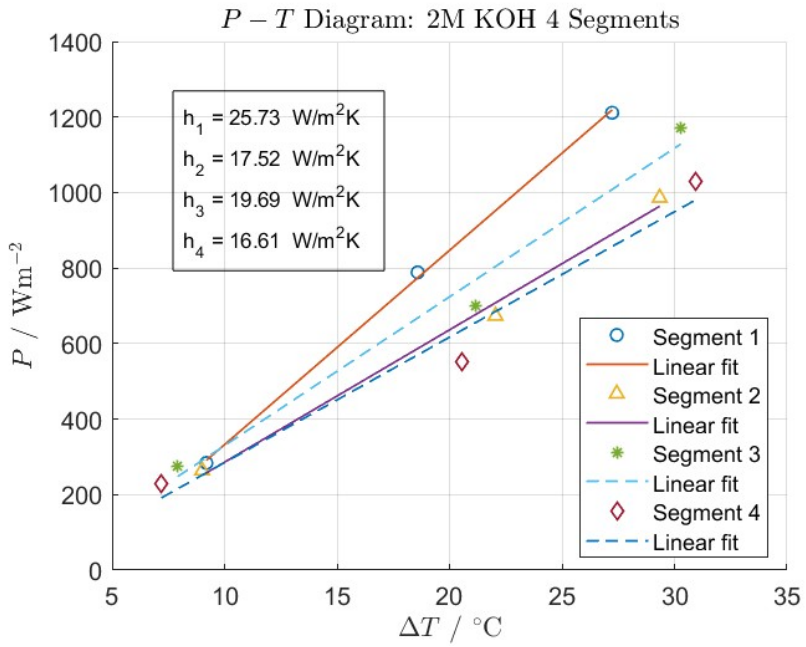

Figure 5.51: Power density versus temperature for 4-segment constant current top-down experiment. Plots show trends for each segment along with their respective linear fits. The accompanied heat transfer coefficient derived from the slope of the fits has also been shown.

Power density versus temperature

Figure 5.51 shows the power density against temperature difference. This evidently shows that the distribution is not uniform along the segments at different heights. Segment 1 shows the largest power density over temperature difference. This is the first segment that is supplied with a fresh electrolyte feed. Heat transfer coefficients are determined using Equation 5.7 and show relatively similar outcome for segments 2 and 3 compared to the procedure that follows Equation 5.14. Segments 1 and 4 appear to be greatly overestimated primarily due to the relatively large evaporation rates. Figure 5.52 shows the associated convective heat transfer coefficients according to Van Vliet et al. Similar to what is seen for the small cell, this indicates that convection is not the dominant mechanism for heat dissipation.

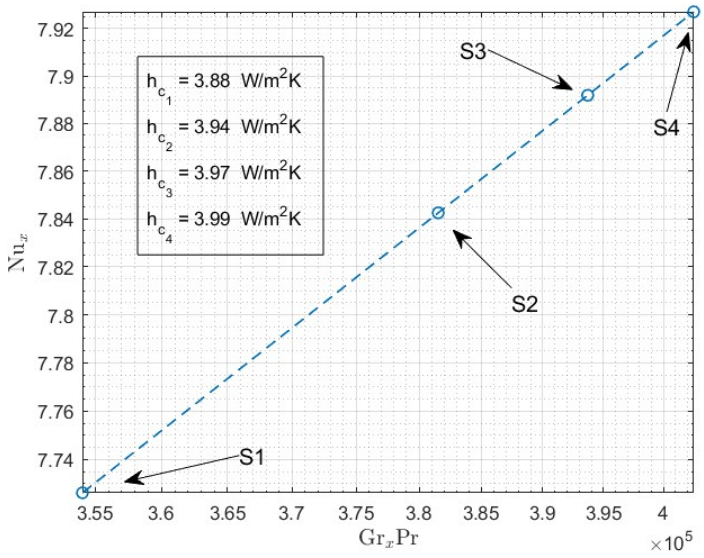

Figure 5.52: Approximation for the local Nusselt number from the empirical relation given by Van Vliet et al. Standard conditions for air have been used.

5.5.4. Porous Conducting Layer

The 4 segment top-down experiment has shown that large potentials arise during electrolysis at relatively low current densities using 2M KOH as the electrolyte. A limiting factor in the power connection for this architecture is that of poor electronic conduction in the vertical direction along the segment. Consequently, this impedes performance as we pose an ohmic resistance to the flow of electrons towards the segment where they can be oxidized or reduced.

Nickel-mesh electrodes		
Characteristics	**Magnitude**	**Units**
Length	60	mm
Width	10	mm
Thickness	0.5	mm
Resistivity	$1.005 \cdot 10^{-5}$	$\Omega \cdot$ m
Resistance	0.1205	Ω

Table 5.3: Dimensions of Nickel-mesh electrodes with accompanied resistance measurement. Obtained from cyclic voltammetry utilising a GAMRY potentiostat.

Nickel Fiber Felt

Table 5.3 shows dimensions of the nickel-mesh flaps. In order to facilitate continued unobstructed gas diffusion towards the environment while at the same time enhance the performance of the cell, a porous conducting layer was placed on the electrode segments. The choice was made to utilise Nickel Fiber Felt material for the conducting layers. Details on the material are shown in Table 5.4. We utilise a material that is less rigid than e.g. expanded metals and would prevent large gaps between the PMMA plates from forming. Figure 5.53 shows a three fold view of the cell with the Nickel Fiber Felt material integrated.

Porous Conducting Layer				
Material	A_{surf} **cm**^{2}	t **mm**	ϵ **-**	**Quantity -**
Nickel Fiber Felt	67.5	0.40	0.60	8

Table 5.4: Properties of Ni Fiber Felt utilised as a porous conducting layer in the segmented cell. Pieces of 4.5$\times$15 cm^2 have been utilised.

Material preparation and connection

Before use the electrodes have been cleaned using a BRANSON 2800 sonic bath. For a period a 300 seconds the electrodes were sonicated while placed in acetone. Afterwards, the process was repeated with pure water. In order to establish improved electron conductivity a set of two crocodile clamps have been connected to each flap, which totals the use to 16 clamps per 8 flaps connected to 4 power supplies. Consequently, the aim is to facilitate improved vertical electronic conductivity such that the nickel-mesh electrodes will experience a well distributed current density.

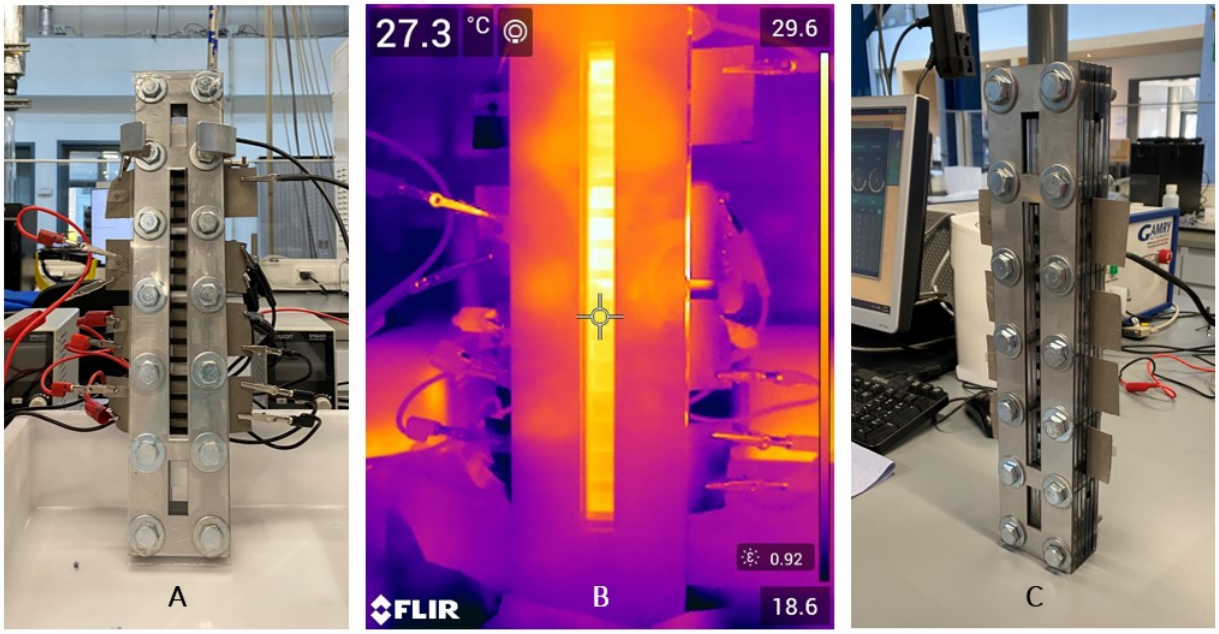

Figure 5.53: A: Segmented cell with Nickel Fiber Felt conducting layers added and connected to power supplies, B: Thermal snapshot of cell during electrolysis, C: Isometric view of segmented cell with Nickel Fiber Felt conducting layers.

Electrolyte replenishment

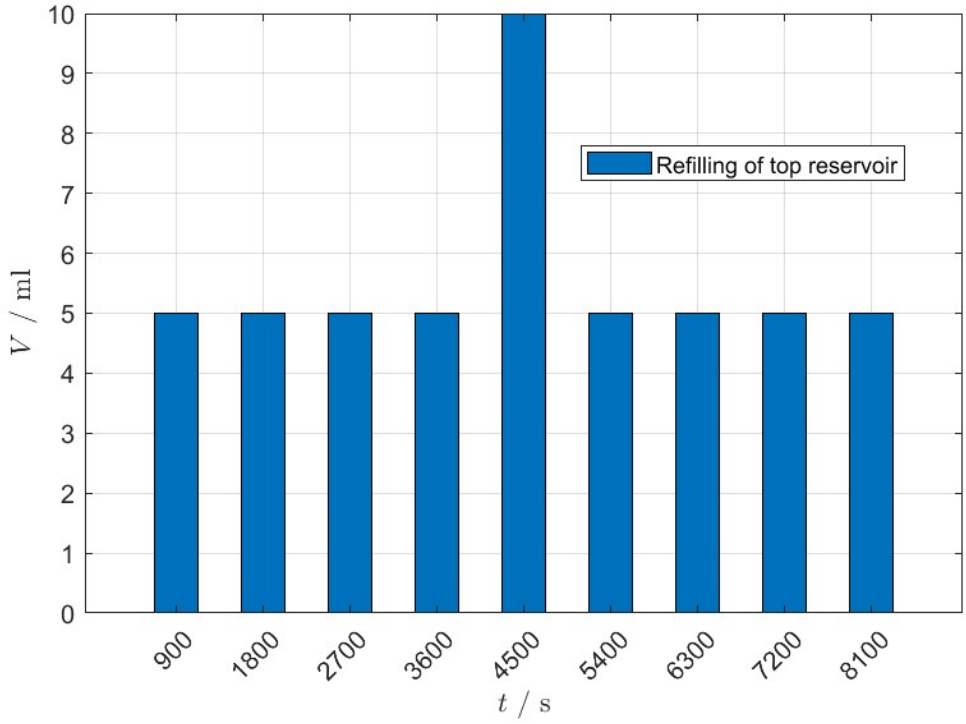

Figure 5.54: Refilling of the top reservoir. Every replenishment has been done with fresh electrolyte. At the moment of replenishment the reservoir was empty. Replenishment took place every 15 minutes for a period of 2.25 hours.

The filling frequency of the top reservoir has been shown in Figure 5.54. Due to the added Nickel Fiber Felt materials on top of the nickel-mesh electrodes, minor leakage was detected from the bottom reservoir during experimentation. The Nickel Fiber Felt added an extra 0.80 mm spacing between the

PMMA plates that holds the conducting layer and MEA together. Consequently, the dilution process as described in Figure 4.5 was not utilised here. Instead, fresh 2M KOH electrolyte was added to the top reservoir every 15 minutes. At $t = 4500$ s the added electrolyte was doubled to verify whether it would impact the potential and temperature evolution over time at higher current densities. This addition did not have a significant effect compared to the initial 5 ml that was used. Consequently, the additions have been kept at a constant volume afterwards. Hypothetically, the electrolyte replenishment and the subsequent voltage and temperature drop seen for all segments could indicate that the feed does not encounter obstructions towards segment 4. Alternatively, the increase that is seen can be attributed to the absence of water.

Voltage and current density

Figure 5.56 shows a zoomed in representation of the potential versus time to show the dynamic behaviour of the profiles during the experiment. A sawtooth profile can be observed. From a first comparison with the non Nickel Fiber Felt addition, a reasonably stable and repetitive cell voltage can be observed. Interestingly, Segment 3 exhibits a sawtooth profile at various scales, i.e. a sawtooth-in-sawtooth trend can be observed. Segment 1, 2 and 3 do not seem to have this effect. From the previous experiment, the poor electrical conductivity was the limiting factor, driving the potential up at high current densities.

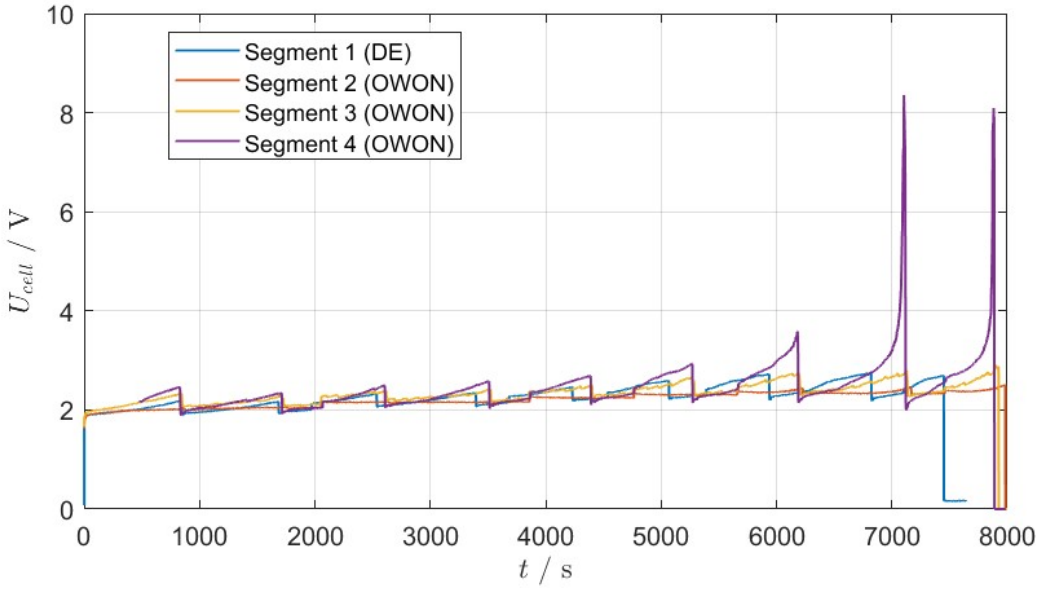

Figure 5.55: Voltage measurements plotted against time. A sawtooth profile can be seen. Potentials rise directly after each electrolyte replenishment. Very large overpotentials can be observed for segment 4 for $t \geq 7000$ s.

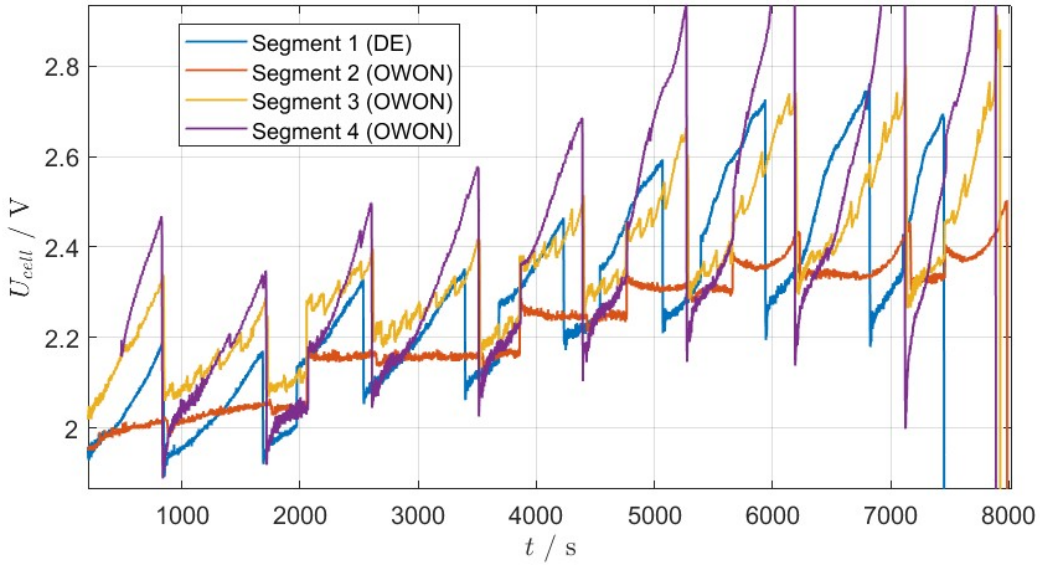

Figure 5.56: Zoom of sawtooth graphs seen in Figure 5.55. Segment 1, 2 and 4 display the sawtooth profile. Additionally, segment 3 exhibits a sawtooth-in-sawtooth profile. Segment 2 does not show this oberved profile.

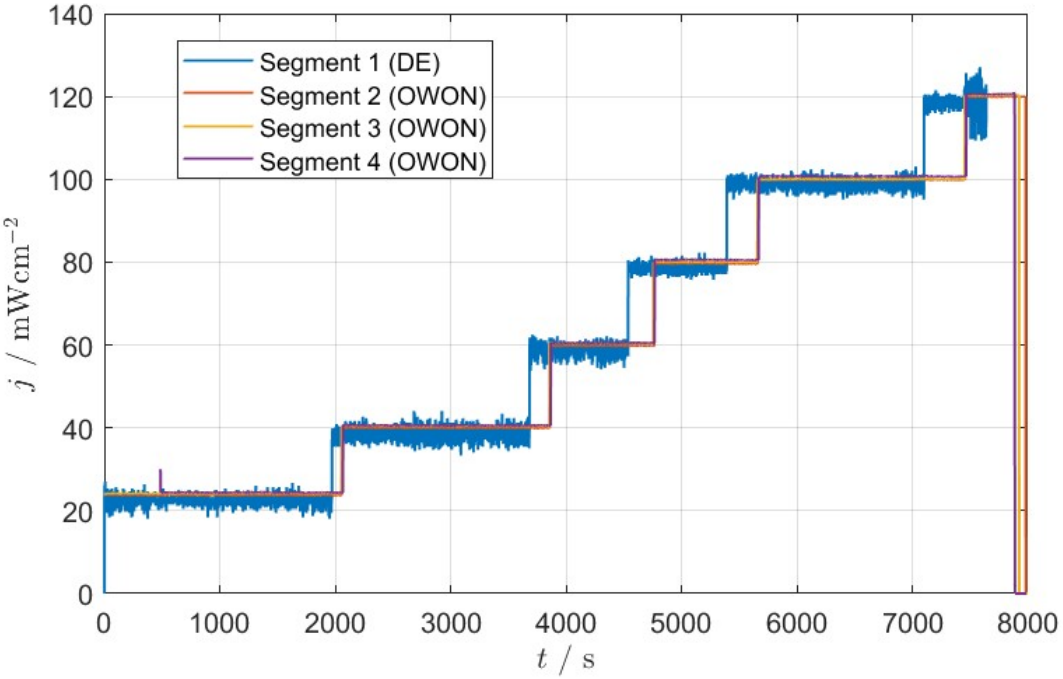

Figure 5.57: Measurements of current density versus time. Six increases in current have been applied to the segmented cell. Subsequent increases in applied current were done at various time instances to aid post-processing the data.

Saturation of conducting layers

During membrane saturation it occurred that the Nickel Fiber Felt material also experiences a saturation process in which electrolyte enters the material through capillarity. From a thermal image shown Figure B.5 in Appendix B.5 it can be seen more clearly. The porous conducting layers do not only provide improved conduction towards the nickel-mesh electrodes. They also aid capillary action. In fact, this observation shows that at the segments there is likely a lateral dual feed of electrolyte through capillary action from the diaphragm and the felt material. As the conducting layer is pressed onto the nickel-mesh and polyethersulfone diaphragm through PMMA compression, presumably the conducting layer also acts as a compressed sponge. However, as this is more speculation, the sawtooth(-in-sawtooth) profile could be attributed the consequence of this.

Temperature

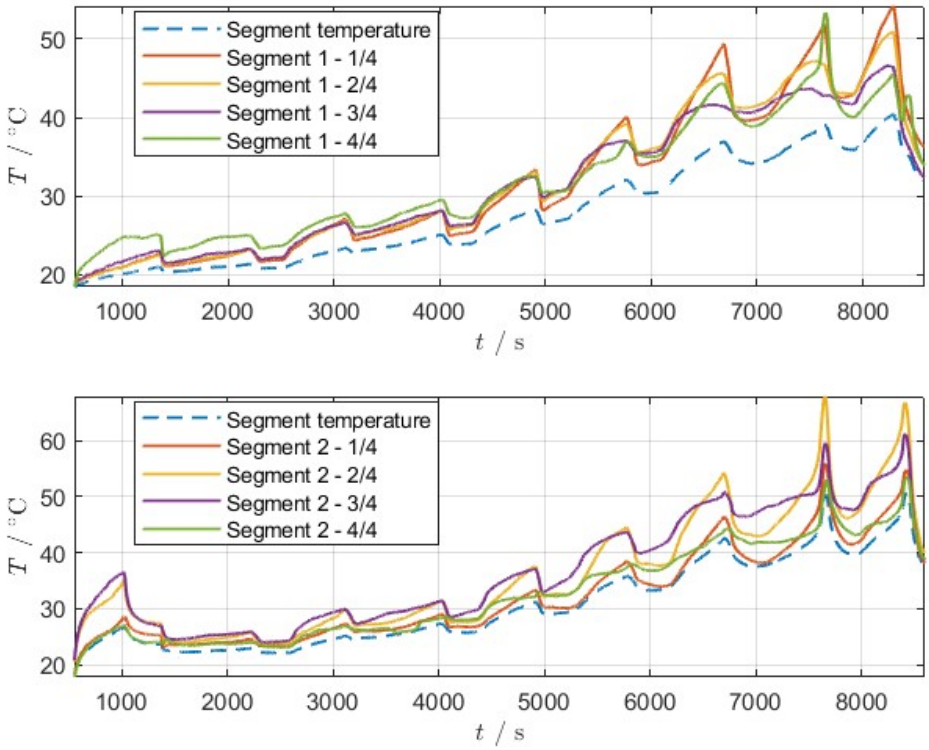

Figure 5.58: Temperature results for segments 1 and 2 performed at constant current. Plots show height-specific temperature versus time. The overall segment temperature has also been shown.

Figure 5.58 presents the height-specific temperature. The graphs show a decrease with every electrolyte injection and increase with every subsequent increase in applied current. As we only measure the Nickel Fiber Felt temperature evolution, soaked with electrolyte, this could explain the difference that we observe. Furthermore, compared to the non Nickel Fiber Felt case. the profiles seem to follow each other relatively well with only a few degrees apart between point ROIs.

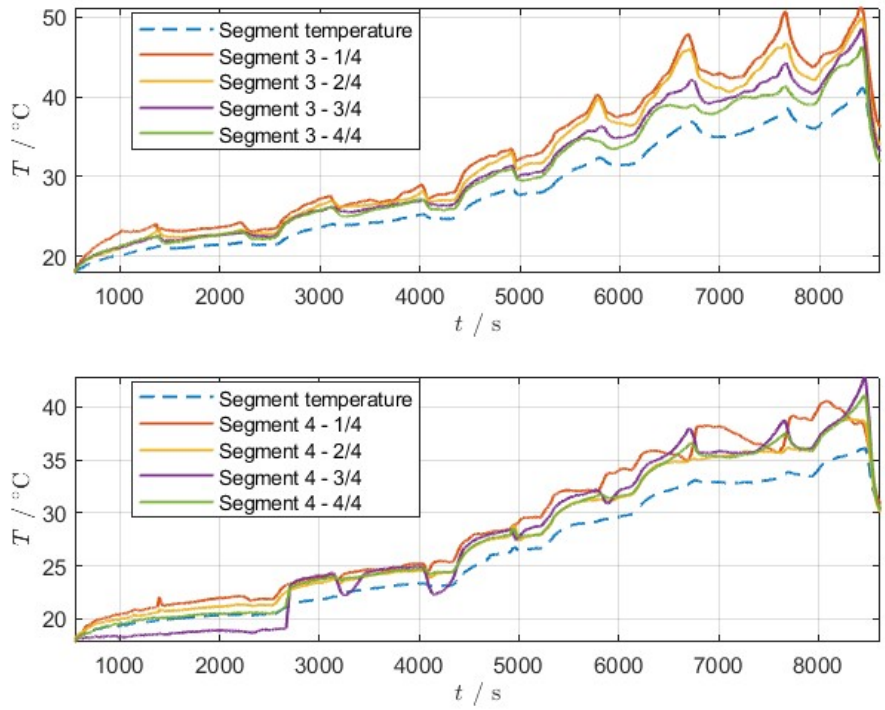

Figure 5.59: Temperature results for segments 3 and 4 performed at constant current. Plots show height-specific temperature versus time. The overall segment temperature has also been shown.

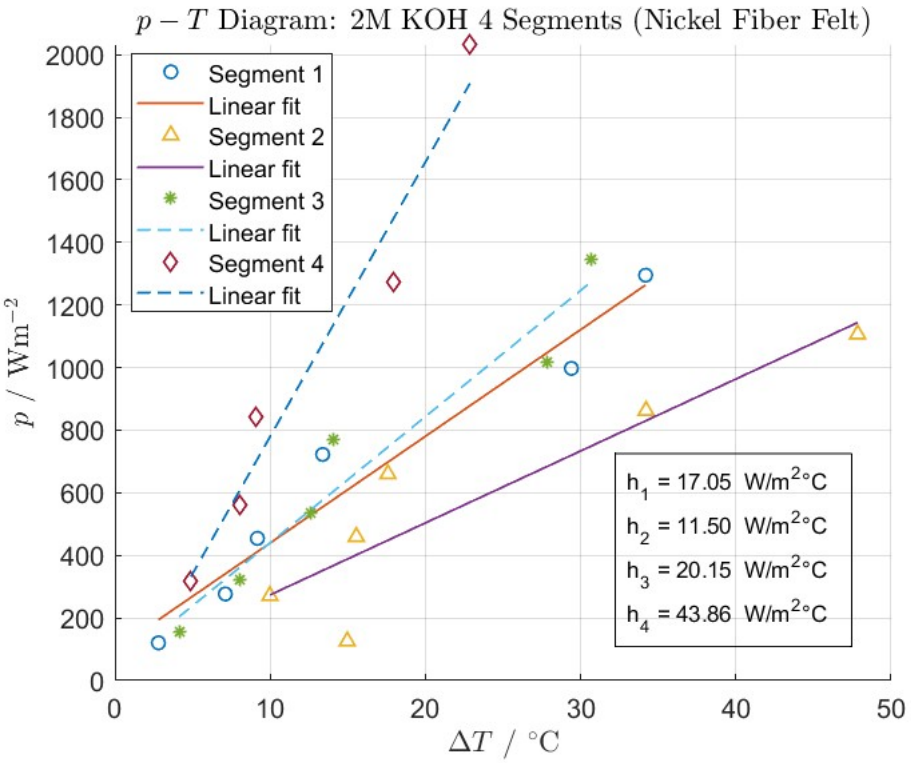

Figure 5.60: Power density versus temperature for 4-segment constant current top-down experiment performed with Nickel Fiber Felt conducting layers. Plots show trends for each segment, respectively.

Power density - temperature characteristic

With regard to the energy that goes into heating, we can again relate the power density distribution against temperature. This is shown in Figure 5.60. Interestingly, Segment 4 shows an steep increase in measured power density while the measured temperature is relatively low. The heat transfer coefficient has also been calculated. This is derived from the slope of the linear fit of the power density versus temperature graph. Graphically, this is shown in Figure 5.61. The shows that the convective component of the heat transfer coefficient is rather low. This would mean that the dominant heat transfer takes place through conduction and radiation.

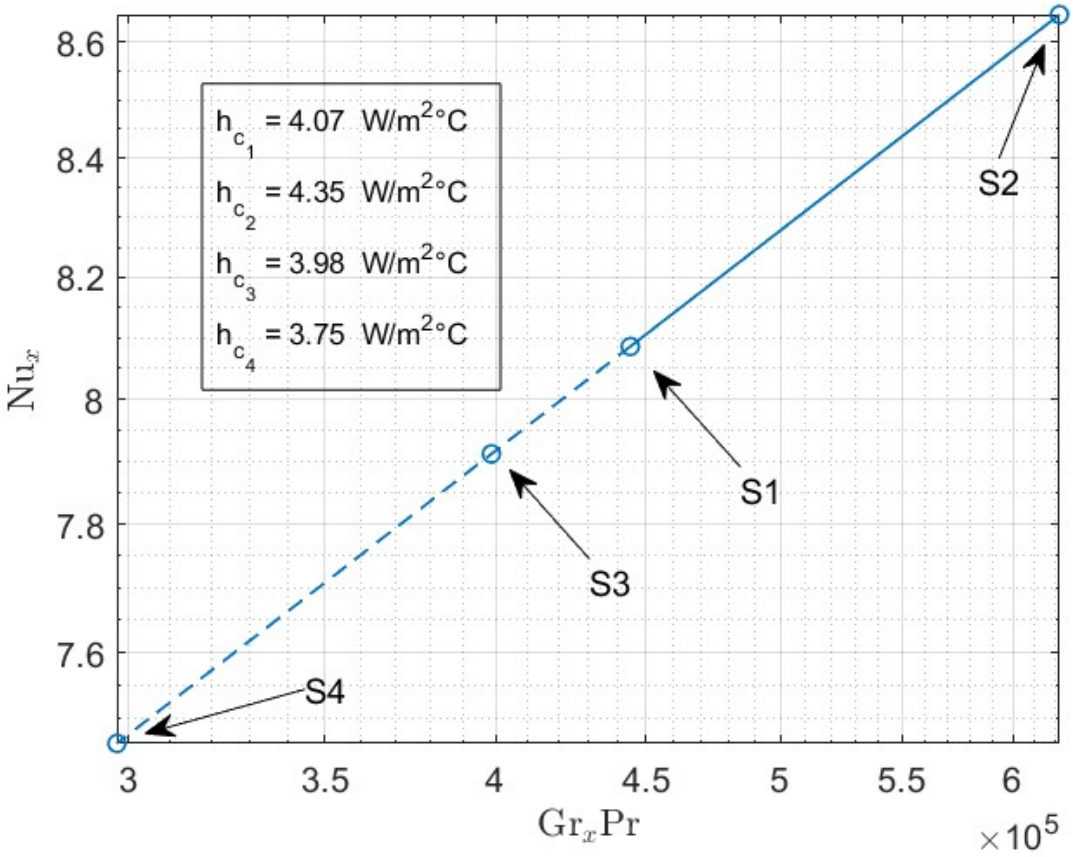

Figure 5.61: Approximation for the local Nusselt number from the empirical relation given by Vliet et al. Standard conditions for air have been used. Each segment has been indicated separately.

5.6. Current-potential characteristic

To compare the experiments with each other we can relate the current-potential characteristics. Over-potentials of interest are the ohmic and activation losses. These have been discussed in Section 2.4. Expressing the total overpotential as a summation of the ohmic and activation contribution, we find an expression of the form:

$$U_{\text{cell}} = a + b\ln(j) + cj \tag{5.15}$$

In which a is the Tafel intercept, b Tafel slope and c a coefficient that is equal to the area specific resistance AR, the product of the electrode area A and the resistance R. For the Tafel intercept 1.23 V was taken, equal to the open circuit potential. The Tafel slope and ohmic resistance can be determined by rewriting Equation 5.15 to:

$$\eta_{\text{tot}} = 1.23 + b\text{asinh}\left(\frac{j}{2j_0}\right) + cj \tag{5.16}$$

Current-potential diagram small cell

For the experiment utilising the small cell and 6M KOH as the electrolyte we see the $j-U$-characteristic as shown in Figure 5.62. The fit has been made utilising Equation 5.16. The higher concentrated KOH shows increased conductivity as expected. In the interval 0.2 Acm$^{-2} \leq j \leq 0.9$ Acm^{-2} a linear trend with respect to voltage can be seen. Originating from approximately 2.25 V towards 4.0 V close to $j = 1.0$ Acm^{-2}. Measured cell potentials of this magnitude for this cell has led to damage to the cell components as was shown in Figure 5.22.

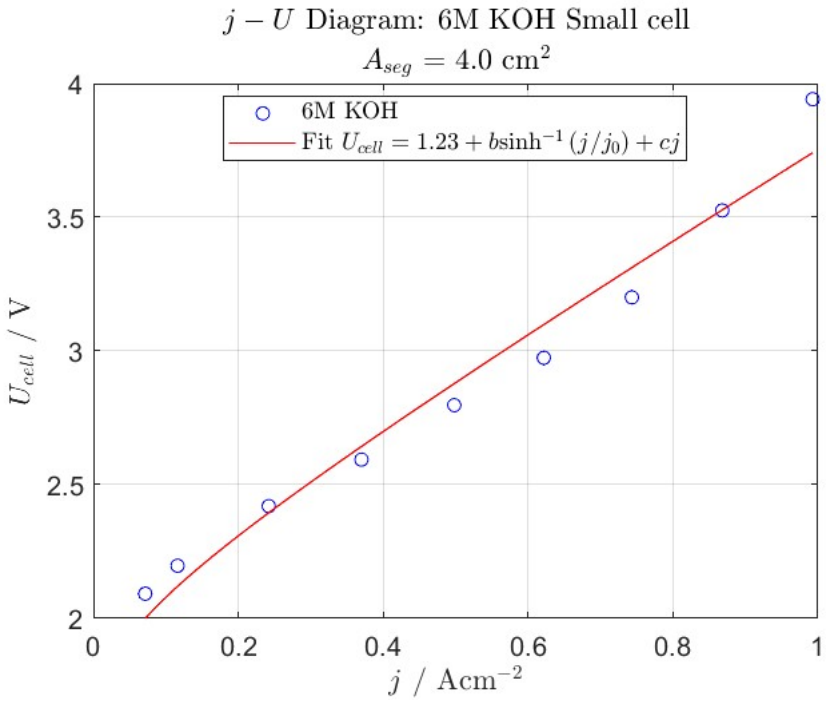

Figure 5.62: $j-U$ Diagram for experiment performed with the small cell utilising 6M KOH as the electrolyte solution.

Current-potential diagram segmented cell

Figure 5.63 shows the current-potential characteristic for the cell utilising all segments. Shown are the characteristics for segments from top to bottom, i.e. $1,\ldots,4$ with the corresponding fits. This can be compared with Figure 5.64 in which the Nickel Felt Fiber conducting layers have been added to each subsequent nickel-mesh electrode. For the same current density, the addition of the conducting layers shows improved performance. The measured potentials are lower and the current density range is larger compared to the absence of the conducting layers.

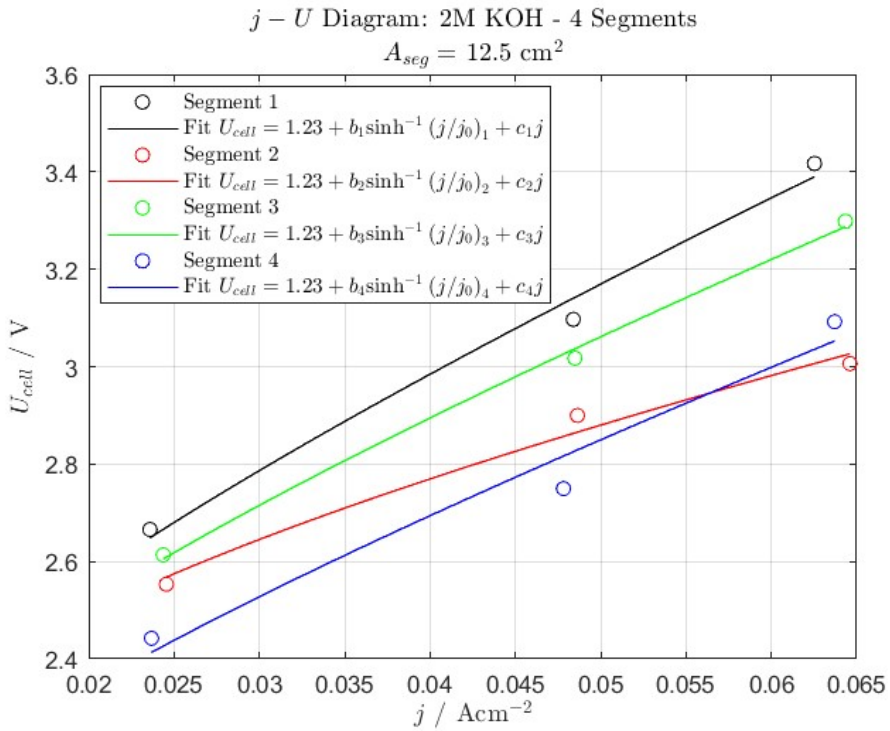

Figure 5.63: $j - U$ Diagram for the 2M KOH constant current top-down experiment utilising all four segments. Trends show current-potential for every segment and their fits.

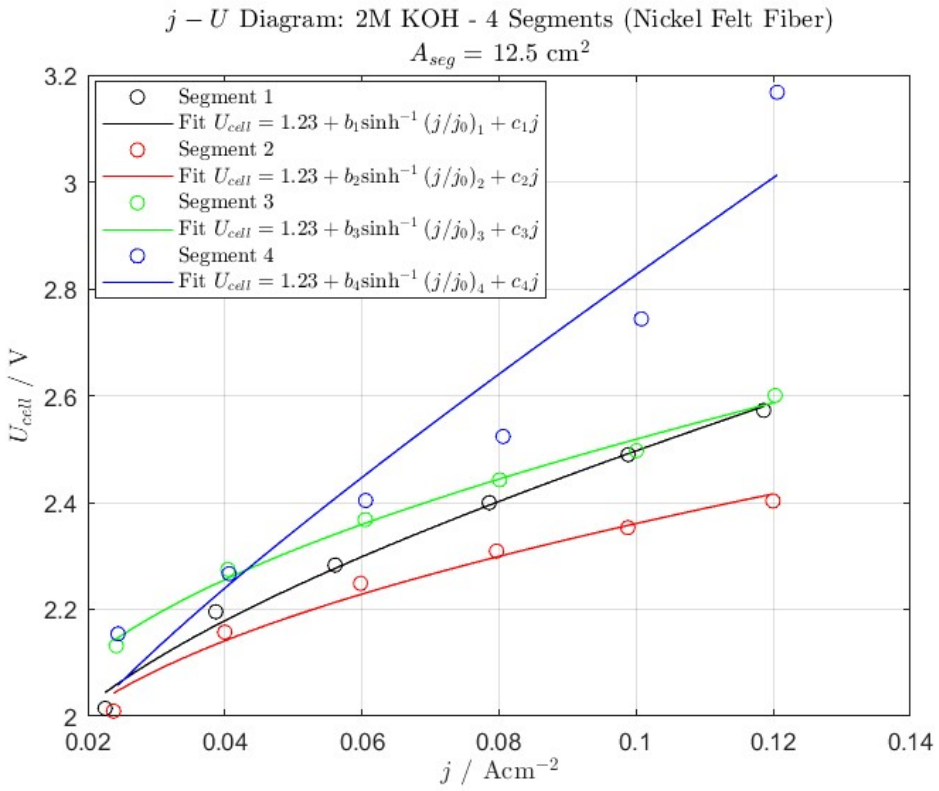

Figure 5.64: $j - U$ Diagram for the 2M KOH constant current top-down experiment utilising all four segments with addition of Nickel Fiber Felt conducting layers. Trends show current-potential for every segment and their fits.

Impact of porous conducting layers

Table 5.5 presents the Tafel constants for the small cell and segmented cell. The maximum areal resistance for the segmented cell without conducting layers is measured to be equal to approximately 15 Ωcm^2. All segments exhibit relatively high areal ohmic resistances. By using 2M KOH as the electrolyte the ionic conductivity decreases to 40 S/m compared to 70 S/m for 6M KOH. However, this decrease is likely to explain the high resistance noted. Presumably, the poor electronic conductivity is the major cause because the entirety of the electrode area is not fully utilised. Improving ionic conductivity using Nickel Felt Fiber conducting layers shows a significant difference. The maximum areal resistance for segments 1-3 with these conducting layers is measured to be equal to approximately 3.21 Ωcm^2. However, segment 4 still exhibits a large areal resistance. For this segment we still measure relatively large overpotentials whereas the measured temperature stays relatively low. It is likely then that this is because the lack of good power connection to the electrodes at this segment.

Fit Coefficients: Small cell and Segmented cell

Experiment	**Cell**	**Tafel Slope** b **Vdec**$^{-1}$	**Resistance** c Ω **cm**^{2}
Constant Current 6M KOH	Small cell	0.0995	1.6071
Constant Current Top-Down - 4 Segments 2M KOH	Segmented cell Segment 1	0.1990	14.0610
	Segmented cell Segment 2	0.2137	6.1913
	Segmented cell Segment 3	0.1915	12.1610
	Segmented cell Segment 4	0.1598	11.7239
Constant Current Top-Down - 4 Segments 2M KOH (Nickel Felt Fiber)	Segmented cell Segment 1	0.1370	3.2064
	Segmented cell Segment 2	0.1422	1.4843
	Segmented cell Segment 3	0.1580	1.9673
	Segmented cell Segment 4	0.1150	8.0229

Table 5.5: Overview of Tafel constants shown in Equation 5.16 for the small cell and the segmented cell. b is the Tafel slope and c represents the ohmic resistance. j_0 has been assumed to be equal to 10^{-4} Acm^{-2}.

6

Conclusions

6.1. Conclusions

This study aims to answer the main research question: "How hot does a capillary-fed electrolyzer become during water electrolysis as a function of the areal heat dissipation? To answer this, various experiments have been presented in Chapters 3 and 4. We have seen in section 5.1 that compression greatly impacts capillarity over time and show that deviation from the Lucas-Washburn approximation is not uncommon. For the small cell in section 5.4.1, using 6M KOH as the electrolyte showed that running at current densities close to $j = 1000$ mAcm^{-2} leads to relatively high potentials. These potentials were equal to at least $U = 4.0$ V. This is likely to be due to very low electronic conductivity and limited capillarity. Furthermore, the accompanied temperature measurements showed a large sudden increase in temperature for all studied ROIs, closing in to $T = 120°$C along the cell close to the top left edge of the cathode. The observed damage to the cell components showed that ohmic resistance is likely the primary cause due to dried up regions along the electrode. In the segmented cell the vertical direction was the axis of interest, we have seen that high overpotentials of $U \geq 3$ V are still seen at very low current densities. Additionally, also very high ohmic resistances are measured as was shown in Table 5.5. Primarily KOH concentrations with molalities of 2M and 3M were utilised to study capillary dynamics and study the period for which sustained electrolysis could be performed. Bottom and top feed were studied separately. The bottom-up study in section 5.4.2 was reduced to a single segment study. The center of the nickel-mesh electrodes was seen to experience the highest temperatures. These reached approximately $T = 55.0°$C at a location just above the center of the electrode. This was measured at a potential of approximately $U = 3.2$ V and current density equal to $j = 80$ mAcm^{-2}. Due to low electronic conductivity, there is a poorly distributed current along the segment which makes the accompanying measurements for this cell less relevant. The top segment (Segment 1) in a 4 segment top-down feed reached approximately $T = 50.0°$C in the center at a current density of $j \approx 63$ mAcm^{-2} and cell potential of $U = 3.42$ V. Segment 2-4 show that the hottest parts shift upwards along the electrodes, encompassing the top half of every segment which were subsequently rendered the hottest. Temperatures between $40°C \leq T \leq 50.0°C$ were measured. Compared to addition of Nickel Fiber Felt conducting layers, the power densities are similar if these are compared with the temperature difference. However, for the Nickel Felt Fiber these power densities were calculated from far lower measured cell potentials and higher current densities. Improving the former is beneficial for efficient water electrolysis as the accompanied losses are reduced.

Section 5.3 showed that the diaphragm is a limited factor for capillary-fed electrolysis. The hydrophilic membrane acts as a hydrophobic substrate when dealt with high concentration KOH solutions as the electrolyte. A 6M KOH sample was measured to have a mean contact angle of 78.14° for samples not larger than several microliters. Furthermore, increasing the molality greatly increases saturation time due to slower penetration. The time it takes for a 3M solution (section 5.5.1) to saturate a single segment is almost twice as long as it takes for a 2M solution to saturate a segment (section 5.5.2). Where compression works for the small cell, the same can not be concluded for the segmented cell.

In conclusion, the study has shown that:

- In a capillary-fed electrolyzer performing water electrolysis with a 2M KOH solution, a well distributed current over the segments leads to a maximum measured temperature difference of 50°C with an areal heat dissipation of $h = 11.5$ W/m^2K with a top-down feed. The highest heat dissipation occurs at the lowest segment at $h = 43.86$ W/m^2K in a top-down feed. For a bottom-up feed $h = 19.13$ W/m^2K. However, precipitation occurred at temperatures close to $T = 50°$C.
- Convection is not the predominant contributor to the overall heat transfer coefficient. This was evident from the small cell as well as the segmented cell;
- Local evaporation along electrode segments induce an increase in potential due to electrolyte starvation. This is clear from both the bottom-up and top-down feed. The former results in local precipitation which renders it unsuitable for at least tall designs;
- Electrolyte solutions of ≥ 5M KOH are less suitable if capillary rise of several centimeters is the aim. 1-3M KOH solutions have been shown to be manageable insofar capillarity and capillary-fed electrolysis go. The hydrophilic polyethersulfone acts as a hydrophobic substrate. The reason behind this is not yet know.

6.2. Future work

There is still much fruitful work to be done in the field of capillary-fed electrolysis. With regard to this thesis, a set of recommendations for future work are highlighted below:

- Find out the origin of the very large areal resistance that are obtained and make these an order of magnitude smaller than reported.
- Expand the study on effects of KOH concentration on capillary imbibition. A small set of KOH solutions have been discussed which have shown limited capillary action. Particularly for polyethersulfone the orientation of the individual fibers could provide more insight into the peculiar behaviour of highly concentrated electrolytic solutions on capillarity. SEM images can give insight into the presence of air pockets.
- Model heat transfer phenomena. This thesis has focused primarily on experimental work. A mathematical model that can retrace the oscillatory behaviour of the temperature plots can give valuable insights already early into the design stage.
- Determine contribution of conduction and radiation to the overall heat transfer coefficient.
- Utilise gas diffusion layers in the cell. The segmented cell was designed to include gas diffusion layers. However, this would obstruct individual analysis of the four segments. Hence, a future design that could integrate gas diffusion layers while at the same time allow thermometry, e.g. utilising thermocouples, would provide a useful comparison between the case in which no gas diffusion layer is applied.
- Comparing different electrodes and conducting layers can bring down a reduction of ohmic losses. The present study focused on a variety a diaphragms. Furthermore, the cell can be expanded from a batch process to a continuous process, e.g. by means of a pump to feed and extract liquid from and to the reservoirs.
- Regarding the design of the (segmented) capillary-fed cell. The cell should be made more modular. Between experiments, there was often need to disassemble the cell for thorough cleaning. A design in which only the MEA assembly can be interchanged for a fresh new MEA would pose beneficial for the amount of experiments that could be performed. Especially since the largest alterations are often made to the MEA. Furthermore, air holes should be included in a future design for the reservoirs which eases cleaning greatly.

References

[1] G. Tsekouras et al. A. Hodges A.L. Hoang. “A high-performance capillary-fed electrolysis cell promises more cost-competitive renewable hydrogen”. In: *NATURE COMMUNICATIONS* 13 (2022).

[2] G. Tsekouras et al. A. Hodges A.L. Hoang. “Supplementary Information A high-performance capillary-fed electrolysis cell promises more cost-competitive renewable hydrogen”. In: (2022).

[3] L. Gandia A. Ursua and P.Sanchis. “Hydrogen Production From Water Electrolysis: Current Status and Future Trends”. In: *Proceedings of the IEEE* 100.2 (2011), pp. 410–426.

[4] advancedthermo.com. *Density of potassium hydroxide, KOH(aq)*. 2023. URL: https://advancedthermo.com/electrolytes/density_KOH.html (visited on 06/11/2023).

[5] A. Ansar et al. *Alkaline electrolysis—status and prospects*. Chapter 5. Elsevier, 2022.

[6] G. Swiegers et al. “Current status of membraneless water electrolysis cells.” In: *Current Opinion in Electrochemistry* 32.100881 (2022).

[7] G. Tsekouras et al. “Insights into the phenomenon of ‘bubble-free’ electrocatalytic oxygen evolution from water”. In: *Sustainable Energy Fuels* 5 (2021). DOI: 10.1039/d0se01633k, pp. 808–819.

[8] J. Archila et al. *Development of a Novel Green Bio-Nanofluid from Sapindus Saponaria for Enhanced Oil Recovery Processes*. 2022. URL: https://www.researchgate.net/publication/360855479_Development_of_a_Novel_Green_Bio-Nanofluid_from_Sapindus_Saponaria_for_Enhanced_Oil_Recovery_Processes (visited on 05/20/2023).

[9] P.M. Diéguez et al. “Thermal performance of a commercial alkaline water electrolyzer: Experimental study and mathematical modeling”. In: *International journal of hydrogen energy* 22 (2008), pp. 7338–7354.

[10] W. Boyce et al. *Elementary Differential Equations and Boundary Value Problems*. 11th ed. ISBN: 9781119382874: Wiley, 2017.

[11] Y. Kamei et al. *C.A. Patent CA2934431C. Alkaline water electrolysis diaphragm, method of manufacturing same, and alkaline water electrolyzer*. 2013. URL: https://example.com (visited on 11/29/2022).

[12] The WayBackMachine Internet Archive. *COSMIC ABUNDANCE of the ELEMENTS and NUCLEOSYNTHESIS*. 2005. URL: https://web.archive.org/web/20060901133923/http://www.astro.wesleyan.edu/~bill/courses/astr231/wes_only/element_abundances.pdf (visited on 10/17/2022).

[13] PV magazine Australia. *Hysata brings capillary-fed electrolyzer tech closer to commercial production.* 2022. URL: https://www.pv-magazine.com/2022/08/02/hysata-brings-capillary-fed-eletrolyzer-tech-closer-to-commercial-production/ (visited on 10/14/2022).

[14] C. van den Berg et al. *NEDERLAND ONAFHANKELIJK VAN RUSSISCH GAS. OPTIES VOOR KORTE EN LANGE TERMIJN.* Rapportnumer P10971. TNO, 2022.

[15] J. Brauns and T. Turek. “Alkaline Water Electrolysis Powered by Renewable Energy: A Review”. In: *Processes* 8.248 (2020). doi:10.3390/pr8020248.

[16] Jianchao Cai and Boming Yu. “A discussion of the effect of tortuosity on the capillary imbibition in porous media”. In: *Transport in porous media* 89.2 (2011), pp. 251–263.

[17] M. Carmo. *Introduction to Liquid Alkaline Electrolysis*. 2022. URL: https://www.energy.gov/sites/default/files/2022-02/2-Intro-Liquid$%5C%$20Alkaline$%5C%$20Workshop.pdf (visited on 12/29/2022).

[18] *Cellulose Nitrate (Mixed Cellulose Ester) Membrane Filters / Type 11306*. 2022. URL: https://www.sartorius.com/shop/ww/en/eur/applications-laboratory-filtration/cellulose-nitrate-$%5C%$28mixed-cellulose-ester$%5C%$29-membrane-filters-type-11306$%5C%$2c-0-45-$%5C%$C2$%5C%$B5m-pore-size$%5C%$2c-55-mm-diameter$%5C%$2c-100-pieces-per-pack/p/11306--55------N.

[19] A. Champenier. *Hydrogen's Role in the Green Economy*. 2020. URL: https://www.lazardassetmanagement.com/references/fundamental-focus/hydrogens-role-in-the-green-economy (visited on 01/08/2023).

[20] CNRood. *SM45-140*. 2023. URL: https://www.cnrood.com/nl/sm45-140 (visited on 05/24/2023).

[21] L. Zhuang D. Tang J. Lu and P. Liu. "Calculations of the exchange current density for hydrogen electrode reactions: A short review and a new equation". In: *Journal of Electroanalytical Chemistry* 644 (2010), pp. 144–149.

[22] Peggy M Dunlap and Sam R Faris. "Surface tension of aqueous solutions of potassium hydroxide". In: *Nature* 196.4861 (1962), pp. 1312–1313.

[23] Eleshop.nl. *Owon SPE6103 labvoeding*. 2023. URL: https://www.eleshop.nl/owon-spe6103-labvoeding.html (visited on 05/24/2023).

[24] N Fries and M Dreyer. "An Analytic Solution of Capillary Rise Restrained by Gravity". In: (2008).

[25] RJ Gilliam et al. "A review of specific conductivities of potassium hydroxide solutions for various concentrations and temperatures". In: *International Journal of Hydrogen Energy* 32.3 (2007), pp. 359–364.

[26] E. Guerrini and S. Trasatti. *Electrocatalysis in Water Electrolysis*. ISBN: 978-3-527-32095-0. WILEY-VCH Verlag GmbH & Co. KGaA, Weinheim, 2009.

[27] F. Hine and K. Murakami. "Bubble Effects on the Solution IR Drop in a Vertical Electrolyzer Under Free and Forced Convection." In: *Journal of The Electrochemical Society* 127.292 (1980).

[28] R. Holyst and A.Poniewierski. *Thermodynamics for Chemists, Physicists and Engineers*. Dordrecht Heidelberg New York London: Springer, 2012.

[29] H. Rajaei J.W. Haverkort. "Voltage losses in zero-gap alkaline water electrolysis." In: *Journal of Power Sources* 497.229864 (2021).

[30] S. Kranias. "Effect of drop volume on static contact angles". In: (), p. 2.

[31] L. JANSSEN L. CZARNETZKI. "Electrode current distribution in a hypochlorite cell." In: *JOURNAL OF APPLIED ELECTROCHEMISTRY* 19 (1989), pp. 630–636.

[32] M. Lago and M. Araujo. "Capillary Rise in Porous Media". In: *Journal of Colloid and Interface Science* 234.1 (2001), pp. 35–43.

[33] N. Lu and W. J. Likos. "Rate of Capillary Rise in Soil". In: *Journal of Geotechnical and Geoenvironmental Engineering* 130.6 (2004), pp. 646–650.

[34] D. Lumanauw. *Hydrogen bubble characterization in alkaline water electrolysis.* Master Thesis. University of Toronto Department oi Metallurgy and Materials Science, 2000.

[35] C. Reynoso M. Lavorante and J. Franco. "Straight-Parallel Electrodes and Variable Gap for Hydrogen and Oxygen Evolution Reactions". In: *International Journal of Electrochemistry* 2019 (2019). https://doi.org/10.1155/2019/5392452, p. 11.

[36] J.C. Melrose. "Wettability as related to capillary action in porous media." In: *Society of Petroleum Engineers Journal* 5.03 (1965), pp. 259–271.

[37] A. Mills. *Basic Heat and Mass Transfer*. 2nd ed. Pearson Education Limited, 2013.

[38] B. Winther-Jensen O. Winther-Jensen K. Chatjaroenporn and D.R. MacFarlane. "Towards hydrogen production using a breathable electrode structure to directly separate gases in the water splitting reaction." In: *International journal of hydrogen energy* 37 (2012), pp. 8185–8189.

[39] G. Swiegers P. Tiwari K. Wagner and G. Wallace. "A new class of bubble-free water electrolyzer that is intrinsically highly efficient". In: *International Journal of Hydrogen Energy* 44 (2019), pp. 23568–23579.

[40] *Polyethersulfone (PES)*. 2022. URL: https://www.dispolab.nl/producten/polyethersulfone-pes/50249.

[41] Hodes S.J. et al. “Analyzing the heat distribution in a “bubble-free” capillary-fed electrolyzer under sub-optimal conditions”. In: (2022).

[42] J. D. Seader and E. J. Henley. *Separation Process Principles*. 2nd ed. ISBN-13 978-0-471-46480-8. John Wiley & Sons, Inc, 2006.

[43] Lecture Series. *3.4 THE BUTLER-VOLMER MODEL*. 2000. URL: https://ocw.snu.ac.kr/sites/default/files/NOTE/8$%5C%$20week.pdf (visited on 10/24/2022).

[44] Sigmaadrich.com. *Potassium Hydroxide*. 2023. URL: https://www.sigmaaldrich.com/NL/en/product/sigald/06103 (visited on 06/11/2023).

[45] J. Singh. *Capillary Rise*. 2019. URL: https://www.concepts-of-physics.com/mechanics/capillary-rise.php (visited on 10/24/2022).

[46] J. Garche T. Smolinka H. Bergmann and M. Kusnezoff. *The history of water electrolysis from its beginnings to the present*. Chapter 4. Elsevier, 2022.

[47] *Technical Data Sheet ZIRFON PERL UTP 500*. 2022. URL: https://www.agfa.com/specialty-products/wp-content/uploads/sites/8/2020/06/TDS_ZIRFON_PERL_UTP_500_20200525.pdf.

[48] Thomann.de. *Eurolite LED IP FL-10 SMD blue*. 2023. URL: https://www.thomann.de/nl/eurolite_led_ip_fl_10_smd_blue.htm?gclid=CjwKCAjw4ZWkBhA4EiwAVJXwqaRaaxQthVmh2mq6e_Gm4ekaZ2SNjMFIIoehfkxJd_9RSGe6dhqnZRoC4R0QAvD_BwE (visited on 06/11/2023).

[49] C. Toshiyouri. *The upper graph shows the current density as function of applied potential , the lower graph shows the logarithmic plot for different values of alpha.* 2016. URL: https://commons.wikimedia.org/wiki/File:Current_density_versus_potential_according_to_butler_volmer_equation.png (visited on 10/24/2022).

[50] Ø. Ulleberg. “Modeling of advanced alkaline electrolyzers: a system simulation approach”. In: *International Journal of Hydrogen Energy* 28 (2003), pp. 21–33.

[51] GC Vliet and DC Ross. “Turbulent natural convection on upward and downward facing inclined constant heat flux surfaces”. In: (1975).

[52] H. Voght. “The concentration overpotential of gas evolving electrodes as a multiple problem of mass transfer.” In: *Journal of The Electrochemical Society* 137.4 (1990), p. 1179.

[53] Warmtebeeldcamera.nl. *FLIR E4 WIFI POINT & SHOOT WARMTEBEELDCAMERA 80 X 60 PIXELS*. 2023. URL: https://www.warmtebeeldcamera.nl/nl/flir-e4-wifi.html (visited on 05/24/2023).

[54] E. W. WASHBURN. “The Dynamics of Capillary Flow”. In: *The Physical Review Second Series* XVII.3 (1921), pp. 273–283.

[55] *Whatman membrane filters nylon*. 2022. URL: https://www.sigmaaldrich.com/NL/en/product/aldrich/wha7404004.

[56] *Whatman quantitative filter paper, ashless, Grade 42*. 2022. URL: https://www.sigmaaldrich.com/NL/en/product/aldrich/wha1442055.

[57] Wikipedia. *Leyden jar*. 2022. URL: https://en.wikipedia.org/wiki/Leyden_jar (visited on 12/29/2022).

[58] K. Zeng and D. Zhang. “Recent progress in alkaline water electrolysis for hydrogen production and applications”. In: *Progress in Energy and Combustion Science* 36 (2010), pp. 307–326.

A

Appendix

A.1. Concentration overpotential

Ideally, advective and diffusive mass transport of electrolyte introduces reactants to the electrode surface. However, in an active electrochemical cell, local bubble nucleation can lead to partial coverage of the electrodes and a depletion of reactants. In addition, slow diffusive and advective mass transport can also lead to a depletion of reactants introduced to the electrode surfaces. Slow advection stagnates the rate with which bubbles are swept away from the electrode surface. Slow diffusion rates stagnate the rate with which new reactants are introduced to the electrodes. Consequently, a concentration overpotential can be measured. The reactants can be seen from the reactions in 2.1 and 2.2, i.e. water in the case of the cathode and hydroxide ions in the case of the anode. In the case of conventional alkaline water electrolyzers, introducing plenty of water would not lead to a source of concentration overpotential at the cathode. However, at the anode, a depletion of hydroxide ions may be observed and can lead to a source of concentration overpotential. We can use the concentration-dependent Butler-Volmer equation from Equation 2.29, neglecting the cathodic terms (for high overpotentials) to write:

$$\frac{j}{j_0} = \frac{C_{\mathrm{O}}}{C_{\mathrm{O,eq}}} \mathrm{e}^{\frac{-\alpha\eta F}{RT}} \tag{A.1}$$

$$\eta = -\frac{RT}{\alpha F} \ln\left(\frac{j}{j_0}\right) + \frac{RT}{\alpha F} \ln\left(\frac{C_{\mathrm{O}}}{C_{\mathrm{O,eq}}}\right) \tag{A.2}$$

From Equation A.2 we can recognize the summation of the anodic activation overpotential and concentration overpotential. Furthermore, it shows that the concentration overpotential is of the following form:

$$\eta_{\mathrm{con}} = \frac{RT}{\alpha F} \ln\left(\frac{C_{\mathrm{O}}}{C_{\mathrm{O,eq}}}\right) \tag{A.3}$$

We can relate Equation A.3 to the current density through the definition of the mass transfer coefficient k:

$$\frac{j}{nF} = k(C_{\mathrm{O}} - C_{\mathrm{O,eq}}) \tag{A.4}$$

Substituting Equation A.4 into Equation A.3 results in an expression for the concentration overpotential as a function of the current density j:

$$\eta_{\mathrm{con}} = \frac{RT}{\alpha F} \ln\left(\frac{j}{nFkC_{\mathrm{O,eq}}} + 1\right) \tag{A.5}$$

Similarly, the relation derived by Voght [52] describes the concentration overpotential as:

$$\eta_{\mathrm{con}} = \frac{\nu R_m T}{nF} \ln\left(\frac{j}{nFkC_{\mathrm{s}}} + \frac{C_\infty}{C_{\mathrm{s}}}\right) \tag{A.6}$$

with n the number of electrons (needed per mole of product, in Equation A.5 equal to 1), T the temperature and C_∞ the concentration in the bulk electrolyte far from the gas generating electrodes. Furthermore, note that $\nu = \alpha^{-1}$ in Equation A.6. $R_{\text{bubble,O}_2}$ and $R_{\text{bubble,H}_2}$ in Table 2.1 are examples of overpotentials caused by resistances due to bubble nucleation at the anode and cathode respectively. Generated bubbles masking the electrode surface take away electrode area available for electrolysis. Bubbles are non-conducting obstacles. Hence, the ionic current has to go around these bubbles, creating sites with increased current density while other sites remain inactive.

A.2. Cell temperature evolution

Apart from thermodynamic and electrochemical considerations, the thermal behaviour of the electrolyzer is the focal point of this thesis. At sufficiently high cell potentials Figure 2.4 has shown that exothermic reactions take place. Generated heat and especially an estimate thereof give insight into the heat and temperature distribution within the electrochemical cell. More importantly, as the current research focuses on heat transfer within a capillary-fed cell, thermal behaviour analyses can not be neglected. Direct gas production is beneficial insofar we can minimize ohmic losses while maintaining good thermal performance. However, as the thermal conductivity and heat capacity of gases is much lower than that of liquids, heat transfer in such electrochemical cells may pose additional complications. Diéguez et al. [9] investigated the thermal performance of alkaline water electrolyzers. Their analysis focused on a 22 cell bipolar series connected stack using 30wt% KOH as the electrolyte. Experiments performed evidenced that large thermal losses were caused by use of different power supply equipment. Furthermore, spatial cell temperature measurements were carried out indicating that heat losses were predominantly due to convection only. For their stack and thermal model, they utilised a Lumped Thermal Capacity (LTC) model [37]. The LTC approach assumes an unsteady temperature evolution and conveniently incorporates the energy conservation principle into the analysis. Furthermore, this approach also assumes a near uniform temperature distribution within components of a system, i.e. temperature gradients are of very small to negligible scale. This assumption can be made when the system's internal conductive resistance to heat transfer is relatively small compared to the external convective resistance to heat transfer. The Biot number is a dimensionless quantity that describes this ratio [37]:

$$\frac{\text{Internal conductive resistance}}{\text{External convective resistance}} \approx \frac{L/k_s A}{1/\bar{h}_c A} = \frac{\bar{h}_c L}{A} = \text{Bi} \tag{A.7}$$

with L the characteristic length of the solid body under consideration, k_s the thermal conductivity of the material, A the surface area and $\bar{h}_c$ the mean convective heat transfer coefficient. A Biot number of Bi < 0.1 assures that the center temperature does not deviate more than 5% as compared to the surface of the solid body and a uniform temperature distribution can be assumed.

Similarly to Diéguez et al., Ulleberg [50] also utilised the LTC approach in modeling the transient thermal behaviour of an advanced alkaline electrolyzer. Ulleberg aimed to approximate the temperature of the electrolyte and document how it evolved over time, resulting in a first-order non-homogeneous linear differential equation. Comparable to Diéguez et al. a simple 1-D approximation was used with regard to the time rate of change of internal energy of a system. In words this can be described as follows [37]:

$$\text{Internal Energy Rate of Change} = \text{Heat gain} - \text{Heat loss} + \text{Heat prod.} - \text{Heat sink}$$

Mathematically, we can express this as a first-order differential equation:

$$\rho V c \frac{dT}{dt} = \dot{Q}_{\text{gain}} + \dot{Q}_{\text{loss}} + \dot{Q}_v + \dot{Q}_{\text{sink}} \tag{A.8}$$

For a simple electrochemical cell, specifically a capillary-fed cell in this study, the heat gain from the surroundings and heat sinks are assumed negligible. This assumption is based on constant ambient conditions and the absence of any heat sinks or cooling water channels present in the cell which can act as heat sinks. Furthermore, when (external) methods of cooling will be included, logically $\dot{Q}_{\text{sink}} \neq 0$. Equation A.8 simplifies to:

$$C_t \frac{dT}{dt} = \dot{Q}_{\text{loss}} + \dot{Q}_v \tag{A.9}$$

with [9] [50]:

$$\dot{Q}_{\text{loss}} = \frac{1}{R_t}(T - T_a) \tag{A.10}$$

$$\dot{Q}_v = n_c \Delta E I \tag{A.11}$$

with R_t the electrolyzer cell thermal resistance, T_a the ambient temperature, $n_c = 1$ the number of cells in the stack. Substituting Equations A.10 and A.11 into Equation A.9 we find the following first-order linear non-homogeneous differential equation of the form [50]:

$$\frac{dT}{dt} + aT - b = 0 \tag{A.12}$$

with a and b constants. This gives a solution of the following form (see Appendix A.3 for the derivation):

$$T(t) = \left(\frac{b}{a}\right) + C\mathrm{e}^{-at} \tag{A.13}$$

with

$$a = -\frac{1}{C_t R_t} \tag{A.14}$$

$$b = \frac{n_c E I (1 - \eta_e)}{C_t} - \frac{T_a}{C_t R_t} \tag{A.15}$$

Note that the product $C_t R_t$ has units of seconds. Hence, this equation is a function of time. Furthermore, the constant C is determined from (initial) boundary conditions on the temperature.

A.3. Integrating factor

Equation A.9 describes

$$C_t \frac{dT}{dt} = \dot{Q}_{\text{loss}} + \dot{Q}_v \tag{A.16}$$

In which constant ambient conditions and the absence of any heat sinks are assumed. C_t the overall thermal capacity in J·K^{-1}, R_t the thermal resistance, T_a the ambient temperature and $n_c = 1$ the number of cells. We can solve this first-order linear differential equation by using a method of the *integrating factor* following the recipe from [10]. Substituting Equations A.10 and A.11 into A.9 we have

$$C_t \frac{dT}{dt} = \frac{1}{R_t}(T - T_a) + n_c \Delta E I \tag{A.17}$$

with $\Delta E = E - E_{\text{TN}}$. If we note that the electrolyzer efficiency is expressed as $\eta_e = E_{\text{TN}}/E$ we can rewrite the above as:

$$C_t \frac{dT}{dt} = \frac{1}{R_t}(T - T_a) + n_c E(1 - \eta_e) I \tag{A.18}$$

Which can be simply written in the form:

$$\frac{dT}{dt} + aT = b \tag{A.19}$$

We define the integrating factor as

$$I(t) = \mathrm{e}^{\int a dt} = \mathrm{e}^{at} \tag{A.20}$$

Multiplying Equation A.19 with the integrating factor we have:

$$I(t)\frac{dT}{dt} + I(t)aT = I(t)b \tag{A.21}$$

$$\mathrm{e}^{at}\frac{dT}{dt} + \mathrm{e}^{at}aT = \mathrm{e}^{at}b \tag{A.22}$$

$$\frac{d}{dt}\left[\mathrm{e}^{at}T\right] = I(t)b \tag{A.23}$$

$$\int d(\mathrm{e}^{at}T) = \int \mathrm{e}^{at} b dt \tag{A.24}$$

$$\mathrm{e}^{at}T = \left(\frac{b}{a}\right)e^{at} + C \tag{A.25}$$

$$T(t) = \left(\frac{b}{a}\right) + C\mathrm{e}^{-at} \tag{A.26}$$

Expanding all terms we find:

$$T(t) = -C_t R_t \left\{ \frac{n_c E I (1 - \eta_e)}{C_t} - \frac{T_a}{C_t R_t} \right\} + C\mathrm{e}^{-at} \tag{A.27}$$

In which the constant C is determined by (intial) boundary conditions for the temperature:

$$T_{\text{initial}} = T(t = 0) = -C_t R_t \left\{ \frac{n_c E I (1 - \eta_e)}{C_t} - \frac{T_a}{C_t R_t} \right\} + C \tag{A.28}$$

A.4. Temperature difference over the diaphragm length

Section 2.5 presented what we can utilise to provide a temperature difference along the vertical length of the cell. Equation 2.31 can be used with the following assumptions on the ambient conditions and dimensions. These are tabulated below:

Property	Value	Units
Pr	0.69	-
ν	$15.06 \cdot 10^{-6}$	$\mathrm{m^2s}{-1}$
k	0.0259	$\mathrm{Wm^{-1}K^{-1}}$
L	0.1	m
E_{cell}	2.0	V
E_o	1.48	V
j	3000	$\mathrm{Am^{-2}}$

Table A.1: Thermodynamic properties of air at atmospheric conditions $T_e = 293$ K.

Where k is the thermal conductivity and ν the kinematic viscosity. Furthermore, assuming natural convection into still ambient air, we can equate the heat production to convective heat transfer for a single cell via:

$$Q = \overline{E}I = \overline{h}_c A \Delta T \tag{A.29}$$

$$\overline{E}jA = \overline{h}_c A \Delta T \tag{A.30}$$

$$\overline{E}j = \overline{h}_c \Delta T \tag{A.31}$$

$$\frac{\overline{E}j}{\overline{h}_c} = \Delta T \tag{A.32}$$

The Nusselt number is a dimensionless quantity that relates the thermal conductivity to the (convective) heat transfer coefficient via $\overline{\mathrm{Nu}}_L = \overline{h}_c L/k$. Hence, by providing an initial guess for the temperature difference ΔT we can make a first estimate of the Rayleigh number and verify whether or not it applies to our laminar case. If not, subsequent iteration of ΔT should converge to a Rayleigh number which applies to laminar flow. Iteration of Equations 2.31 and 2.33 resulted in:

$$\begin{aligned} \Delta T &\approx 34 \ \ \mathrm{K} \\ \overline{h}_c &\approx 22.94 \ \ \mathrm{Wm^{-2}K^{-1}} \\ \overline{\mathrm{Nu}}_L &\approx 88.58 \\ \mathrm{Ra}_L &\approx 8.65 \cdot 10^8 \end{aligned}$$

This equates to a theoretical heat loss of $Q = \overline{h}_c A \Delta T \approx 7.8$ W.

B

Appendix

This Appendix serves to provide supplementary detail regarding cell design and methods. Details on dimensions of electrode segments, milling, contact angle equipment and tracer materials are presented here.

B.1. The segmented cell

Four segments are utilised in the vertical cell, resulting in 8 segments that are used over the entire length of the cell. Four anodes and four cathodes. Each electrode has a total surface area of $A_{\text{elec}} = 12.5$ cm^2. The separation between each electrode is equal to 5 mm to prevent rogue meshes to contact each other and create a short circuit. Figure B.1 shows two segments and their dimensions in millimeters.

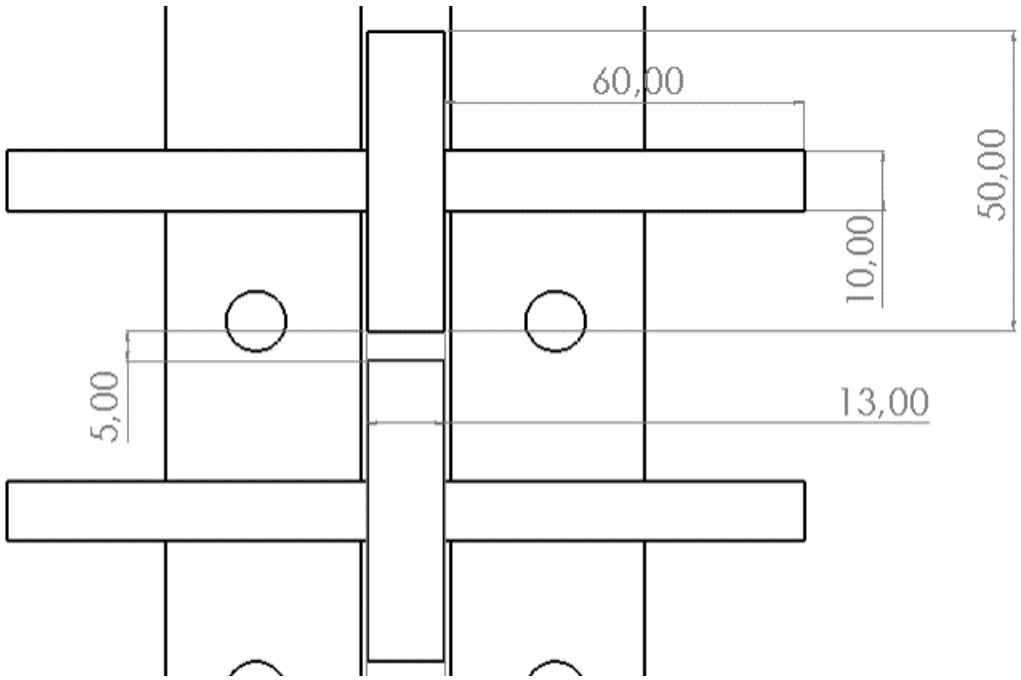

Figure B.1: Principle of the segmented cell. Instead of a single large nickel mesh electrode, the cell consist of 4 smaller equally sized segments which can be researched separately. All displayed length measurements are in millimetres.

B.2. Milling

Figure B.2 shows the milling work that has been done on two of the six PMMA plates. All shown dimensions are in millimeters. The channel runs over the whole vertical length between the electrolyte reservoirs. The channel depth is shown to be 1 mm for observational purposes. A depth of approximately 150 μm has been milled in order for the membrane pores to relax and promote capillary wicking. This thickness is approximately equal to the thickness of the membrane itself.

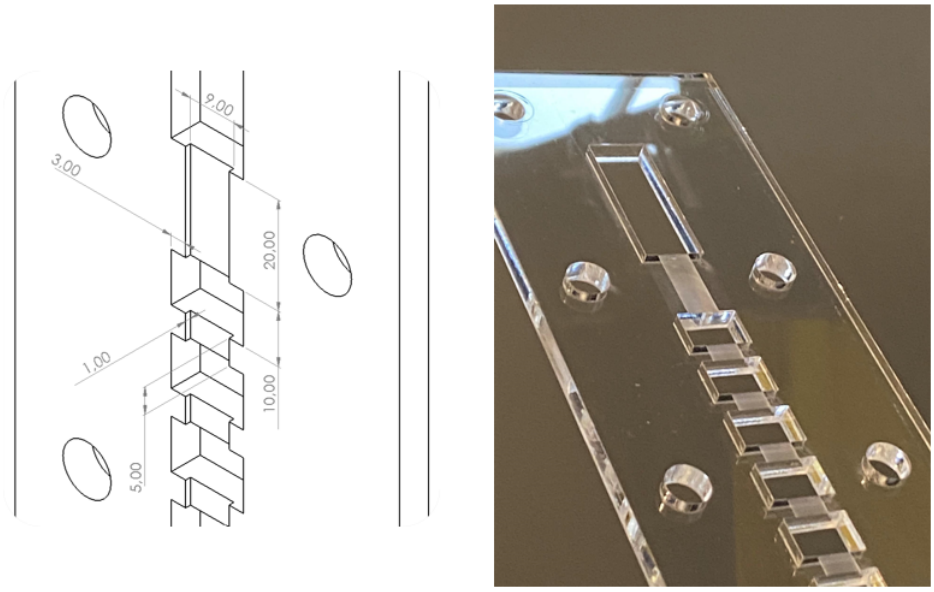

Figure B.2: Left: schematic of milled channel. Right: realised product. All displayed length measurements are in millimetres.

B.3. Theta Lite Optical Tensiometer

Figure B.3 shows the apparatus utilised for the contact angle experiments.

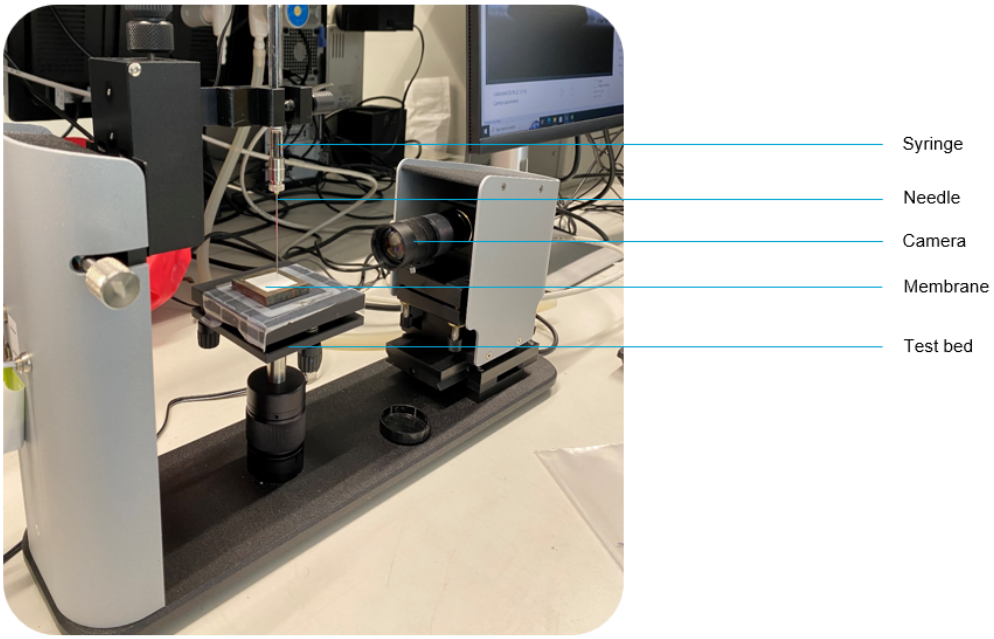

Figure B.3: Theta Lite Optical Tensiometer device in the Corrosion Technology and Electrochemistry lab. .

B.4. Capillary imbibition using tracers

Capillary imbibition was traced various times by utilising fluorescein salt as the tracer. Figure B.4 shows the segmented cell in the vertical configuration for three distinct time instances. The reservoir shown left is where 1M KOH electrolyte is injected. The solution reached the full length of the membrane and even is seen to penetrate into the bottom reservoir. An Eurolite LED IP FL-10 SMD (10 W) [48] blue light is used to illuminate the solution for clear tracing.

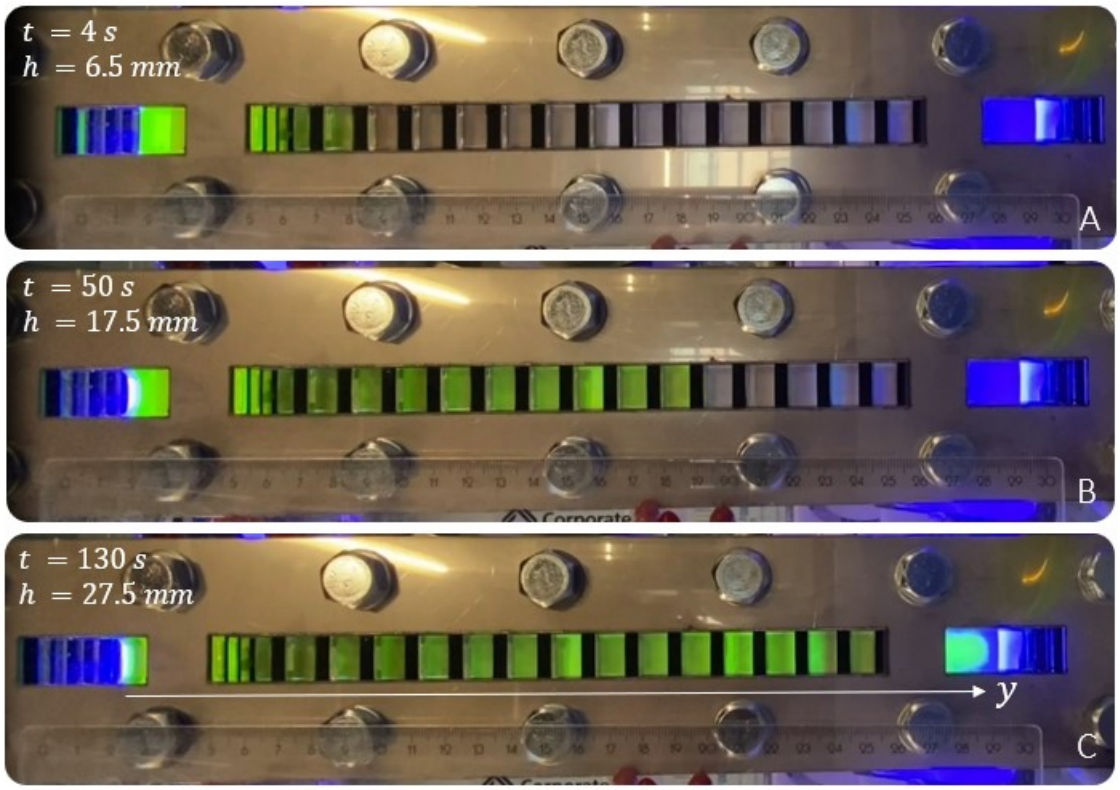

Figure B.4: Process of capillary imbibition using fluorescein salt as the tracer. Shown is the cell in the vertical configuration at various time instances, A, B, and C into imbibition. Note that the y-axis is pointing in the downwards vertical direction.

B.5. Nickel Fiber Felt capillarity

Figure B.5 shows an image taken of the FLIR E75 interface during water electrolysis. The Nickel Fiber Felt conducting layers can be seen to be approximately 10°C lower than the gas generating section at this time. The capillarity of the electrodes inherently aids capillary-fed electrolysis for longer time. Together with the improved electronic conductivity higher current densities (Figure 5.55) could be reached at lower areal ohmic resistance (Figure 5.64).

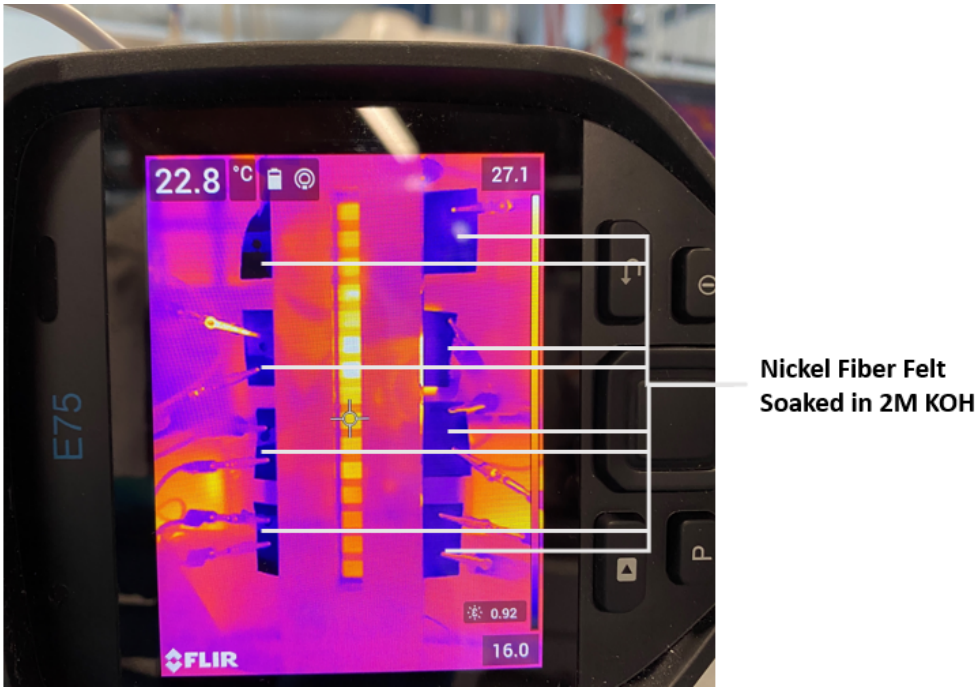

Figure B.5: Nickel Fiber Felt conducting layers during electrolysis. The low temperature evidently shows the capillary imbibition of electrolyte.

C

Appendix

This Appendix presents additional experimental work that has been performed. Appendix C.1 highlights a series of small introductory experiments that have been carried out. The study focused on electrolysis where the electrolyte level is decreased over time for two different cells. This is continued until the electrode area reached complete unimmersion. Appendix C.2 highlights the experimental results for penetration depth versus time for filter paper and nylon filter membranes. Comparisons can be seen between the uncompressed case and compressed case. These are collected in Appendix C.2. Appendix C.3 shows additional contact angle data and Appendix C.4 shows data for the constant current experiments reported in Chapter 5.

Preliminary experiments

The objective is to verify which membrane materials perform best when they are either completely immersed in an electrolyte solution and when they are only partly dipped in an electrolyte solution.

C.1. Variation of electrolyte level

The objective of these experiments are to compare different membrane materials on their performance when the electrolyte level is lowered. Hence, the aim is to promote direct-gas production with every subsequent lowering of the level and measure which material performs better over time. The cells in question have a zero-gap configuration and can be seen in Figure 4.1. The materials used were tabulated in Table 4.2. The initial condition for both cells is complete immersion in electrolyte, i.e. the electrodes should be completely immersed. Figures C.1 and C.2 show the first experimental findings. The legend displays the level of electrolyte in millimeters. It can be seen from the Zirfon Perl experiment that a reasonable current density is maintained with lowering of the electrolyte level with $525 \leq j \leq 600$ A·m^{-2}. In particular for the h_0 case we see that Zirfon Perl maintains a reasonable performance over time. This continued performance could be acclaimed to the diaphragm being wetted due to complete immersion for a large period of the experiment. The polyethersulfone experiment shows a somewhat better performance over time. A double membrane was used here to prevent short-circuiting of the membrane due to puncturing by the nickel-mesh electrodes. However, a higher potential was applied to the electrodes to perform electrolysis. It can be clearly seen here that for $h_5 \leq h \leq h_{30}$ the current density stays between $650 \leq j \leq 1000$ A·m^{-2}.

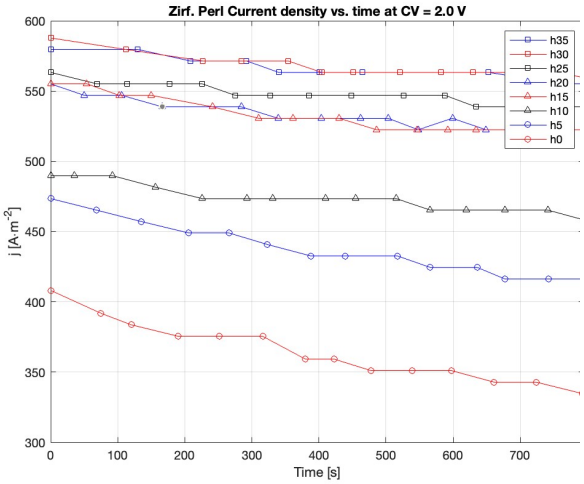

Figure C.1: Zirfon PERL UTP500 current density versus time. 1M KOH solution (h = 35 mm) and subsequent lowering of the electrolyte level until no immersion (h = 0 mm). Measurements were done manually at a 2.0 V constant voltage.

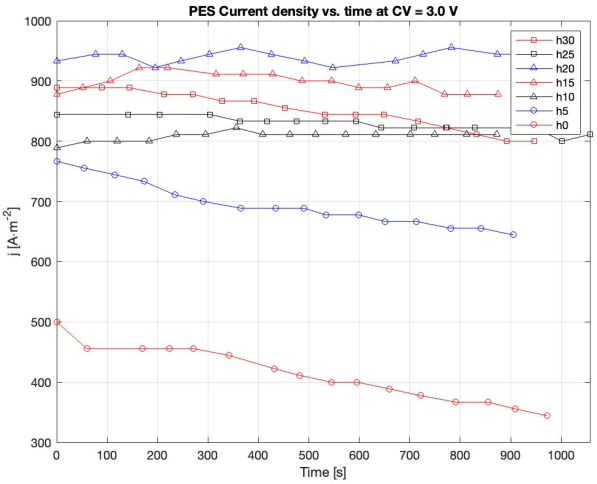

Figure C.2: Polyethersulfone current density versus time. 1M KOH solution (h = 30 mm) and subsequent lowering of the electrolyte level until no immersion (h = 0 mm). Measurements were done manually a 3.0 V constant voltage. 2 membranes are used on top of each other.

C.2. Capillary rise

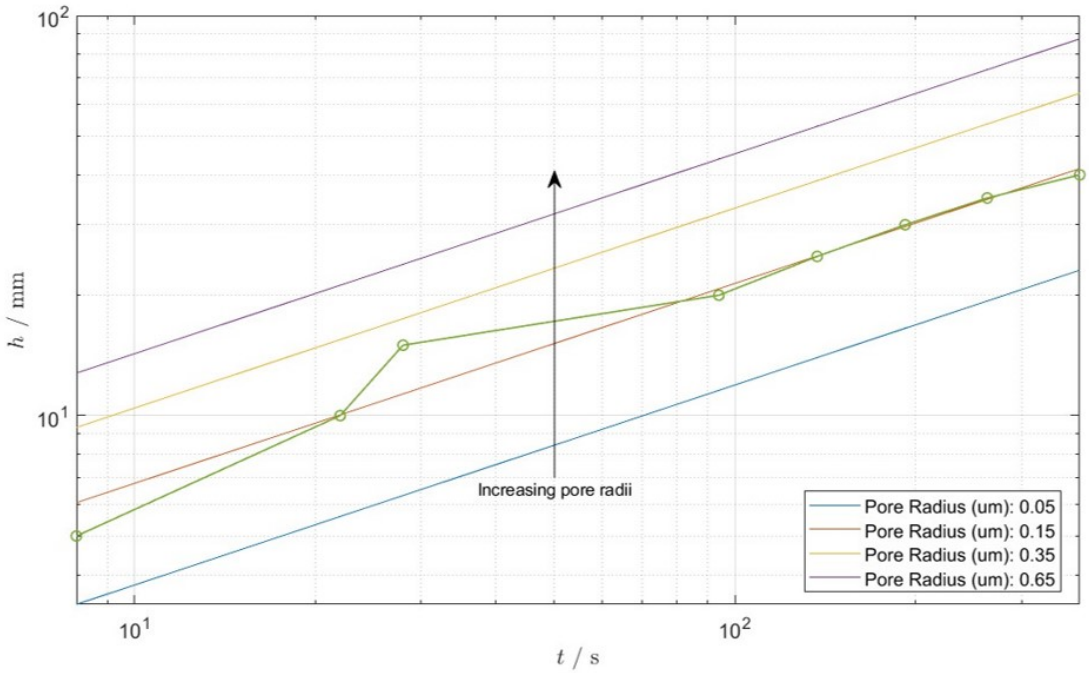

Figure C.3: Penetration depth versus time for uncompressed 2.5 μm Ashless Filter Paper. Lucas-Washburn approximations have been plotted to show what pore radii suit the membrane in question. Lucas-Washburn approximation follows Equation 2.46 with $\theta = 30^\circ$ at standard conditions for water.

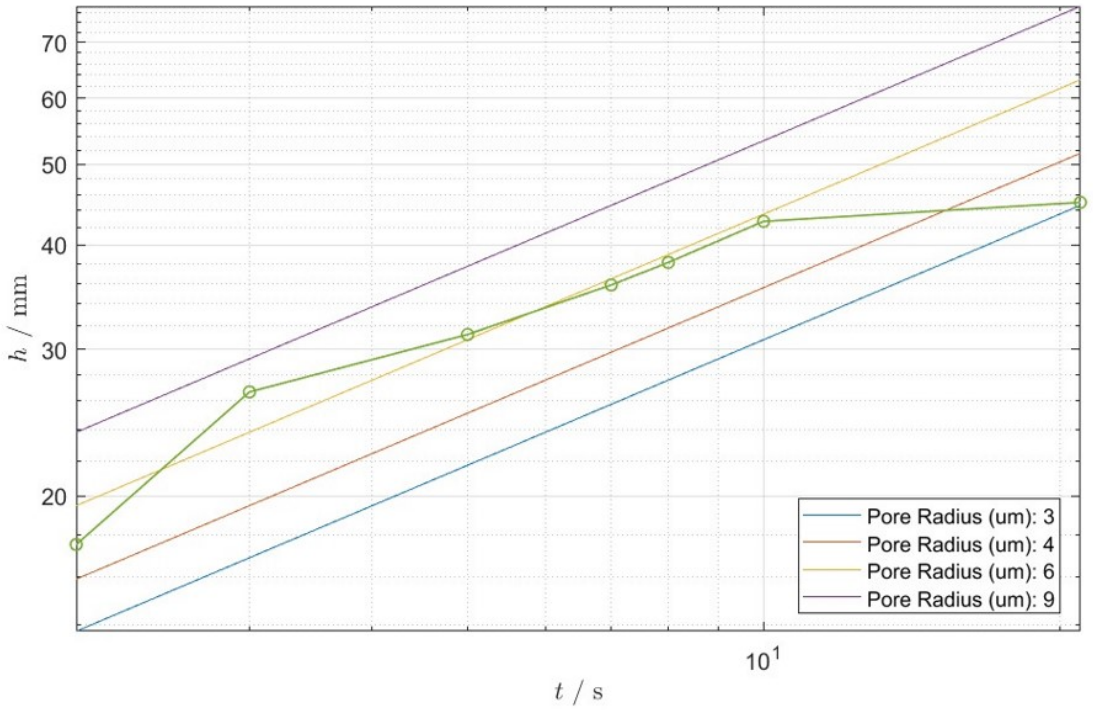

Figure C.4: Penetration depth versus time for compressed 2.5 μm Ashless Filter Paper. Lucas-Washburn approximations have been plotted to show what pore radii suit the membrane in question. Lucas-Washburn approximation follows Equation 2.46 with $\theta = 30°$ at standard conditions for water.

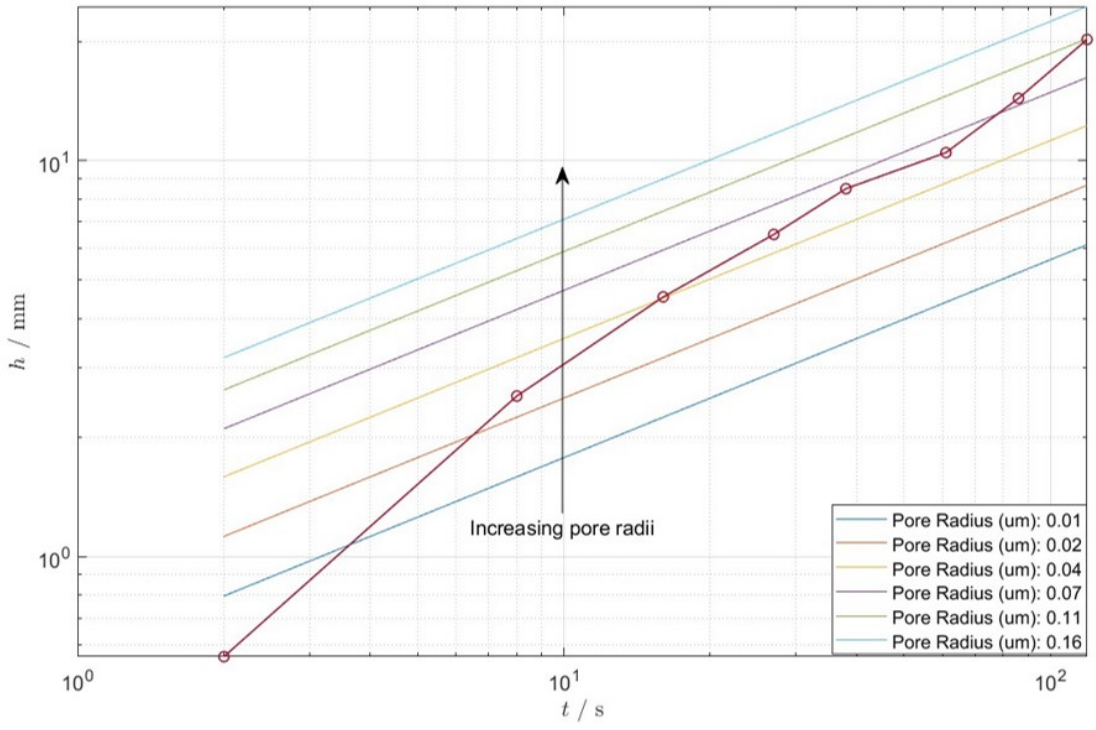

Figure C.5: Penetration depth versus time for uncompressed 0.45 μm Nylon Filter Membrane. Lucas-Washburn approximations have been plotted to show what pore radii suit the membrane in question. Lucas-Washburn approximation follows Equation 2.46 with $\theta = 30°$ at standard conditions for water.

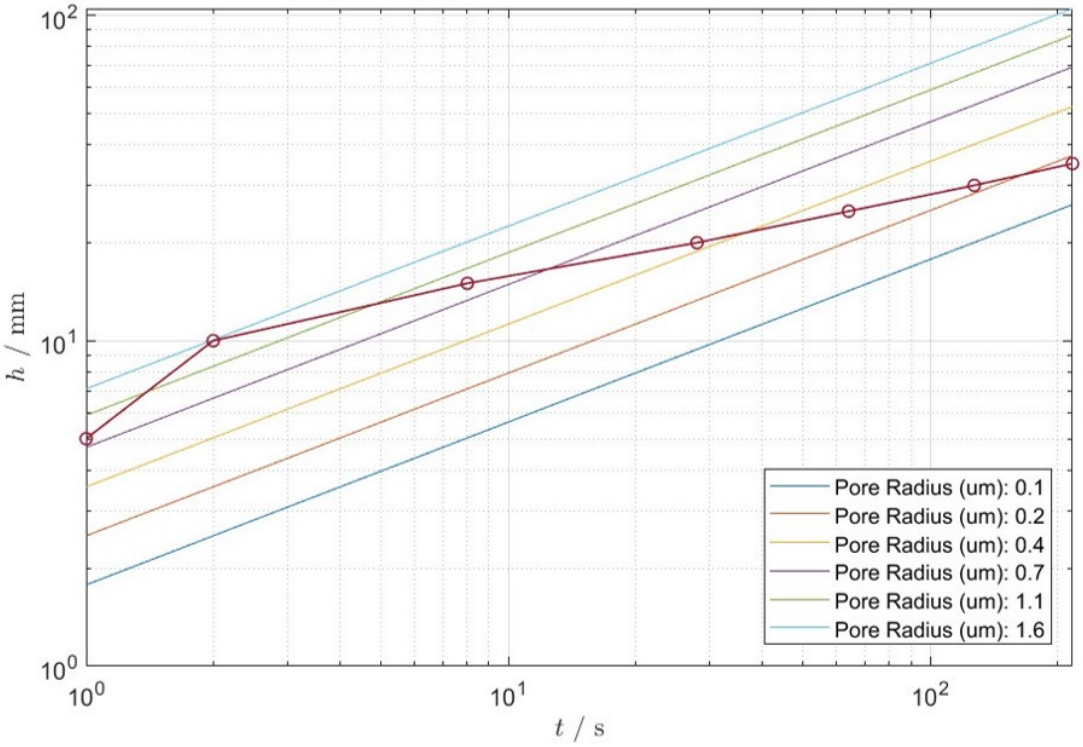

Figure C.6: Penetration depth versus time for compressed 0.45 μm Nylon Filter Membrane. Lucas-Washburn approximations have been plotted to show what pore radii suit the membrane in question. Lucas-Washburn approximation follows Equation 2.46 with $\theta = 30°$ at standard conditions for water.

C.3. Average contact angle

AVG CA			
Sample	**6M KOH + F** $\bar{\theta}$ **[°]**	**6M KOH** $\bar{\theta}$ **[°]**	**5M KOH** $\bar{\theta}$ **[°]**
i	78.02	70.94	80.12
ii	82.29	67.05	79.15
iii	76.44	78.63	71.39
iv	77.78	96.59	66.28
v	77.86	74.18	69.87
vi	72.88	81.43	76.56
$\bar{\bar{\theta}}$	77.54	78.14	73.90

Table C.1: Average contact angle measurements from each subsequent sample for given KOH solutions.

C.4. Constant current

Single Segment Constant Current Bottom-Up Experiment							
j **mA/cm^2**	U V	p **mW/cm^2**	$\bar{T}_{\text{seg}}$ **°C**	$\bar{T}_{\text{Top}}$ **°C**	$\bar{T}_{\text{HighMid}}$ **°C**	$\bar{T}_{\text{LowMid}}$ **°C**	$\bar{T}_{\text{Bott}}$ **°C**
58.98	2.99	89.32	36.81	34.91	42.43	45.32	35.45
78.60	3.18	133.40	42.85	42.75	50.21	47.88	37.53
0.68	0.08	0.95	34.49	36.19	38.46	32.76	27.80

Table C.2: Averaged results for 2M KOH Constant Current Bottom-Up experiment. Shown values are averaged and reported before current is increased.

3M KOH Single Segment Constant Current Top-Down Experiment							
j **mA/cm^2**	U V	p **mW/cm^2**	$\bar{T}_{\text{seg}}$ **°C**	$\bar{T}_{\text{1/4}}$ **°C**	$\bar{T}_{\text{2/4}}$ **°C**	$\bar{T}_{\text{3/4}}$ **°C**	$\bar{T}_{\text{4/4}}$ **°C**
22.25	2.40	20.53	22.17	21.82	25.51	26.08	23.91
38.48	2.62	44.05	25.51	24.03	31.19	31.23	27.06
78.57	2.96	116.12	29.24	26.68	41.14	37.82	30.55
62.82	2.81	83.71	30.22	27.84	41.29	39.0	32.43

Table C.3: Averaged results for 3M KOH Constant Current Top-Down experiment using a single segment. Shown values are averaged and reported before current is increased or decreased.

2M KOH 2-Segment Constant Current Top-Down Experiment								
Segment	j **mA/cm^2**	U V	p **mW/cm^2**	$\bar{T}_{\text{seg}}$ **°C**	$\bar{T}_{\text{1/4}}$ **°C**	$\bar{T}_{\text{2/4}}$ **°C**	$\bar{T}_{\text{3/4}}$ **°C**	$\bar{T}_{\text{4/4}}$ **°C**
1	22.73	2.63	59.80	17.12	13.52	17.80	21.47	19.38
2	23.08	2.46	56.97	18.19	18.38	21.64	23.44	19.57

Table C.4: Averaged results for 2M KOH Constant Current Top-Down experiment using the top two segments. Shown values are averaged and reported before current is increased.

2M KOH 4-Segment Constant Current Top-Down Experiment								
Segment	j **mA/cm**^{2}	U V	p **mW/cm**^{2}	$\bar{T}_{\text{seg}}$ **°C**	$\bar{T}_{1/4}$ **°C**	$\bar{T}_{2/4}$ **°C**	$\bar{T}_{3/4}$ **°C**	$\bar{T}_{4/4}$ **°C**
1	23.59	2.67	28.38	23.77	22.28	26.39	29.19	23.98
	48.39	3.10	78.86	29.24	26.38	37.21	38.58	28.86
	62.53	3.42	121.13	35.07	31.58	49.12	47.23	33.50
2	24.55	2.55	26.35	24.22	27.16	29.00	26.31	23.95
	48.64	2.90	75.17	30.85	36.84	42.04	33.82	29.72
	64.60	3.01	98.60	34.84	41.49	49.34	37.78	34.00
3	24.37	2.61	27.62	24.10	25.16	27.91	29.40	22.54
	48.49	3.02	81.75	30.62	34.52	41.18	38.26	26.40
	64.34	3.30	117.00	34.53	42.55	50.28	40.53	29.30
4	23.68	2.44	22.78	22.54	27.19	29.28	19.55	22.97
	47.82	2.75	67.14	26.55	40.56	40.09	20.07	25.02
	63.71	3.09	102.80	29.51	50.96	47.01	20.56	26.65

Table C.5: Averaged results for 2M KOH Constant Current Top-Down experiment using all segments. Shown values are averaged and reported before current is increased.

2M KOH 4-Segment Constant Current Top-Down Experiment (Nickel Fiber Felt)								
Segment	j **mA/cm^2**	U V	p **mW/cm^2**	$\bar{T}_{\text{seg}}$ **°C**	$\bar{T}_{1/4}$ **°C**	$\bar{T}_{2/4}$ **°C**	$\bar{T}_{3/4}$ **°C**	$\bar{T}_{4/4}$ **°C**
1	22.52	2.01	12.04	20.03	21.00	20.93	21.43	23.47
	38.66	2.20	27.66	22.07	24.03	24.21	24.35	25.58
	56.08	2.28	45.44	24.54	26.72	27.25	27.56	28.44
	78.56	2.40	72.25	27.16	30.52	31.20	31.31	31.30
	98.81	2.49	99.76	32.73	39.44	39.74	38.43	37.92
	118.59	2.57	129.54	36.81	46.10	45.80	43.25	43.45
2	23.75	2.01	12.58	23.84	25.02	28.73	29.72	24.31
	39.99	2.16	27.09	24.00	25.41	26.64	27.47	25.30
	59.79	2.25	45.96	27.16	28.32	30.29	31.69	29.32
	79.62	2.31	66.02	29.81	31.11	33.99	35.23	32.39
	98.78	2.35	86.27	37.03	38.61	43.94	45.60	40.06
	119.94	2.40	110.69	42.67	45.71	52.28	50.59	45.63
3	24.15	2.13	15.74	20.13	22.32	21.16	21.08	21.12
	40.45	2.27	32.14	23.11	25.74	25.22	24.81	24.63
	60.46	2.37	53.67	25.69	29.52	28.56	27.80	27.44
	80.06	2.44	77.06	28.06	32.89	31.91	30.68	30.18
	100.04	2.50	101.73	33.90	41.46	40.36	38.24	36.87
	120.26	2.60	134.73	37.13	46.57	44.45	42.11	40.05
4	24.41	2.15	16.46	19.32	20.31	19.90	18.35	19.44
	40.61	2.27	31.95	21.64	23.42	22.88	22.09	22.70
	60.53	2.40	55.92	23.99	26.31	25.41	25.26	25.51
	80.56	2.52	84.08	26.46	29.08	27.84	28.32	27.90
	100.75	2.74	127.33	31.35	35.46	33.58	34.41	33.85
	120.56	3.17	203.51	33.41	37.33	35.87	36.98	36.53

Table C.6: Averaged results for 2M KOH Constant Current Top-Down experiment using all segments with added Nickel Fiber Felt conducting layers. Shown values are averaged and reported before current is increased.